FLUID FLOW IN HORIZONTAL INJECTION REGIMES

By

ANDREW A. SHOOK

B.E., The University of Saskatchewan, 1983

A THESIS SUBMITTED IN PARTIAL FULFILLMENT OF

THE REQUIREMENTS FOR THE DEGREE OF

MASTER OF APPLIED SCIENCE

in

THE FACULTY OF GRADUATE STUDIES

Department of Metallurgical Engineering

We accept this thesis as conforming

to the required standard

THE UNIVERSITY OF BRITISH COLUMBIA

October, 1986

In presenting this thesis in partial fulfilment of the requirements for an advanced degree at the University of British Columbia, I agree that the Library shall make it freely available for reference and study. I further agree that permission for extensive copying of this thesis for scholarly purposes may be granted by the head of my department or by his or her representatives. It is understood that copying or publication of this thesis for financial gain shall not be allowed without my written permission.

Department of Metals & Materials Engineering

The University of British Columbia
1956 Main Mall
Vancouver, Canada
V6T 1Y3

Date Feb 20/87

ABSTRACT

Physical and mathematical modelling studies have been performed to investigate liquid flow driven by a horizontally injected gas.

The experimental work consisted of water velocity measurements made at 100 locations within a plexiglass tank. Air was introduced into the tank through a series of side-mounted tuyeres, and the effect of air flowrate on water recirculation velocity was observed. The results of the experiments indicate that the maximum water velocity occurs at the water surface. The effect of bubbles coalescing from adjacent tuyeres was observed with increasing air flowrate, and was found to diminish the water recirculation rate.

The mathematical model employed a variant of the Marker and Cell (MAC) technique to compute fluid flow with a free surface. The model predictions indicate that the flow in the experimental tank is largely driven by water flowing across the free surface. Based on this knowledge, qualitative predictions of the flow regimes in a Peirce-Smith copper converter and a zinc slag fuming furnace were made.

TABLE OF CONTENTS

	Page
ABSTRACT	ii
TABLE OF CONTENTS	iii
LIST OF TABLES	vi
LIST OF FIGURES	vii
NOMENCLATURE	xi
ACKNOWLEDGEMENTS	xiv
1. INTRODUCTION	1
1.1. Copper Smelting	1
1.2. The Copper Converter	4
1.2.1. History and Development	4
1.2.2. Difficulties	4
1.3. The Zinc Slag Fuming Furnace	5
1.4. Objectives of the Work	6
2. LITERATURE REVIEW	7
2.1. Flow Regimes in Non-Ferrous Metallurgical Reactors	7
2.2. Bubble Formation Investigations	10
2.3. Investigations of Gas-Driven Flow	12
2.3.1. Experimental Studies	12
2.3.2. Numerical Studies	15
2.4. Conclusions	19
3. EXPERIMENTAL	20
3.1. Objectives	20
3.2. Apparatus	20
3.3. Procedure	26
3.4. Experimental Results	28

TABLE OF CONTENTS (cont'd)

	Page
3.4.1. Introduction	28
3.4.2. Check of the Two Dimensionality of the Flow	30
3.4.3. Velocity Patterns	34
3.4.4. Surface Shape	36
3.4.5. Bath Stirring	37
4. THE MATHEMATICAL MODEL	43
4.1. General Statement of Problem	44
4.1.1. Governing Equations	44
4.1.2. Boundary Conditions	46
4.2. Selection of Solution Algorithm	48
4.3. The SOLASMAC Algorithm	53
4.4. Treatment of Boundary Conditions	56
4.4.1. Locating and Moving the Free Surface	56
4.4.2. Free Surface Velocities and Pressures	58
4.4.2.1. Normal Stress Condition	61
4.4.2.2. Tangential Stress Condition	61
4.4.3. Rectangular Wall Boundaries	63
4.4.4. Round Bottom Boundary	64
4.4.5. Gas-Liquid Boundary	65
5. CALCULATIONS - COMPARISON WITH EXPERIMENTAL RESULTS	67
5.1. Constant Vertical Velocity	70
5.2. Variable Density	73
5.3. Pulsed Boundary	77
5.4. Collapsing Surface	79
5.5. Discussion	83
6. INDUSTRIAL CALCULATIONS	86
6.1. Fluid Flow in a Copper Converter	86
6.1.1. Assumptions	86
6.1.2. Mathematical Description of Gas-Liquid Interface	87
6.1.3. Results	88

TABLE OF CONTENTS (cont'd)

	Page
6.2. Fluid Flow in a Zinc Slag Fuming Furnace	90
6.2.1. Assumptions	91
6.2.2. Modifications to Program	92
6.2.3. Mathematical Description of Bubble Column	93
6.2.4. Results	95
7. CONCLUSIONS	97
7.1. Experimental	97
7.2. Calculations - Agreement with Experimental Results	98
7.3. Industrial Calculations	99
7.3.1. Flow in a Copper Converter	99
7.3.2. Flow in a Zinc Slag Fuming Furnace	99
7.4. Recommendations for Further Work	100
REFERENCES	101
APPENDIX 1	107
TABLES	110
FIGURES	123

LIST OF TABLES

Page

Chapter 3

Table 3.1. Experimental Air Injection Rates..... 111

Table 3.2. Values of $\frac{\Delta w}{\Delta z}$ in Experimental Tank, Experiment 1..... 112

Table 3.3. Minimum Mean Values of $\frac{\Delta w}{\Delta z}$ of Experimental Runs..... 113

Chapter 4

Table 4.1. Approximations Used for Rectangular Wall Boundaries..... 114

Chapter 5

Table 5.1. Effective Viscosity Values Predicted by Model of Sahai and Guthrie (44)..... 115

Table 5.2. Comparison of Results Calculated by Constant Velocity Condition with Experiments..... 116

Table 5.3. Estimated Experimental Bubble Column Porosity Values.... 117

Table 5.4. Comparison of Results Calculated by Variable Density Condition with Experiments..... 118

Table 5.5. Comparison of Results Calculated by Pulsed Boundary Condition with Experiments..... 119

Table 5.6. Comparison of Results Calculated by Collapsing Surface Condition with Experiments..... 120

Chapter 6

Table 6.1. Data Used to Model Flow in Peirce-Smith Copper Converter..... 121

Table 6.2. Data Used to Model Flow in Zinc Slag Fuming Furnace..... 122

LIST OF FIGURES

Page

Chapter 1

Figure 1.1. Schematic Diagram of Peirce-Smith Copper Converter..... 124

Figure 1.2. Schematic Diagram of Zinc Slag Fuming Furnace..... 125

Chapter 2

Figure 2.1. Estimate of Flow in a Copper Converter, from Themelis et al. (3)..... 126

Figure 2.2. Predicted Flow Profile in Two-Phase Region of Copper Converter, from Nakanishi and Szekely (4)..... 127

Figure 2.3. Jet Behaviour Diagram, from Hoefele and Brimacombe (7)..... 128

Chapter 3

Figure 3.1. Schematic Diagram of Experimental Apparatus..... 129

Figure 3.2. Dimensions and Construction of Experimental Tank..... 130

Figure 3.3. Diagram of Laser-Doppler System..... 131

Figure 3.4. Velocity Measurement Locations Within Experimental Tank..... 132

Figure 3.5. Horizontal Velocity Variation Through Depth of Tank..... 133

Figure 3.6. Vertical Velocity Variation Through Depth of Tank.... 134

Figure 3.7. Experimental Velocity Vector and Surface Plot - Experiment 1..... 135

Figure 3.8. Experimental Velocity Vector and Surface Plot - Experiment 2..... 136

Figure 3.9. Experimental Velocity Vector and Surface Plot - Experiment 3..... 137

Figure 3.10. Experimental Velocity Vector and Surface Plot - Experiment 4..... 138

Figure 3.11. Experimental Velocity Vector and Surface Plot - Experiment 5..... 139

Page

Figure 3.12. Experimental Velocity Vector and Surface Plot - Experiment 6..... 140

Figure 3.13. Experimental Velocity Vector and Surface Plot - Experiment 7..... 141

Figure 3.14. Experimental Velocity Vector and Surface Plot - Experiment 8..... 142

Figure 3.15. Experimental Velocity Vector and Surface Plot - Experiment 9..... 143

Figure 3.16. Experimental Velocity Vector and Surface Plot - Experiment 10..... 144

Figure 3.17. Variation of Air Holdup in Experimental Tank with Air Flowrate..... 145

Figure 3.18. Variation of Air Holdup in Experimental Tank and Zinc Slag Fuming Furnace with Modified Froude Number..... 146

Figure 3.19. Mean Cell Kinetic Energy of Experimental Measurements as a Function of Air Flowrate..... 147

Figure 3.20. Mean Cell Kinetic Energy of Non-Surface Cells in Experimental Measurements as a function of Air Flowrate..... 148

Figure 3.21. Variation of Experimental Mean Cell Kinetic Energy with Air Input Energy..... 149

Figure 3.22. Bubble Formation at Tuyeres, $N_{Fr'}$ = 0.4..... 150

Figure 3.23. Bubble Formation at Tuyeres, $N_{Fr'}$ = 2.3..... 151

Figure 3.24. Bubble Formation at Tuyeres, $N_{Fr'}$ = 15.6..... 152

Chapter 4

Figure 4.1. Schematic Description of Boundary Conditions Necessary to Describe the Flow in the Experimental Tank..... 153

Figure 4.2. Velocity Fluctuations in a Finite-Difference Cell Computed by SOLASMAC Method..... 154

Page

Figure 4.3. Finite Difference Grid Used to Compute Flow in Experimental Tank..... 155

Figure 4.4. Flowchart of the SSMCR Program..... 156

Figure 4.5. Diagram of Free Surface Location and Movement Technique as used in SSMCR..... 157

Figure 4.6. Recognition of Surface Orientation for Tangential Stress Condition..... 158

Chapter 5

Figure 5.1. Diagram of Problem used to Test SSMCR..... 159

Figure 5.2. Agreement Between Predictions Made by SSMCR and SOLASMAC for Flow in a Square Cavity..... 160

Figure 5.3. Erroneous Prediction of Square Cavity Flow..... 161

Figure 5.4. Correct Prediction of Square Cavity Flow..... 162

Figure 5.5. Prediction of Experimental Flow Regime Made by Constant Velocity Condition, μ_{eff} = 10 g/cm•s..... 163

Figure 5.6. Prediction of Experimental Flow Regime Made by Constant Velocity Condition, μ_{eff} = 40 g/cm•s..... 164

Figure 5.7. Prediction of Experimental Flow Regime Made by Constant Velocity Condition, μ_{eff} = 400 g/cm•s..... 165

Figure 5.8. Prediction of Experimental Flow Regime Made by Variable Density Condition..... 166

Figure 5.9. Prediction of Experimental Flow Regime Made by Variable Density Condition with Left Wall Velocity..... 167

Figure 5.10. Prediction of Experimental Flow Regime Made by Pulsed Boundary Condition..... 168

Figure 5.11. Prediction of Experimental Flow Regime Made by Collapsing Surface Condition, T = 0.5 s..... 169

Figure 5.12. Prediction of Experimental Flow Regime Made by Collapsing Surface Condition, T = 0.7 s..... 170

Page

Chapter 6

Figure 6.1. Prediction of Flow Regime in a Copper Converter Made by Constant Velocity Boundary Condition..... 171

Figure 6.2. Prediction of Flow Regime in a Copper Converter Made by Collapsing Surface Condition..... 172

Figure 6.3. Prediction of Flow Regime in a Zinc Slag Fuming Furnace Made by Collapsing Surface Condition..... 173

Figure 6.4. Prediction of Flow Regime in a Zinc Slag Fuming Furnace Made by Constant Velocity Condition..... 174

Figure 6.5. Prediction of Flow Regime in a Zinc Slag Fuming Furnace Made by Variable Density Condition..... 175

NOMENCLATURE

A_{column}	Area of bubble column (m^2) = depth of column x bubble forward penetration
A_{tank}	Area of tank face (m^2)
$\bar{D}_{dist}$	Mean cell distribution deviation (-)
$\bar{D}_{\theta}$	Mean cell angular deviation (degrees)
div	divergence (s^{-1})
$\dot{E}_{buoyant}$	Buoyant energy input rate (watts)
$\bar{E}_{cell}$	Mean cell kinetic energy
$\dot{E}_{input}$	Total energy input rate (watts)
$\dot{E}_{kinetic}$	Kinetic energy input rate (watts)
g	Acceleration due to gravity (9.8 m/s^2)
H	Depth of tank (m)
h	Height of free surface above arbitrary datum (m)
i	Column number (-)
j	Row number (-)
N	Number of experimental cells containing data (-)
n_i	Number of columns (-)
n_j	Number of rows (-)
p	Pressure (Pa)
Q	Air flowrate (m^3/s)
R	Equivalent radius of tank (m)
t	time (s)

u	Horizontal fluid velocity (m/s)
v	Vertical fluid velocity (m/s)
V_{max}	Maximum velocity (m/s)
w	Transverse fluid velocity (m/s)
x	Horizontal axis (-)
y	Vertical axis (-)
z	Transverse axis (-)

Greek Symbols

α	Gas fraction (-)
γ	Fractional upwind difference parameter (-)
θ	Surface inclination (degrees)
μ	Viscosity (g/cm•s)
ξ	Vorticity (s^{-1})
ρ	Density (kg/m^3)
τ	Stress (Pa)
ϕ	Tuyere Diameter (m)

Subscripts

c	calculated
e	experimental
eff	effective
f	fluid
l	laminar
g	gas
t	turbulent

Superscripts

$t+\Delta t$	next time step
'	time dependent

Dimensionless Groups

N_{Fr}	Froude Number, $u_g^2/g \cdot \phi)$
$N_{Fr'}$	Modified Froude Number, $\frac{u_g^2}{g\phi} \cdot \frac{\rho_g}{\rho_f - \rho_g}$
N_{Re}	Nozzle Reynolds Number, $\frac{\phi \rho_g u_g}{\mu_g}$

ACKNOWLEDGEMENTS

The author wishes to express his sincere appreciation to:

Dr. G.G. Richards for his helpful supervision and great patience.

Mrs. J. Richards for her instructions on the operation of the LDV.

Mr. P. Wenman for drawing many of the graphs and figures.

Mrs. M. Jansepar for typing, correcting and helping to prepare this thesis.

And to my fellow graduate students and friends for their interesting discussions, support and encouragement.

Financial support for this work was obtained from the Natural Sciences and Engineering Research Council.

1. INTRODUCTION

The injection of air into a vessel through a number of horizontal side-mounted tuyeres is a common practice in the non-ferrous metallurgical industry. In particular, side-blowing of air is carried out in the Peirce-Smith copper converter, and the zinc slag fuming process (1). This is contrasted with the top and bottom blown vessels currently used in the ferrous industry (2).

Unlike the case of top and bottom blowing, relatively little research has been performed on the description of the fluid flow regimes within side-blown metallurgical vessels (3,4,5). The major objective of this work was therefore to develop a mathematical model capable of predicting the flow regimes within side-blown furnaces. Due to its industrial importance, particular emphasis was placed on the description of the fluid flow profile in a Peirce-Smith copper converter. In addition however, predictions were also made for the slag flow in the zinc slag fuming furnace.

1.1. Copper Smelting

The production of copper is of great importance to the industrialized world. Used mainly in electrical components, annual world copper production exceeds 8 million metric tons, with proven reserves of 550 million metric tons (1982 Figures) (6). In Canada, copper production is a billion dollar industry: approximately 650,000 metric tons are produced annually, and accounts for 2.4% of all exports (6).

Throughout the world, most copper is found in the form of sulphide ores, either chalcocite (Cu_2S), chalcopyrite ($CuFeS_2$) or covellite (CuS). Mineable copper ores are typically low-grade - 3 wt.% or lower, depending upon current prices. Since the early 20th century, copper has been produced from these ores by the following procedure:

1. The ore is crushed and concentrated by flotation. This concentrate is usually between 15 and 35% copper, the remainder being mainly iron, sulphur and gangue.
2. The concentrate is roasted eliminating some of the sulphur as SO_2.
3. The calcine is melted in a reverberatory furnace. Slag (containing silicates, FeO and some copper and sulphur) is removed, and the matte (a mixture of Cu_2S and FeS) is tapped off.
4. The matte is placed in a copper converter. Silica flux is also added to the matte at this time. The conversion of the matte to metallic copper in this furnace is carried out by blowing air through the matte in two stages:

a) slagmaking:

The iron sulphide in the matte preferentially oxidizes to FeO and sulphur dioxide:

$$FeS + 3/2\ O_2 \rightleftharpoons FeO + SO_2 \qquad (1.1)$$

This oxidation releases a great amount of heat, and proceeds autogenously. The sulphur dioxide, nitrogen, and unreacted oxygen rise through the melt and are drawn out of the converter mouth. The FeO combines with the silica flux to form a slag on the surface of the bath. Periodically, the slag is poured out of the converter, more silica and matte are added, and the process is continued.

b) blister making:

Once all of the iron has been removed from the melt, the molten copper sulphides are oxidized to copper by further blowing of air:

$$Cu_2S + O_2 \rightleftharpoons Cu + SO_2 \qquad (1.2)$$

This produces "blister copper" which is approximately 99% pure with the remainder largely oxygen and precious metals.

5. The blister copper is normally reduced in an anode furnace and then cast into electrodes and refined electrolytically. This yields 99.98% pure copper, and "anode slimes" from which any precious metals can be extracted.

Over the years, many improvements have been made in this smelting process. The roasting and reverberatory steps have been eliminated in the new "flash-smelting" techniques. These methods utilize the heating value of the sulphur in the ore to accomplish melting. They are therefore far more

energy efficient than earlier methods. Despite such general improvements however, the vast majority of the copper produced in the world today still involves the oxidation of sulphide matte in a copper converter.

1.2. The Copper Converter

1.2.1. History and Development

By far the most common type of copper converter in use today is the Peirce-Smith side-blown converter (Figure 1.1). The design of this vessel arose from research in the mid-19th century. Bottom blown Bessemer-type converters were found to be unsuccessful due to the blockage of the tuyeres by frozen copper matte. As well, the refractory was found to be strongly attacked by the silica slag. In 1905 Messrs. Peirce and Smith conducted successful tests on a side-blown cylindrical vessel with a basic refractory lining. Within a few years, the Peirce-Smith converter was in use world-wide.

1.2.2. Difficulties

Despite its success and wide use, the design of the Peirce-Smith converter has several serios problems:

1. Because the air is blown into the converter at low pressure and consequently in the form of bubbles, the bath is able to wash up against the tuyeres (7). Cooled by the incoming air, matte in this region solidifies to form accretions which eventually completely block the

tuyeres (7). In order to maintain blowing rates, the plug of frozen matte must be "punched" periodically. In addition to its overall inefficiency, this punching of the tuyeres is thought to add greatly to refractory wear.

2. At certain air flowrates and bath depths, the matte in the converter may "slop" uncontrollably. This may result in the ejection of molten matte from the top of the converter and cause great danger to operating personnel in the immediate vicinity. Dust losses and the build up of material at the converter mouth may also become excessive under these conditions (8).

1.3. The Zinc Slag Fuming Furnace

A diagram of the zinc slag fuming furnace is shown in Figure 1.2. Zinc slag fuming is topologically similar to the copper converting process in that it involves gas injection from multiple, horizontally oriented tuyeres into a molten bath.

Zinc slag fuming is a process whereby molten slag from lead smelting (containing up to 20% ZnO) is reduced by the action of coal injected into the furnace. The reduced zinc leaves the bath as a vapour, where it is re-oxidized, and removed by the furnace off-gases.

The kinetics of the slag fuming furnace have been extensively studied (9,10). However, the general lack of accurate information on the bath circulation velocity has limited the applicability of mathematical models describing this process (9,10).

1.4. Objectives of the Work

The primary objective of the research performed in this work was to develop a mathematical model that was capable of describing the fluid flow regime in horizontally injected metallurgical processes.

For the case of the copper converter, such a model has several obvious applications.

1. To yield insights of the general flow patterns and stirring within conventional copper converters.
2. To provide input data for sophisticated heat and mass transfer models of the converter. To date, the development of such models has been hampered by a lack of information on the bath circulation velocity. In turn, such models can provide information to optimize the production of current copper converters, and aid in the design of more efficient vessels.
3. To study and possibly suggest ways of preventing bath slopping.

Similarly, the application of such a model to the zinc slag fuming furnace will provide information, previously unavailable, on the bath recirculation velocities. When considered along with kinetic models (9,10) this has application to the optimization of the furnace operating conditions.

2. LITERATURE REVIEW

As described in Chapter 1, a major objective of this study was to provide a mathematical description of the fluid flow regimes in the Peirce-Smith copper matte converter and the Zinc Slag-Fuming furnace. As gas injection into a liquid bath is the central feature of each of these processes, the scientific literature was searched in the following fields:

1. Studies of the flow regimes in non-ferrous reactors.
2. Experimental studies of simple bubble formation in water and liquid metals.
3. Investigations of the flow regimes in other gas-driven flow systems. These studies are largely concerned with inert-gas injected ladles and gas lift systems.
4. Numerical methods capable of predicting the velocity and pressure regimes within a copper converter and a zinc slag fuming furnace. This review will be discussed in detail in Chapter 4.

2.1. Flow Regimes in Non-Ferrous Metallurgical Reactors

Among the first to consider the fluid flow fields in copper matte converting was Themelis et al. (3). Based on air-water jet injection studies, Themelis et al. estimated the fluid flow regime within a copper converter to be as shown in Figure 2.1.

Based on the assumptions of Themelis et al., Nakanishi and Szekely (4) formulated a fluid flow model of domain "A" in Figure 2.1. The results of their calculations are shown in Figure 2.2, and show the maximum calculated velocities to be about 5.0 m/s.

However, the studies of Oryall (11) and Oryall and Brimacombe (12) showed that the model of Themelis et al. was unable to predict the behaviour of an air jet in liquid metal. The jet cone angle measured by Themelis et al. in water (20 degrees) was found to be 155 degrees in mercury. In addition, bubbles in mercury were found to rise almost vertically, with very little forward penetration. These findings threw doubt upon the accuracy of the description shown in Figure 2.2.

Industrial measurements performed by Hoefele and Brimacombe (7) on a Nickel converter showed that the air enters this vessel in the form of bubbles - at a formation rate of 10 s^{-1} - and not as a jet as was thought by Themelis et al. (3). The bubble formation frequency of 10 s^{-1} agreed well with that found accoustically by Irons and Guthrie (13) in a bath of liquid iron. However, this low frequency indicated large bubbles (estimated diameters of 0.40 to 0.68 m) and hence the possibility of bubble coalescence occurring. The laboratory measurements of Hoefele and Brimacombe (7) of gas injection into water, mercury and Zinc (II) Chloride solution indicated that the transition between bubbling and jetting phenomena could be related to the modified Froude number and the ratio between the gas and liquid densities. This criterion (similar to the injection number condition employed by Wraith and Chalkley (14)) is illustrated in Figure 2.3. Bubbling behaviour is

clearly predicted for matte converting. Plotting relevant operational data for the slag fuming furnace on Figure 2.3 indicates that this too is operating in a bubbling mode.

A mathematical model formulated by Ashman et al. (15) was used to study the reaction kinetics and oxygen utilization efficiency in a copper converter. A modified version of the bubble formation model proposed by Davidson et al. (16) was employed. Data was not available for the bath recirculation velocity (upon which bubble formation depended strongly). Therefore, this parameter was varied independently until the predicted bubble formation frequency was approximately equal to that measured by Hoefele and Brimacombe (7). Using this method, the vertical velocity of the liquid matte in the region of the tuyeres was calculated to be between 1.2 and 2.6 m/s.

Industrial trials carried out by Bustos et al. (17) on an operating copper converter and a zinc slag fuming furnace showed that the bubbling behaviour in these vessels is more complex than was previously believed. Analysis of tuyere pressure measurements indicated that the copper converter behaves differently depending upon the state of its refractory lining. The bubbles forming at the tuyeres of a newly-lined copper converter were shown to rise independently, and not to interfere significantly with one another. However, after several heats (and corresponding refractory wear) the bubbles arising from adjacent tuyeres were found to interact with one another, forming a large, unstable gas envelope in the region of the tuyeres. The bubbles in the slag fuming furnace were found to act independently under all testing conditions at a frequency of 5-6 s^{-1}.

Unfortunately, no studies were found that predicted the complete fluid flow regimes in either the copper matte converter or the zinc slag fuming furnace as has been done for argon-stirred ladles.

2.2. Bubble Formation Investigations

The behaviour of gas bubbles injected into water has been extensively studied. The earlier literature concerning bubble formation in aqueous systems have been thoroughly reviewed by Kumar and Kuloor (18), Themelis, et al. (3) and Clift, Grace and Weber (19). Among the more significant studies were those performed by Davidson and co-workers (16) and Wraith and Chalkley (14).

The behaviour of air bubbles injected into a liquid (from a single tuyere) has been summarized by Oryall (11) as follows:

1. At very low air flowrates ($N_{Re} < 500$) the bubble volume is relatively invariant with gas flow. Therefore, the bubble frequency of formation varies with gas flowrate in this low-flow condition.
2. At higher air flows ($500 < N_{Re} < 2100$), the bubble formation frequency remains almost constant (at approximately 8-10 s^{-1}), hence bubble volume increases with increasing air flowrate in this regime. Simple models (15) have been formulated (based only upon a balance of buoyancy force and inertia) yielding formulae for bubble volume that agree well with experiment, though nozzle diameter effects have been seen to be significant.

3. Increasing air flowrates further causes significant interaction between rising bubbles. Wraith and Chalkely (14) and Nilmani and Robertson (20,21) have investigated the effects of bubble-bubble interaction. Two different effects, termed "binary coalescence" and "stem coalescence" have been found to occur at low and high air flowrates respectively. The transition between these two types of behaviour is determined by gas momentum. Stem coalescence occurs when the bubbles elongate and form columns of air that reach the surface and break up unpredictably.
4. At higher flowrates still, ($N_{Re} > 10{,}000$, $N_{Fr} > 1000$) the bubbling behaviour ceases altogether, and the gas enters the liquid as a turbulent jet.

It is generally agreed that the transition between these types of behaviour are dependent upon increasing gas momentum. The nozzle Reynolds number (11) was initially used to predict the transition between "bubbling" and jetting phenomena. As mentioned above, Hoefele and Brimacombe (7) used the modified Froude Number as an indicator of this gas momentum effect, and successfully predicted the transition between "bubbling" and "jetting" regimes. The injection number has been used similarly by Wraith and Chalkely (14) to correlate the effect of gas momentum for air injection into both water and liquid metal.

2.3. Investigations of Gas-Driven Fluid Flow

2.3.1. Experimental Studies

One of the earliest investigations of the velocity fields set up by air injected into water was that performed by Bulson (22). The conclusions formed from this large-scale study may be summarized as follows:

1. A stable recirculation pattern was clearly observed at all air flowrates tested.
2. The maximum water velocities were found to occur at the surface.
3. This maximum water velocity was found to be directly related to the cube root of the air injection rate.

Unfortunately, Bulson did not provide sufficient information to allow later calculation of the modified Froude Number of the injected gas.

A large number of studies on gas-lift systems have been reported in the Chemical Engineering literature. For example, Kumar et al. (23) correlated the liquid recirculation rate with the dimensionless gas flowrate. In addition, the gas holdup in the column was shown to be directly related to the injected gas flowrate.

Some of the earliest experimental measurements that directly applied to metallurgical operations were performed by Szekely and Asai (24). They studied the general recirculation pattern of water in an air-injected physical model of a steel ladle using photography. This was largely a

qualitative study, used in conjunction with a mathematical model (25).

Szekely, Wang and Kiser (26) measured the velocity field in a water-filled plexiglass model of a ladle, by a combination of hot-wire anemometry and photographic techniques. Air was introduced through a vertically-oriented tuyere at the bottom of the tank at a flowrate of .2 l/s (a modified Froude Number of 1.3). Water velocities were measured at 24 different points in the model, and the general recirculatory nature of the flow was clearly discerned.

Salcudean and Guthrie (27,28,29) employed two physical models in their study of the fluid flow generated while tapping ladles. Although primarily a liquid injection study, the effect of air entrainment on the fluid velocity distribution was observed.

Szekely, Dilawari and Metz (30) also used a physical model of a ladle, but employed a motor-driven belt, rather than gas bubbles, as the means of generating the recirculatory flow regime. Laser-doppler measurements of the flow pattern were made. This investigation was primarily for the purpose of validating a mathematical model, and was not intended as a rigorous physical description of gas-liquid interaction.

In a following paper, Szekely, El-Kaddah and Grevet (31) carried out laser-doppler measurements of the flow in an air-injected water model of a 6 ton ladle. Two air flowrates were considered, 12.3 Nl/min and 25 Nl/min, corresponding to (modified) Froude Numbers of .021 and .080 respectively.

At each flowrate, the water velocity in the plexiglas model was measured at 26 different locations.

Hsiao, Chang and Lehner (32) measured gas plume velocities in a 1/7 scale water model of a ladle. The maximum water velocity was found to occur at the fluid surface and was found to be related linearly to the cube root of the air injection rate.

A comprehensive analysis of gas-stirring was performed by Sahai and Guthrie (33,34) who carried out experiments in a .17 scale model of a 150 ton ladle. The gas was introduced into the tank through an immersed, downward directed lance, at a Modified Froude Number of about 650. The velocity profile within the tank was measured by a photographic technique: the motion of small seed particles within the tank was recorded at different times, and their velocity was assumed to be the same as the water velocity. These measurements were carried out in 106 different locations in the tank.

Oesters, Dromer, and Kepura (35) employed hot wire anemometry to measure the velocity field in a water model of a ladle. Both bottom blowing (through a perforated plate) and top blowing (through a lance) were studied. An equation based on the studies of Hsiao et al. (21) was formulated and shown to give a good estimate of the velocity in the gas plume. Two injection rates were studied: 3 1/s and 1.2 1/s, corresponding to modified Froude numbers of 2 and 32 respectively. In addition, the "mixing time" in the ladle as a function of air flowrate was shown to decrease with air flowrate asymtotically to a minimum.

Mazumdar and Guthrie (36) studied the flow in a .3 scale model of a 150 ton ladle. Photographic techniques and the motion of small threads immersed in the flow were used to measure the velocity profiles. Injection was carried out at a Froude number of approximately 2.

An investigation by Haida and Brimacombe (37) confirmed the existence of a maximum in the stirring efficiency of an air-driven water model. Electrical probes were used to study the shear stress of the liquid at the wall (which is directly related to the velocity of the fluid) at various air injection rates. At a modified Froude Number of approximately 50, this shear stress was seen to reach a maximum. This was explained as being due to the onset of gas "channelling" through the liquid, and a means of predicting this behaviour was derived.

2.3.2. Numerical Studies

As with the experimental work, virtually all effort in this field has been concerned with calculating the fluid flow regime in argon-stirred ladles.

Drawing on earlier work by Gosman et al. (38), Szekely and Asai (24,25) formulated a mathematical model of the turbulent recirculating flow fields in an inert-gas stirred ladle. Two dimensional flow was assumed and the Kolmogorov-Prandtl single equation model was used to calculate the turbulent viscosity. The solution was performed in stream function and vorticity. The free surface was assumed to be horizontal, and to be of zero

vorticity. Reasonable qualitative agreement was found with visual experimental observations, although quantitative comparisons of the calculated flow field with experimental results were not made.

In the mathematical segment of the work performed by Szekely et al. (26), the k-W technique proposed by Spalding (39) was used to model the turbulent viscosity in a two dimensional mathematical model of an experimental ladle. They neglected free surface effects, and considered the bubble column to apply a constant upward velocity to adjacent fluid. Again, fair qualitative agreement was found with experiment, but actual velocities were found to be up to an order of magnitude different from computed velocities.

Deb Roy, Majumadar and Spalding (40) also used a two-dimensional mathematical model in an attempt to predict the flow regime in an air-stirred water model (31) of a ladle. An algebraic model, proposed by Pun and Spalding (41), was used to calculate the turbulent viscosity. The bubble-water boundary condition was modelled by varying the density in this boundary region according to a "void fraction" - the amount of space occupied by the bubbles. Two separate methods of calculating this void fraction were then tested.

1. No slip. The air moves with the same velocity as the liquid.
2. Slip. The bubbles move through the liquid at their terminal velocity.

In all cases, the free surface was considered to be a horizontal, non-retarding wall. These calculations were found to yield better agreement with experiment than those published by Szekely et al. (26).

Szekely, Dilawari and Metz (30) used a model similar to Szekely et al. (26), but applied wall functions in the region of the walls to better approximate these boundaries. Good agreement was found between the model predictions and experiments in which the recirculation of the bath was caused by a motor-driven belt, rather than by bubbles. This indicated that the main reason for the differences between previous calculations and experiments was due to inaccurate approximations of the bubble-liquid interface. When this boundary was simplified to a form that was easily approximated mathematically (a belt-driven system), good agreement was observed between calculations and experiments.

Again neglecting deformation of the free surface, Szekely, El Kaddah and Grevet (31,42,43) employed the improved approximation of the bubble boundary suggested by Deb Roy et al. (40) and calculated the flow regime in a gas-agitated system. Velocity fields were calculated based on both the k-W model and the algebraic model of Pun and Spalding (41). The algebraic model was found to yield acceptable results, and was much less expensive in computer time. However, considerable differences between experiment and calculations were still observed.

Sahai and Guthrie (44) proposed a new algebraic relation for a constant effective viscosity, deliberately designed for bubble-driven systems

(the viscosity model of Pun and Spalding (41) was based on the action of turbulent jets). In two succeeding papers (33,34) they examined the mathematical description of the bubbling mechanism and developed a relation for mean bath recirculation velocity and bubble plume velocity. In addition, they formulated a turbulent model, based on Patanker and Spalding's (45) SIMPLE algorithm. This model was found to give good qualitative agreement with experiments.

The first to examine the effects of the free surface were Salcudean, Low, Hurda and Guthrie (46). A three dimensional model was written that used a Marker and Cell (MAC) type method to describe the deformation of the free surface. The description of the bubble-liquid boundary suggested by Deb Roy et al. (40) was employed as was the viscosity model of Pun and Spalding (41). Calculations were performed for symmetrical and off-centred gas injection. Reasonable agreement was found both with two dimensional calculations (40) and with experimental results. A three dimensional, steady state, turbulent model formulated by Salcudean and Wong (47) was also compared to these calculations.

Salcudean, Lai and Guthrie (48) and Mazumdar and Guthrie (49) extended these calculations to compare the accuracy of the turbulent viscosity models proposed by Sahai and Guthrie (44) and Deb Roy et al. (40) with the k-ε model of Jones and Launder (50). All models were compared with the experimental results of Oeters et al. (35). Surprisingly, the fluid profiles predicted by the algebraic models were closer to experimental values than were the results calculated from the k-ε model. This was thought to be

due to the influence of buoyancy and curvature effects, as well as inaccuracies introduced by upwind differencing.

2.4. Conclusions

From the literature mentioned above, a number of conclusions can be made about the prediction of the flow regimes in the copper matte converter and the zinc slag fuming furnace:

1. The air enters these vessels in the form of bubbles. Therefore the mathematical method used to model the flow in these vessels should be one that is capable of modelling flow induced by bubble injection.
2. The study of Salcudean et al. (48) has shown that for the computation of flow in a ladle, the complex $k-\varepsilon$ differential model of turbulence does not yield as accurate results as the simple algebraic viscosity model of Sahai and Guthrie (44).
3. A number of mathematical approximations have been used to describe the stirring effect of bubbles in liquid ladles. The most successful of these to date has been the variable density or void fraction model of Deb Roy et al. (40).
4. Independent air-injection studies by Hsiao et al. (32) and Bulson (22), under very different conditions, have shown that the maximum liquid velocity frequently occurs at the surface of the vessel. This velocity may be related to the cube root of the air injection rate.

3. EXPERIMENTAL

3.1. Objectives

The two major objectives of the experimental portion of this work were as follows:

1. To provide a quantitative description of the stirring of a liquid by air bubbles, at injection conditions similar to the industrial processes of copper converting and zinc slag fuming.
2. To verify a mathematical model written to describe both the experimental and the industrial systems.

3.2. Apparatus

The experimental apparatus used in this investigation is shown schematically in Figure 3.1. The two major components of this system were a water-filled plexiglass tank and a laser-doppler velocimeter.

The design of the water tank assembly was determined by the following criteria:

1. Rectangular in cross section.
2. Air injected from a series of horizontal side-mounted tuyeres.
3. Open at the top.

4. Adjacent tuyeres do not interact significantly at low air flowrates.

The tank was chosen to be rectangular in cross section to simplify both velocity measurements and later mathematical modelling. A rectangular computatational domain allows finite-difference calculations (which are carried out in a rectangular grid) to be performed easily - therefore a rectangular tank is much simpler to treat in this manner than tanks of other shapes. Further, it is difficult to obtain laser-doppler velocity measurements in a tank with surfaces not normal to the incident laser beam, due to refraction of the laser light. For example, it is hard to obtain laser-doppler measurements at all positions within a cylindrical tank. Therefore a rectangular tank was constructed to allow measurements to be made easily at all positions.

Side-blowing of air from more than one tuyere was specified for two reasons:

a) The metallurgical processes of interest in this study (copper converting and zinc slag fuming) are side-injected.
b) There already exist many excellent studies of stirring by a single, vertically oriented tuyere.

The surface of the bath was unconstrained to achieve similarity with the metallurgical processes of interest.

The spacing between the tuyeres was given much design consideration as it has been shown by Bustos et al. (17) that the interaction of bubbles forming at adjacent tuyeres is a significant effect in nickel matte converting and copper converting. To investigate this effect experimentally, a tuyere spacing was sought in the experimental tank that would prevent or permit the coalescence of bubbles at adjacent tuyeres depending on air flowrate. Preliminary experiments were performed to determine the appropriate minimum tuyere spacing to achieve interaction at Froude Numbers approximating those used in copper converting. This distance was found to be approximately 2.5 cm.

Provision was made to blow air from two sides of the tank if so desired. Two-sided gas injection was the source of qualitative data only, and is discussed in Chapter 6.

Note that exact dimensional similarity with a zinc slag fuming furnace or a copper converter was not a design criterion. The tank constructed for the purposes of this study was not, nor was it intended to be, a physical model of any metallurgical process in particular. In fact, the aforementioned design criteria effectively rule out any possible direct correspondence between the dimensions of the experimental tank and either of the two metallurgical process vessels of interest to this study. Rather, the purposes of the velocity measurements carried out in this tank were both to verify, and to provide input data for, a mathematical model of the flow regimes within a copper converter and a zinc slag fuming furnace. In particular, a means of characterizing the interaction of air bubbles with a

surrounding liquid was of primary importance. Therefore, the actual physical dimensions of the experimental tank were not important, provided that they facilitated velocity measurements and subsequent mathematical modelling.

However, simply because rigid physical similarity does not exist between the experimental tank and the two industrial processes of interest, this does not necessarily imply that the measured velocity profiles were completely inapplicable to these processes. Despite all differences, similarity of the modified Froude Number was maintained throughout these experiments, indicating that the bubble behaviour that occurred in the experimental tank was similar to that occurring in the industrial cases. It is primarily the interaction of these bubbles with the surrounding liquid with which this study is concerned.

It is not claimed that the velocity measurements made within this tank are identical to those occurring industrially, but rather that there exists (if only qualitatively) similarlity of the interaction mechanism between the gas bubbles and the surrounding fluid. Despite such obvious complications as the non-wetting characteristics of liquid metals, and the difference between liquid interaction with reacting and non-reacting gases, the results of this experimental study will still be generally applicable to zinc slag fuming and copper converting for two reasons:

1. In all of these processes, a liquid bath is stirred wholly by incoming gas that enters the vessel in the form of bubbles. Thus even though

various liquid characteristics vary among the three processes, the basic method of stirring remains the same: lifting and shearing of the surrounding liquid by air bubbles.

2. A mathematical model that is capable of describing the flow regime within the experimental tank should therefore be capable of extrapolating these results to industrial processes, with greater confidence than calculations based simply on assumptions about the bubble-stirring mechanism.

With these conclusions in mind, the internal dimensions of the plexiglass tank were designed to be 30 cm x 20 cm. The tank was made 60 cm tall to prevent escape of liquid by splashing. Five holes, each 1.0 cm in diameter, were drilled along two sides of the tank at 2.5 cm intervals, and located 3.0 cm above the tank bottom. Water-tight fittings were placed in each of these holes through which 0.6 cm diameter nylon tubing was inserted, forming tuyeres (Figure 3.2).

Air was introduced into these tuyeres through the manifolds shown in Figure 3.2. These manifolds were constructed of 3/8 in. PVC tubing and hoseclamps. Great care was taken in their construction to ensure that the air flow out of each tuyere was identical (this was verified by successive rotameter measurements of each tuyere).

The air flow into the tank was measured by a calibrated rotameter attached to a manometer (Figure 3.1).

The laser-doppler velocimeter (LDV) consisted of a 15 mW Spectra-Physics Helium-Neon laser connected to optics and data-collection electronics manufactured by TSI Inc. The detailed operation of an LDV has been outlined elsewhere (65,66) and will not be discussed here.

The velocity of the water in the tank was measured within a region of space 1.8 cm long, defined by the intersection of two laser beams (Figure 3.3). The value recorded as the water velocity at a particular point in the tank was actually an average of 512 separate velocity readings taken from anywhere within this 1.8 cm measuring length. The LDV was only capable of measuring one component of the fluid velocity at any one time, (either horizontal or vertical) but the orientation of the refracting optics could be altered to allow later measurement of the other component.

The entire laser-doppler apparatus was mounted on a computer-controlled traversing table. This table was constructed so that it could position the measuring volume of the LDV at any position in the cross-section of the tank with an error of less than 1.0 mm.

Data collection was also performed by computer. At each point within the tank, the LDV sent 512 independent water velocity measurements to an Apple IIe microcomputer. The computer then averaged these measurements, and printed the result (along with the standard deviation of the points) on the screen and saved these values on disk.

3.3. Procedure

The laser-doppler measurements were carried out in the central vertical plane of the experimental tank, in a 10 x 10 grid with points spaced 3.0 cm apart (Figure 3.4). Each separate square region within this grid is termed a "cell", due to the similarity between this experimental mesh, and a finite difference grid. Velocity measurements were carried out in the centre of each of these cells, as shown. The numbered cells correspond to the measurement locations mentioned in Figures 3.5 and 3.6.

Velocity measurements were carried out at ten separate air flowrates, ranging from 38 to 220 std l/min. (Table 3.1).

Due to the inability of the LDV to measure both horizontal and vertical fluid velocity components simultaneously, a complete experimental run involved two complete sweeps over this mesh of 100 cells. On the first sweep the horizontal component was measured, and the optics were then adjusted to measure the vertical component. The second sweep was then performed, measuring the vertical water velocity in each of the 100 positions in the tank.

The experimental procedure was therefore very straightforward:

1. The tank was filled to its desired operating level (always 30.0 cm) with distilled water.

2. Seed particles (small plastic spheres measuring 2.0×10^{-6} m in diameter) of neutral buoyancy were added to the water in the tank.
3. The tank was positioned perpendicular to the laser, and its exact position relative to the LDV was recorded.
4. The air supply was switched on and set to the desired flowrate by observing the rotameter/manometer assembly.
5. The traversing table, computer, and LDV were switched on.
6. The data collection and traversing program was run on the computer.

After these preliminary steps had been performed, the traversing-table LDV system performed the following tasks, with little or no intervention:

7. The traversing table positioned the laser at a point in the 100 point scan.
8. The LDV made 512 separate measurements of the (horizontal or vertical) fluid velocity at this new location.
9. These values were transferred to the computer, which averaged them and stored the mean and standard deviation on a floppy diskette. The computer then calculated the next location for the traversing table, and gave these instructions to the computer controlling the table.

Steps 7 to 9 were repeated as necessary until velocity measurements had been taken in each of the 100 locations.

Once both velocity traverses had been completed, the shape of the water surface was traced onto a piece of clear plastic. This surface shape was later digitized, and stored on a mainframe computer along with the velocity data, allowing later analysis and plotting.

The only serious difficulty encountered in implementing this procedure arose from the presence of smaller air bubbles remaining in the water near the surface and left wall. These bubbles randomly blocked and scattered the light from the laser beam, sometimes causing a very long period of time to elapse before 512 water velocity measurements could be taken. Further, this scattering of the laser could cause spurious velocity measurements if the LDV happened to measure the velocity of a passing bubble, rather than the surrounding water. This problem was overcome by introducing very small and precisely sized seed particles into the water tank. This then enhanced signal quality, and permitted the LDV to distinguish between particles and bubbles.

3.4. Experimental Results

3.4.1. Introduction

In addition to the water velocity and surface profile measurements, a number of general observations have been made on the experimental system as a whole:

1. The air was seen to enter the tank in the form of bubbles at all flowrates tested. This was expected since even the maximum experimental modified Froude number used (15.5) was well within the bubbling regime for water (7).

2. As designed, adjacent tuyeres did not interact significantly at low air flowrates. However, both photographs and visual observations indicate that at air flowrates greater than approximately 90 standard litres per minute, bubbles rising from adjacent tuyeres interfered with one another, and did not rise in separate, discrete columns. This corresponded to a modified Froude number of 2.32.
3. The bubble column was seen to be confined to the region around the left wall, only penetrating 2 to 3 cm into the bath.
4. The tank was observed to oscillate slightly while velocity measurements were being taken. This occurred because the tank was not securely anchored, but was simply placed on a supporting table. Various attempts were made to prevent this action, but none was completely successful. This vibration was not severe (a deflection of approximately ± 2 mm at its worst) and it is unlikely that it affected the velocity measurements significantly for the following reasons:

   a) There were no significant oscillations about the y-axis (Figure 3.1).
   b) Oscillations about the x-axis have a very small effect since the variation of the flow through the depth of the tank is small (see below). Further, velocity measurements were made along a 1.8 cm region defined by the intersection of two laser beams (see Apparatus section in this chapter). Harmonic motion about the x-axis would merely serve to extend this length slightly.
   c) Only vibrational motion about the z-axis would have an effect, however due to the averaging of velocity measurement data, even this effect would be small. Assuming that these oscillations occur symmetrically

about the z-axis, the velocity measurements would be evenly distributed in the region within 2 millimetres to either side of the desired position. Since a velocity measurement at a particular point was used to represent the average velocity of the fluid for 15 mm in each direction, it is unlikely that this effect was significant, compared to the coarseness of the experimental data grid.

3.4.2. Check of the Two Dimensionality of the Flow

Before carrying out any of the complete velocity scans, several checks were made on the variation on flow through the width of the tank. From the point of view of subsequent computer modelling, it would be ideal if the horizontal and vertical velocity components at each of the 100 measurement locations were constant at any point in the tank width. This would be the case of truly two-dimensional behaviour.

However, there were two reasons for suspecting that this type of behaviour would not be observed:

1. The effect of the walls of the tank would be to retard the nearby fluid. Thus, one would expect the water velocity to be lower in the region of the walls than in the centre of the fluid.
2. The stirring of the tank was caused by bubbles injected from a number of adjacent tuyeres. Any significant variation in the air flowrates among these tuyeres could cause a corresponding variation in the local fluid velocity.

To quantify these effects, the variation of the horizontal and vertical components with tank width was measured at four separate locations in the tank (Figure 3.4). When plotted (Figures 3.5 and 3.6) they show that there is, in fact, some variation of flow with width. The wall effect is noticeable and as expected the velocities are higher in the centre of the tank than at the walls. However, the flatness of the profiles (a maximum velocity variation of 10%) indicates that this effect is slight. More importantly, these profiles are relatively symmetrical - indicating that the air flowrates through the tuyeres were equal.

Because of this slight velocity variation, all velocity scans were performed in the central vertical plane of the tank, where the wall effect was least significant. The location of the measuring volume that was used in these scans is clearly seen in Figures 3.5 and 3.6 (the dashed line).

Another, more rigorous, method of checking the two dimensionality of the flow is to apply the principle of conservation of mass to the measured velocity profiles. That is, once all vertical and horizontal velocity measurements had been made at a given air flowrate, the two dimensional continuity equation was applied to each experimental cell. If the horizontal and vertical mass flows into each cell were equal to the horizontal and vertical flows out, then there would be no reason to suspect any transverse flow. Stated mathematically, for an incompressible fluid, the three dimensional continuity equation is:

$$\frac{\partial u}{\partial x} + \frac{\partial v}{\partial y} + \frac{\partial w}{\partial z} = 0 \qquad (3.1)$$

Applying a backward finite difference approximation, this becomes (for an experimental cell):

$$\frac{u_{ijk} - u_{i-1,jk}}{\Delta x} + \frac{v_{ijk} - v_{ij-1,k}}{\Delta y} + \frac{w_{ijk} - w_{ij,k-1}}{\Delta z} = 0 \qquad (3.2)$$

Therefore if the summation:

$$\frac{u_{ij} - u_{i-1,j}}{\Delta x} + \frac{v_{ij} - v_{ij-1}}{\Delta y} \qquad (3.3)$$

is everywhere equal to zero, then $\frac{\partial w}{\partial z} = 0$ and the flow is confined to the vertical plane.

Applying Equation (3.3) to several cells in the velocity vector plot of Figure 3.7 yields the values shown in Table 3.1. It is immediately apparent that Equation (3.3) does not, in fact, equal zero at all locations. However, even with truly two-dimensional experimental flow, there are several reasons why one might expect Equation (3.3) to be non-zero.

1. The equation assumes an incompressible fluid of constant overall density. Both visual observation and photographs have confirmed that there are several regions of the tank (such as near the surface or the bubble column) where the air is entrained in the liquid phase. In these regions, the local density could vary significantly, invalidating Equation (3.3). This effect is shown by considering the variable density form of the

continuity equation:

$$\frac{\partial \rho}{\partial t} + \frac{\partial(\rho u)}{\partial x} + \frac{\partial(\rho v)}{\partial y} = 0 \qquad (3.4)$$

Equation (3.3) assumes ρ = constant. If this is not the case, then the value calculated by Equation (3.3) is erroneous. Unfortunately, without knowing the values of $\frac{\partial \rho}{\partial t}$, $\frac{\partial \rho}{\partial x}$, $\frac{\partial \rho}{\partial y}$, it is impossible to determine the "true" two dimensional divergence for these cells. Therefore any subsequent consideration of the two dimensionality of the flow in the experimental tank will be confined to regions uncontaminated by air bubbles.

2. A further reason why Equation (3.3) might be non-zero arises from the coarseness of the experimental mesh. Equation (3.3) is a finite-difference approximation to the true relationship:

$$\frac{\partial u}{\partial x} + \frac{\partial v}{\partial y} = 0 \qquad (3.5)$$

and this approximation rapidly loses accuracy as mesh size is increased. Accuracy will be most adversely affected in regions where the flow is highly rotational, such as in the central vortex region of Figure 3.7. In this case, the fluid velocity changes strongly with position and there are significant changes in the orientation of the flow vectors from one cell to the next. The velocity at one position may be tremendously different from that measured only a few centimetres away. Thus the continuity equation that applies for the infinitesimal region around this point may bear no resemblance whatever to that for the cell as a whole, and therefore the fact

that Equation (3.3) does not equal zero does not necessarily imply that $\frac{\partial w}{\partial z}$ is finite.

The simplest solution to this difficulty would be to reduce the size of the experimental mesh. Unfortunately, time constraints eliminated this as an option. Therefore further analysis of the two dimensionality of the flow in the tank will be performed on regions in which the velocity vectors are relatively parallel, and do not change greatly with position.

Selecting regions that do not violate the two criteria mentioned above reduces the mean values of $\frac{\partial w}{\partial z}$. These are shown for each set of experimental velocity measurements in Table 3.2. It is clear that the overall flow in the experimental tank was not perfectly two-dimensional. While this is only to be expected, it is important to note for subsequent comparisons between experimental and calculated results that the mathematical model developed in the following chapter was in fact truly two dimensional, and was incapable of considering any transverse flow.

3.4.3. Velocity Patterns

The series of laser-doppler measurements carried out at ten air flowrates between 38 and 220 standard l/min yielded the velocity vector plots shown in Figures 3.7 to 3.16. Each of these plots has been scaled so that the longest velocity vector corresponds to the maximum measured velocity (shown at the bottom of the plot). The border around each plot represents the position of the inside walls of the tank. Cells that do not contain

arrows indicate that it was not possible to obtain velocity measurements at that position (usually due to bubbles blocking the laser beam). Such cells are common at the higher air flowrates and near the surface of the tank. Despite the presence of such "empty" cells, the general recirculatory motion of the flow is clearly observed.

The left-most column of each plot is the region occupied by the bubble column. It was not possible to obtain accurate water velocity measurements in this region, due to the large numbers of bubbles in this region, which block the laser beam.

The expected recirculation pattern is clearly evident in each plot, with the fluid rotating around a quiescent central region. For each velocity vector plot, the highest velocities appear to occur at, or close to, the surface of the bath. Low water velocities occur in the centre of the vortex and in the vicinity of the walls.

A close inspection of the velocity plots reveals notable differencs between those taken at widely different air flowrates. For example, the centre of the vortex in Figure 3.7 (corresponding to a blowing rate of 38 l/min) is in the approximate centre of the tank, while that of Figure 3.16 (at an air flowrate of 216 l/min) is in the upper left corner. Further, such prominent features as the strongly downward-directed velocity vectors in the upper right quarter of Figure 3.16 are not present at all in Figure 3.7: the vectors in this region of Figure 3.7 are horizontal. This shift in the location of the vortex centre and the orientation of the velocity vectors

indicates that there was a significant change in the flow conditions between the lowest and the highest air flowrate. This hypothesis is supported by observing the figures lying between these two extremes. They show a steadily-increasing downward motion of surface velocity vectors, with a corresponding shift in the location of the vortex.

3.4.4. Surface Shape

In addition to velocity vectors, Figures 3.7 to 3.16 also contain the steady state fluid surface profiles. These profiles were obtained by digitizing the traces of the experimental surfaces. As with the vector plots, the surface profiles also show considerable change with air blowing rate.

This variation is emphasized by integration of these surface profiles. By conservation of mass, the volumes defined by each of these curves should all be equal to the volume of the undisturbed bath (18 litres). Performing this integration by the trapezoidal method, (and assuming only a two-dimensional surface variation) reveals that this volume is in all cases larger than the quiescent volume. This "extra" volume must therefore be due to the presence of air bubbles.

Calculating a percentage gas holdup defined by:

$$\text{Gas Holdup} = \frac{\text{Actual Bath Volume} - \text{Quiescent Bath Volume}}{\text{Quiescent Bath Volume}} \times 100\% \qquad (3.6)$$

and plotting against injection air flowrate gives Figure 3.17. There is clearly a direct relationship between the gas fraction and the flowrate of the injected air. More importantly however, the gas fraction at the higher flowrates tested is as high at 14%. This has serious ramifications for the mathematical model discussed in the following chapter, since fluid properties such as viscosity and density will be altered significantly by this amount of gas. In addition, any calculations performed to model an industrial operation (such as zinc slag fuming) must take this effect into account.

Plotting gas holdup against modified Froude number in Figure 3.18 - for both the experimental results and data obtained on the slag fuming furnace - shows a very poor correlation. The gas fraction of the slag fuming furnace is much higher than any experimentally measured value, and yet the modified Froude Number of the furnace injection is lower than many experimental runs. Therefore, the gas fraction variation is not due to the inertial variation of the incoming air, and is not a bubbling-jetting phenomenon.

3.4.5. Bath Stirring

A quantitative indication that some type of flow transition occurs between the lowest and the highest air flowrates tested, is given by the bath kinetic energy (or stirring energy). The (experimental) mean cell kinetic energy can be calculated by:

$$\bar{E}_{cell} = \frac{1}{N} \sum_{i=1}^{n_i} \sum_{j=1}^{n_j} \frac{1}{2} (\rho \Delta x \Delta y z)(u_{ij}^2 + v_{ij}^2) \qquad (3.7)$$

where N is equal to the number of cells which contain velocity data. Cells for which it was not possible to collect velocity measurements (usually those near the surface) are excluded from this calculation. The effect this may have on the summation is discussed below.

Equation (3.7) has been applied to each set of velocity measurements. When plotted against air flowrate, one obtains the curve shown in Figure 3.19. This shows a steady increase in cell energy with air flow up to a maximum at an air flowrate of about 90 l/min and corresponding to a modified Froude number of 3. At this point, a sharp transition occurs, and the mean cell energy actually decreases with increasing blowing rate (this is most unexpected, as the injected air is the source of all kinetic energy in the bath). The mean cell energy continues to drop for all remaining air flowrates.

Unfortunately, the exclusion of cells lacking velocity measurements may have affected this summation somewhat, especially since the water velocities near the surface were the largest, and it was particularly difficult to obtain surface velocity measurements at higher air flowrates. This effect can be investigated by calculating the mean cell kinetic energy of non-surface cells and plotting this as a function of air flowrate, as shown in Figure 3.20. This curve follows the same overall trend as Figure 3.19, indicating that this observed transition is not due to a lack of surface velocity measurements.

As all other important factors such as depth of fill, tuyere diameter and vessel dimensions were constant throughout each run, it can only be concluded that this effect is due to a change in the mechanism of air-water energy transfer with air flowrate. The interaction of the incoming air with the water must have undergone a sharp change at an air blowing rate of about 90 l/min, otherwise the cell kinetic energy would continue to increase with increasing air flowrate.

A plot of the mean cell energy as a function of air input energy (Figure 3.21) illustrates this further. The energy input rate is defined as being the sum of the air buoyant and kinetic energy:

$$\dot{E}_{input} = \dot{E}_{buoyant} + \dot{E}_{kinetic} \tag{3.8}$$

$$= 2\ (\rho_w - \rho_g)Qh + 1/2\ \rho_g\ Q(Q/A)^2 \tag{3.9}$$

Figure 3.21 shows that, after a certain point, increasing the energy input rate actually causes a decrease in the kinetic energy possessed by the bath. Obviously therefore, the mechanism of energy transfer changes with air flowrate.

To characterize this transition, a series of photographs were taken of the air bubbles in the tank (Figures 3.22 to 3.24). Figure 3.22 shows bubble formation at a relatively low air flow of 38 l/min $N_{Fr'}$ = 0.4, corresponding to the velocity regime of Figure 3.7. It can be seen that the air enters as distinct bubbles that do not interact to any significant degree. The photograph taken at the transition air flowrate of 90 l/min

$N_{Fr'}$ = 2.3) shows that the bubbles tend to interfere with one another, or coalesce. Finally, at an air flowrate of 256.8 l/min (corresponding to the plot of Figure 3.16) Figure 3.24 shows the bubbles coalescing continuously, and the air "channels" its way to the surface.

It is this coalescence or channeling that is probably responsible for the reduced efficiency of energy transfer. The maximum amount of fluid entrained by a bubbled gas seems to occur when the bubbles do not interfere with one another. If the gas "channels" to the surface in the form of a continuous column of air, very little fluid is entrained. In such a case, the surrounding fluid is unable to penetrate the gas column, and much of the gas rushes to the surface without encountering any liquid at all, and little energy transfer can occur.

The transition between Figures 3.7 and 3.16, and the shape of Figure 3.21 can then be explained by the following hypothesis:

1. For air flows of less than about 90 l/min ($N_{Fr'}$ = 2.3) the air enters the bath in the form of discrete, non-interacting bubbles, which entrain liquid well. Increasing air flowrate merely increases energy transfer. This corresponds to the increasing section of the curve in Figure 3.21 and the profiles of Figure 3.7 to 3.10.
2. At an air flowrate of about 90 l/min (the maximum of Figure 3.19 and corresponding to a modified Froude Number of 2.3) the bubbles start to interact significantly both longitudinally, and with bubbles rising from adjacent tuyeres.

3. Air flowrates greater than this cause greater coalescence, and increasingly poor gas-liquid contacting. The fluid finds it more and more difficult to penetrate the gas column. This corresponds to the decreasing section of Figure 3.19, and covers Figures 3.11 to 3.14.
4. At an air flowrate of 157.8 l/min (the minimum of Figure 3.7 and corresponding to a modified Froude number of 12) complete channelling occurs. This drastically different gas-liquid contacting mechanism is responsible for producing the velocity field of Figures 3.15 and 3.16.

Channeling behaviour has been observed previously by several previous studies (37,14). Haida and Brimacombe (37) observed the onset of channeling to occur at a modified Froude number of 23, quite different from the value of 2.3 determined by this study. However, much of the channeling behaviour in this study is due to the interaction of bubbles originating from adjacent tuyeres, and not to the coalescence of bubbles rising from a single tuyere, as defined by Haida and Brimacombe. Therefore, it is reasonable that this interaction would occur at lower injection rates in this experimental system. This interaction of bubbles rising from adjacent tuyeres has also been shown to be significant in the nickel matte converting process (17), at Froude numbers as low as 12.

Unfortunately, the presence of this significant change in the gas-liquid interaction in this system invalidates the application of algebraic models of bath recirculatory motion based upon simple energy balances (33,34) since an increasing amount of input buoyant energy is not

transferred to the bath, but escapes the system entirely. It is this "lost" energy that is not accounted for in simply equating the kinetic energy of the bath with the energy of the input air. Any predictions for the velocity fields in multi-tuyere industrial systems at similar modified Froude numbers must take this coalescence effect into account if accurate calculations are to be made.

4. THE MATHEMATICAL MODEL

The objectives of the mathematical model written for this work were twofold:

1) To provide a means of analyzing the experimental velocity and surface shape measurements.
2) To provide predictions for the fluid flow regimes in the industrial processes of lead slag fuming and copper matte converting.

The overall similarity between the experiments and the industrial processes allowed the same computer model to predict values for both of these cases with little modification. Thus the experimental data serves both to verify the mathematical model, and to provide an accurate and detailed description of the gas-liquid stirring mechanism common to each of these systems.

The formulation of the mathematical model developed in this work proceeded in four distinct stages:

1) The general statement of the problem, where the governing equations and boundary conditions were identified. Within this general description, assumptions and approximations had to be introduced, to allow solution.
2) A numerical technique was chosen to solve the simplified system.
3) A computer progam employing this technique was run for many different sets of input conditions in an attempt to model the experimental data collected previously.

4) Finally, calculations were made to describe the fluid flow pattern in a Zinc Slag Fuming Furnace, and a Peirce-Smith Copper Converter.

4.1. General Statement of Problem

4.1.1. Governing Equations

The general principles that allow calculation of the motion of an isothermal fluid are the laws of conservation of mass and conservation of momentum. These laws are stated mathematically by the three dimensional Navier-Stokes equations:

$$\frac{\partial(\rho u)}{\partial t} + \frac{\partial}{\partial x}(\rho u^2) + \frac{\partial}{\partial y}(\rho uv) + \frac{\partial}{\partial z}(\rho uw) = -\rho g \frac{\partial h}{\partial x} - \left(\frac{\partial \tau_{xx}}{\partial x} + \frac{\partial \tau_{yx}}{\partial y} + \frac{\partial \tau_{zx}}{\partial z}\right) \tag{4.1}$$

$$\frac{\partial(\rho v)}{\partial t} + \frac{\partial}{\partial x}(\rho uv) + \frac{\partial}{\partial y}(\rho v^2) + \frac{\partial}{\partial z}(\rho vw) = -\rho g \frac{\partial h}{\partial y} - \left(\frac{\partial \tau_{yx}}{\partial x} + \frac{\partial \tau_{yy}}{\partial y} + \frac{\partial \tau_{zy}}{\partial z}\right) \tag{4.2}$$

$$\frac{\partial(\rho w)}{\partial t} + \frac{\partial(\rho uw)}{\partial x} + \frac{\partial(\rho vw)}{\partial y} + \frac{\partial(\rho w^2)}{\partial z} = -\rho g \frac{\partial h}{\partial z} - \left(\frac{\partial \tau_{zx}}{\partial x} + \frac{\partial \tau_{zy}}{\partial y} + \frac{\partial \tau_{zz}}{\partial z}\right) \tag{4.3}$$

$$\frac{\partial \rho}{\partial t} + \frac{\partial(\rho u)}{\partial x} + \frac{\partial(\rho v)}{\partial y} + \frac{\partial(\rho z)}{\partial z} = 0 \tag{4.4}$$

Here, Equations (4.1) to (4.3) represent the conservation of x,y and z fluid momentum, while Equation (4.4) states the law of conservation of mass: and is termed the "continuity equation". When supplied with the correct initial

and boundary conditions, these equations can be used to calculate the flow of a fluid under any conditions.

To achieve a solution to these equations for the experimental system discussed in Section 3, the following approximations were made:

1) The flow of the liquid in the tank was assumed to be perfectly two-dimensional. The laser-doppler measurements indicate that this is a fair assumption, and it greatly simplified further calculations.
2) The turbulent action of the experimental bath was described by time-averaging these equations, and employing the technique of a turbulent viscosity to describe the viscous and turbulent shear stresses. This assumption introduced little error by itself, and was necessary in order to calculate the turbulent flow field. The actual determination of this turbulent viscosity however introduced considerable approximation.
3) One phase only (liquid) was considered: the domain of calculation was assumed to end at the gas-liquid interface. Thus all subsequent calculations were only concerned with the flow of the water in the tank. This approximation also allowed constant fluid density to be assumed. This is a very important assumption. It greatly reduces the mathematical effort necessary to solve the problem, but consequently complicates the boundary conditions, and limits the applicability of the model. Unfortunately, there was very little choice in this matter as the complexity of a two-phase model was beyond the scope of this investigation. The adequacy of a one phase model in describing the experimental results is discussed in Section 5.

4) Convective stirring effects due to temperature gradients were neglected. This is a good assumption for the experiments performed in this work (which were essentially isothermal). For the case of the two industrial processes, Salcudean et al. (39) have shown that the magnitude of the Archimedes Number (Gr/Re) is of significance when determining the significance of the stirring due to temperature gradients. For the case of slag fuming and copper matte converting, the Archimedes number is very hard to estimate accurately, due to the lack of adequate information on temperature gradients, and therefore the effect of this assumption is difficult to quantify.

The actual equations employed by the mathematical model are therefore:

$$\frac{\partial u}{\partial t} + \frac{\partial u^2}{\partial x} + \frac{\partial (uv)}{\partial y} = -\frac{1}{\rho}\frac{\partial p}{\partial x} + \nu_t\left(\frac{\partial^2 u}{\partial x^2} + \frac{\partial^2 u}{\partial y^2}\right) + g_x \qquad (4.5)$$

$$\frac{\partial v}{\partial t} + \frac{\partial (uv)}{\partial x} + \frac{\partial v^2}{\partial y} = -\frac{1}{\rho}\frac{\partial p}{\partial y} + \nu_t\left(\frac{\partial^2 v}{\partial x^2} + \frac{\partial^2 v}{\partial y^2}\right) + g_y \qquad (4.6)$$

$$\frac{\partial u}{\partial x} + \frac{\partial v}{\partial y} = 0 \qquad (4.7)$$

This is the conservative form of the time-averaged two dimensional turbulent Navier-Stokes equations, written for an incompressible, isothermal fluid. The term ν_t is an effective turbulent viscosity, defined according to the Boussinesq approximation.

4.1.2. Boundary Conditions

A schematic description of the boundary conditions necessary to quantify the experimental results is shown in Figure 4.1. The (two-

dimensional, single-phase) liquid of the experiments is assumed to be bounded by the following:

1) The walls of the plexiglass tank.

2) The surface of the liquid.

3) The bubble column.

Each of these three conditions must be characterized mathematically if a quantitative description of the fluid flow within the experimental tank is to be achieved. This is by no means a trivial exercise: two of the three boundary conditions are extremely difficult to describe within the confines of this single-phase model.

For example, were a two phase model employed, the bubble column would simply be described as a constant inflow of gas, and the free surface as a gas-liquid interface. But the one-phase model requires that the horizontal and vertical velocity components and the liquid pressure be specified along the entire length of each boundary. In the case of the bubble column, this is almost impossible to achieve, while deriving these values for the free surface requires considerable mathematical effort.

Fortunately, the drag of the walls on the liquid is relatively simple to characterize, as the fluid velocity in the region of the walls is zero.

4.2. Selection of Solution Algorithm

As is usually the case, the selection of the numerical method for this particular problem was heavily influenced by the boundary conditions of the problem. An algorithm was sought that could adequately describe the pertinent boundary conditions, while still maintaining accuracy and computational efficiency. In this case, the combination of awkward boundary conditions and the type of flow made the selection of the solution algorithm more difficult:

1) The rectangular shape of the experimental tank meant that finite difference schemes could be applied easily to this simple system. However, this makes the description of flow in more complex (eg. round) geometries more difficult. This was unfortunate, since a partial objective of this work was to calculate the fluid flow regime in a (round) copper converter. Finite element methods are frequently used instead to describe the flow in such a domain.
2) The free surface at the top of the bath greatly complicated matters. Finite element methods have only been applied very sparingly to problems containing a free surface boundary. The nature of the finite element method makes it very difficult for this technique to calculate the fluid velocity and position at a free surface. Some finite element calculations have been made for such cases (51,52), but these require considerable approximation and are generally computationally inefficient, especially when compared to equivalent finite-difference techniques. Further the flow in the experimental tank has been shown to be highly rotational:

$$\xi = \frac{\partial v}{\partial x} - \frac{\partial u}{\partial y} \neq 0 \qquad (4.8)$$

This invalidates such techniques as the method of free streamlines (53) to describe the position of the free surface, as this requires potential flow ($\xi = 0$).

The only truly satisfactory numerical method capable of describing the free surface is the Marker and Cell (MAC) technique (54). The MAC technique and its variants allow calculation of the position of the free surface, as well as the velocity and pressure fields in this region. Again, several factors prevent the immediate selection of this type of technique:

a) The MAC methods are generally only used for laminar flows, as they are relatively complex numerical techniques; the addition of turbulent viscosity calculations can cause these methods to be prohibitively expensive in computer time.

b) MAC methods are transient techniques - steady state can only be attained by solving the system at successively greater points in time and determining when these solutions cease to change appreciably. Since we are only interested in the steady state velocity values, this is a very inefficient method of calculation.

c) MAC methods are generally very computationally expensive. They frequently require manipulation of vast amounts of data, and also employ many thousands of iterations to solve the Navier-Stokes equations. Even relatively "small" MAC programs often comprise several thousand executable statements.

There are large numbers of numerical methods that are capable of directly calculating a steady state velocity regime under turbulent conditions. However few, if any, of these can describe the position of a free surface adequately, since most of these rely upon the derived values of vorticity and stream function. (Vorticity and stream function simplify solution of the turbulent Navier-Stokes equations, but are of little use in the location of a free surface, as this relies upon the continuity equation, which vanishes). Because the motion of the free surface was considered to be of significance in determining the overall velocity field, these two functions could not be employed - solution had to be made in terms of the primitive variables (velocities and pressure).

Therefore, the ideal numerical technique for this problem would possess the following characteristics:

1) Capable of describing the free surface, as in the MAC methods.
2) Able to deal with turbulence adequately.
3) Direct calculations of the steady state velocity regime.
4) Capable of dealing with non-rectangular domains of calculation.

Unfortunately an efficient numerical method with all of these capabilities does not exist. Because of its ability to describe the free surface, a MAC method was selected and modified in an attempt to meet the other criteria:

1) Turbulence was to be modelled by employing a constant turbulent viscosity, calculated by the algebraic technique proposed by Sahai and Guthrie (44) and employed by Salcudean et al. (48).
2) Circular domains were to be dealt with by employing the techniques by Viecelli (55,56).
3) Two attempts were made to improve the transient nature of the MAC methods calculations of steady state.

a) Direct Steady-State Calculation:

A means was sought whereby the steady state velocities and surface profile could be calculated directly by a MAC type method. The MAC equations that describe the free surface were modified to apply to steady flow situation, and the steady Navier-Stokes equations were employed.

A program was written based on this method:

- the initial conditions were set into the velocity and pressure arrays.
- the steady Navier-Stokes equations were solved to produce new values for velocity and pressure.
- the surface was moved in accordance with these new values.
- iteration proceeded until a steady state was attained.

Unfortunately, despite all attempts, this program failed to converge. Eventually, it was determined that this failure to converge was due to the movement of the free surface. In effect, every time that the

surface was moved, a new computational problem was created. Since the surface was moved with each iteration, convergence was impossible. When the surface movement was deleted, this program rapidly converged.

b) Accelerated Steady State Solution

When the previous attempt failed, it was decided to revert to the MAC technique to advancing the free surface along discrete time steps. However, an attempt was made to predict the steady state solution from a very few transient solutions. A second computer program was written, this time employing the transient Navier Stokes equations. The program was run (with boundary conditions approximating those of the experimental apparatus) and allowed to calculate the velocity profiles and surface shape at several different time increments. These calculated values were still very different for those at steady state. The manner in which the calculated velocity in each finite difference cell changed with time was then used in an attempt to predict the steady state. This predicted steady state was then compared with the "true" calculated value.

Unfortunately, this attempt was also unsuccessful. The reason for this is revealed by a time plot of the calculated velocities of a finite difference cell (Figure 4.2). The oscillatory nature of the convergence is immediately obvious: the velocity values swing quite unpredictably at each time step, though they do approach a steady state. Again, this oscillation of the velocities is due to the unstable influence of the free surface. Moving the free surface at the beginning of each time step introduces a

complete change in the geometry of the computational mesh, which affects the calculated velocity values somewhat.

When the free surface was not allowed to move, the program immediately predicted the expected velocity field for flow in a square cavity, from a very few time steps. The velocity values of this predicted steady state were within .1% of those calculated for the true steady state, but used less than 10% of the computer time.

After these unsuccessful attempts to reduce the cost of employing a MAC method, it was decided that the only other alternative was to employ an efficient MAC algorithm, and to use all available computational techniques to increase efficiency and reduce cost.

4.3. The SOLASMAC Algorithm

The computational algorithm selected for these calculations was based on the SOLASMAC method developed by Hill (57), which simplified and combined the SOLA progra proposed by Hirt (58) and the SMAC method of Amsden and Harlow (59). For the purposes of this study, the SOLASMAC method was altered slightly to yield the SSMCR (SOLASMAC - ROUND DOMAIN) program. As with SOLASMAC the SSMCR program method uses an explicit transient finite-difference scheme to solve the viscous incompressible Navier-Stokes equations. Calculations are performed in primitive variables, allowing the position of the free surface to be determined easily. To increase stability and accuracy, upwind differencing is used to a slight extent.

As in all finite difference schemes, the solution domain is divided into a number of small squares, or "cells". Figure 4.3 shows a sketch of the finite difference grid used to model the laser-doppler measurements. Boundary conditions (except for the free surface) are applied in the fictitious cells on the edges of the domain. The velocity and pressure values for a cell are considered to apply at the cell centre. The central finite difference schemes used to approximate the terms of Equations 4.5 to 4.8 are contained in Appendix 1. A flowchart of the computer program is shown in Figure 4.4. After the velocities and pressures have been loaded into the boundary cells, the fluid velocity within all other cells is set to zero, and the pressure distribution is set to hydrostatic. This represents the initial condition of the experimental tank, before the air has been introduced.

Horizontal and vertical momentum equations are then solved explicitly for each non-boundary cell containing fluid. This procedure starts with the cell at the bottom left of the finite-difference mesh, and continues up the first column. Once the top of a column of cells is reached, the procedure starts again at the bottom of the next column, and continues bottom to top, left to right.

The solution of the momentum equations yields an estimate of liquid velocities for the next time step. The continuity equation is then applied to each cell:

$$div_{ij} = \frac{u_{ij} - u_{i-1,j}}{\Delta x} + \frac{v_{ij} - v_{i,j-1}}{\Delta y} \qquad (4.9)$$

The value of this sum is termed the "divergence" and is used to adjust the pressure and velocity fields using the following scheme:

$$\Delta p_{ij} = \lambda \rho \, div_{ij} \tag{4.10}$$

$$p_{ij} = p_{ij} + \Delta p_{ij} \tag{4.11}$$

$$u_{ij} = u_{ij} + \frac{\Delta t \, \Delta p_{ij}}{\rho \Delta x} \tag{4.12}$$

$$u_{i-1,j} = u_{i-1,j} - \frac{\Delta t \, \Delta p_{ij}}{\rho \Delta x} \tag{4.13}$$

$$v_{ij} = v_{ij} + \frac{\Delta t \, \Delta p_{ij}}{\rho \Delta y} \tag{4.14}$$

$$v_{ij-1} = v_{ij-1} - \frac{\Delta t \, \Delta p_{ij}}{\rho \Delta y} \tag{4.15}$$

where λ is an input parameter to the program, usually set by

$$\lambda = \frac{1.0}{2 \Delta t \left(\frac{1}{\Delta x^2} + \frac{1}{\Delta y^2} \right)} \tag{4.16}$$

Two constraints are placed on the time step, Δt:

$$\Delta t < \text{minimum} \left(\frac{\Delta x}{u}, \frac{\Delta y}{v} \right) \tag{4.17}$$

$$\Delta t < \frac{\rho}{2\mu} \frac{\Delta x^2 \Delta y^2}{(\Delta x^2 + \Delta y^2)} \tag{4.18}$$

This is carried out until the divergence of each cell falls below a specified error limit. When this occurs, these new cell velocities are used to calculate the new position of the free surface, and the entire procedure is repeated for the next time step. This method of solving the transient Navier-Stokes equations is very similar to many other numerical techniques.

However, the SOLASAMC method as used by SSMCR differs greatly by its treatment of the boundary conditions, most notably the free surface.

4.4. Treatment of Boundary Conditions

4.4.1. Locating and Moving the Free Surface

There are two main difficulties associated with calculations involving a free surface boundary: locating its position, and specifying the velocities and pressures at the surface.

Of the two, the former is simpler. Using mass balances, it is relatively straightforward to locate the position of the surface within the finite difference mesh, and to move it if appropriate.

Previous MAC methods (54,60) used marker particles to locate the surface position. These were fictious particles of neutral buoyancy that were considered to move with the flow of the liquid. At the end of a time iteration, the positions of the marker particles located the position of the free surface. However, to keep track of these particles required considerable amounts of computer time and memory. The SOLASMAC method, following the suggestions of Hirt, eliminates the need of these particles altogether. Instead the surface is located by a vector describing the height of the surface above an arbitrary datum at any position within the finite difference mesh (Figure 4.5). These "heights" are then moved according to a mass balance. The complete derivation has been performed by Hill, but a shorter description is given below.

Considering an element of the free surface:

Mass input rate:

$$= u(h_2 - h_1) + v\Delta x \tag{4.17}$$

Mass output rate:

$$= (u + \frac{\partial u}{\partial x}\Delta x)(h_2 + \frac{\partial h_2}{\partial x}\Delta x - h_1) + [v + \frac{\partial v}{\partial y}(h_2 + \frac{\partial h_2}{\partial x}\frac{\Delta x}{2} - h_1)]\Delta x \tag{4.18}$$

Rate of Accumulation:

$$\frac{\partial}{\partial t}[(h_2 - h_1)\Delta x + \frac{\partial h_2}{\partial x}\frac{\Delta x^2}{2}] \tag{4.19}$$

Applying the continuity equation, letting $\Delta x \to 0$, and observing $\frac{\partial h_1}{\partial t} = v$ one obtains (in finite difference form):

$$h_i^{t+\Delta t} = h_i^t + \Delta t\,(v_{ij} - u_{ij}(\frac{h_{i+1}^t - h_i^t}{\Delta x})) \tag{4.20}$$

Equation (4.20) is then used to advance the position of the free surface. In practice, the x and y fluid velocity components employed in Equation (4.20) are averages of surface cell velocities and those in adjacent cells. It has been found by Hill and others, that this increases stability and accuracy. The actual averaging scheme used depends upon the position of the surface in relation to the finite difference mesh. For example, if the free surface

(from the previous time step) lay below the centre of the surface cell, the averaged velocities would be:

$$\bar{u} = \frac{(1-f)}{4}(u_{i-2,j} + u_{ij} + 2u_{i-1,j}) + \frac{f}{4}(u_{i,j-1} + 2u_{i-1,j-1}) \quad (4.21)$$

$$\bar{v} = \frac{(1-f)}{4}(v_{i-1,j} + v_{i-1,j-1} + v_{ij} + v_{i,j-1}) + \frac{f}{4}(v_{i-1,j-1} + v_{i-1,j-2} + v_{i,j-1} + v_{i,j-2}) \quad (4.22)$$

where $$f = \frac{(j - 1.5)\Delta y - h_i}{\Delta y} \quad (4.23)$$

Additional velocity averaging methods are used if the surface is above the cell centre, or if there is a boundary cell nearby. These averaging schemes are largely a result of trial and error investigation by many different researchers. They are completely empirical, but have been shown to yield accurate results.

4.4.2. Free Surface Velocities and Pressures

Unlike locating and moving the free surface, specifying the values of the surface cell velocities and pressures is truly complex, since these values depend inherently on surface orientation. The equations that describe these values arise from the vanishing of the normal and tangential stresses on the fluid at the free surface. The normal stress condition is usually employed to estimate the pressure of a surface cell, while the tangential stress is used with the continuity equation to determine the vertical and

horizontal fluid velocity components. Again, the full derivation has been performed by Hill, and only an abridged version is given below. The only significant departure from Hill's derivation is the use of time averaged velocities to describe turbulence.

For a two-dimensional Newtonian fluid under laminar flow conditions, the velocity gradient descriptions of the normal and tangential stresses at a surface are:

Normal Stresses:

$$\tau_{xy} = p_{\ell} - 2\mu \left(\frac{\partial u_{\ell}}{\partial x}\right) \tag{4.24}$$

$$\tau_{yy} = p_{\ell} - 2\mu \left(\frac{\partial v_{\ell}}{\partial y}\right) \tag{4.25}$$

Tangential Stresses:

$$\tau_{xy} = \tau_{yx} = \mu \left(\frac{\partial u_{\ell}}{\partial y} + \frac{\partial v_{\ell}}{\partial x}\right) \tag{4.26}$$

If the flow of the fluid is turbulent, the x and y velocities and the isentropic pressure can be represented as being the sum of an average component and a fluctuating component:

$$u_t = u + u' \tag{4.27}$$

$$v_t = v + v' \tag{4.28}$$

$$p_t = p + p' \tag{4.29}$$

Substituting these values into the normal and tangential stress conditions and time-averaging, one obtains:

Tangential Stresses:

$$\tau_{xx} = p - 2\mu \left(\frac{\partial u}{\partial x}\right) \qquad (4.30)$$
$$\tau_{yy} = p - 2\mu \left(\frac{\partial v}{\partial y}\right)$$

Normal Stresses:

$$\tau_{xy} = -\mu \left(\frac{\partial u}{\partial x} + \frac{\partial v}{\partial y}\right) \qquad (4.31)$$

Note that the laminar viscosity, rather than the apparent turbulent viscosity, is used in the turbulent stress conditions. Therefore, the derivation of the normal and tangential stress conditions for a turbulent fluid surface proceeds similarly to that for a laminar surface, if time-averaged values are used.

Hill has shown that for a fluid surface inclined at an angle θ to the horizontal, a two-dimensional force balance on a unit length of surfaces gives:

Tangential Stress Condition:

$$-2 \tan \theta \left(\frac{\partial u}{\partial x} - \frac{\partial v}{\partial y}\right) + (\tan^2 \theta - 1)\left(\frac{\partial u}{\partial y} + \frac{\partial v}{\partial x}\right) = 0 \qquad (4.32)$$

Normal Stress Condition:

$$p = \mu \frac{(1 + \tan^2 \theta)}{2 \tan \theta} \left(\frac{\partial u}{\partial y} + \frac{\partial v}{\partial x}\right) \qquad (4.33)$$

Since the sum of the forces on a fluid surface are zero.

Thus to describe the fluid velocity and pressure at the surface, one is forced to satisfy a further two partial differential equations, whose form depends upon surface orientation. Fortunately, approximations can be made.

4.4.2.1. Normal Stress Condition

The SOLASMAC method employs the full normal stress condition to specify the pressure in the finite difference cells at the fluid surface. However, SOLASMAC was written to study flows at Reynolds numbers, where the viscous pressure correction term in the normal stress equation becomes significant. Hirt and Shannon (60) have shown that the full normal stress condition need only be used at Reynolds numbers below 10.

Therefore, the pressure of the surface cells was considered to be atmospheric. This approximation is common in MAC-type codes (it was used in the original MAC program) as it reduces complexity and increases stability at little cost in accuracy.

4.4.2.2. Tangential Stress Condition

The surface velocities set by the tangential stress condition also depend upon surface inclination. The SOLASMAC method considers surface orientation in 15 degree increments. That is, for surfaces oriented between the horizontal and +15 degrees, one equation is used. For those inclined between +16 and +30 degrees, a different equation is employed and this continues in 15 degree increments.

Hill chose to be this accurate because he was solving problems at low velocities, where differences of a few millimeters per second were significant. This type of accuracy is not justified for the purposes of this investigation.

Therefore, in the SSMCR program, the tangential stress condition was approximated much more roughly. As in the original MAC program, surface slopes are considered to be either horizontal, vertical or at 45 degrees. Figure 4.6 shows how these slopes are recognized by the computer program: the three cells surrounding a surface cell (the central cell in Figure 4.6) are examined. If only one is empty of fluid, the surface is either horizontal or vertical. If two are empty, the surface is at 45 degrees. For a surface cell that contains a section of surface considered to be horizontal, the horizontal velocity component is calculated by the x-wise momentum equation, while the vertical component is defined by the continuity equation:

$$v_{ij} = v_{i,j-1} + \frac{\Delta y}{\Delta x}(u_{ij} - u_{i-1,j}) \tag{4.24}$$

The horizontal tangential stress condition is applied by adjusting the horizontal velocity in cells outside the free surface:

$$u_{i,j+1} = u_{ij} - \frac{\Delta y}{\Delta x}(v_{ij} - v_{i-1,j}) \tag{4.25}$$

This velocity is then used to solve the x-wise momentum equation at the next time step.

Vertical cells are treated similarly. Cells located on a 45 degree surface have their velocities specified by setting:

$$u_{ij} = u_{i-1,j} \tag{4.26}$$

$$v_{ij} = v_{i,j-1} \tag{4.27}$$

Thus simultaneously satisfying both the tangential stress condition and the continuity equation.

4.4.3. Rectangular Wall Boundaries

The boundary conditions used to describe the influence of the walls of the experimental tank were, in comparison to the others, extremely simple to apply. As stated earlier, these conditions were applied in the fictitious cells surrounding the computing region. In these regions, the velocity component perpendicular to the wall was set to be zero. The velocity component tangential to the wall was either zero (no slip) or unaffected by the wall (free-slip), as seen in Table 4.1.

The choice between the no slip and free slip conditions is made depending on the relative sizes of the boundary layer and the finite-difference mesh. For low Reynolds number flows, where the boundary layer is large compared to the cell size, the no-slip approximation should be used. At higher Reynolds numbers, the boundary layer is small, and the retarding effect of the wall is limited to a region smaller than a finite difference cell. For this case, free-slip should be used. In actual fact, the choice of these boundary conditions had little effect on the calculations. Both types of approximation were tested, and similar results were obtained with each.

4.4.4. Curvilinear Boundary

To predict the flow regime in a copper converter, it is necessary that the mathematical model be capable of dealing with a curved or non-rectangular boundary. Initially, the technique of Viecelli was employed, whereby the pressure of boundary cells was adjusted to constrain the fluid to flow parallel to an arbitrary boundary.

However, this pressure adjustment was found to be insufficient: the fluid was not significantly affected by the pressure in the boundary cells to cause it to flow parallel to a curved wall. This was due to the relatively small size of the terms $\frac{\partial p}{\partial x}$ and $\frac{\partial p}{\partial y}$ in the momentum equations, compared to such viscosity-dependent terms as $\frac{\partial^2 v}{\partial y^2}$ or $\frac{\partial^2 u}{\partial x^2}$ - since the effective viscosity used in this study was many orders of magnitude higher than the laminar viscosity employed by Viecelli. To force the velocities near the wall to flow tangentially, it was therefore necessary to adjust the boundary value velocities, not the pressures. The following technique was then employed:

1) The curvilinear boundary was imposed over a finite difference grid. Cells that intersected the bottom boundary were termed boundary cells.
2) For each time step, the fluid in these boundary cells was constrained to flow tangetially to the wall. There was no velocity component normal to the wall. The magnitude of the tangential velocity was calculated from the net mass flow into the cell (i.e. by the continuity equation).

3) The pressure in these boundary cells was adjusted in accordance with a Bernoulli-type equation: the pressure change being calculated by the change in fluid momentum.

The intersection of a surface cell and a wall cell was treated by setting the pressure of the cell equal to zero, and determining the velocities by the continuity equation. When this (admittedly crude) boundary approximation were employed, the fluid was found to flow tangentially to the round wall.

4.4.5. Gas-Liquid Boundary

The final boundary condition requiring treatment is the gas liquid interface - the bubble column. This is by far the hardest to characterize mathematically due to its inherent complexity and the lack of experimental data. The injection of a gas into a quiescent bath causes the liquid to rise by a number of inter-related effects.

The first of these is fluid displacement or entrainment. A rising gas bubble pushes and shears liquid as it moves upward, causing the fluid to rise. Sahai and Guthrie (33) have argued that this effect occurs with the action of large, stable, gas bubbles.

Another mechanism for liquid movement is buoyancy. The presence of a bubble lowers the density in its vicinity. This density difference causes the fluid beneath the bubble to rise, following the bubble to the surface.

Despite these general guidelines, and the existence of some experimental data, the mathematical description of the gas-liquid interface is by no means complete. For example, simple models such as that proposed by Sahai and Guthrie (34) make no mention of the effect of bubble coalescence on the liquid rise velocity - a serious (though understandable) omission. Mathematical models based on these descriptions have had some qualitative success, but there remains considerable disparity between experiments and calculations. Therefore before reliable calculations can be made, an adequate description of this boundary is necessary, which requires the water velocity and pressure distribution along the length of the rising gas column as a function of injected gas flowrate. Unfortunately, this data is not yet available.

Therefore, all descriptions of the gas-liquid boundary condition used by the mathematical model in this work will be, at best, semi-empirical. Various theoretical velocity and pressure distributions will be applied to the model, and the results studied. Those predicting velocity and surface values that conform closest to the experimental data will be accepted as valid descriptions. That is, the mathematical description of the gas-liquid boundary condition will be inferred by the agreement of calculations with experiments.

5. CALCULATIONS - COMPARISON WITH EXPERIMENTAL RESULTS

Before calculations of flow regimes were performed, the computer program used in this study was subjected to several tests to ensure that it was error-free. Foremost among these was the calculation of flow in a square cavity: the SSMCR program was set the task of computing the flow regime of a fictious fluid (having a viscosity of 0.4 g/cm s) in a square cavity measuring 1 cm x 1 cm (Figure 5.1). This problem is suitable for test conditions as it is relatively simple (involving no free-surface conditions or turbulence) and has been extensively studied (61-62). The output of the SSMCR program was compared to that published by Hill (57). This comparison is shown in Figure 5.2 and clearly there is excellent quantitative agreement between the two sets of data. Hill's program was, in turn, verified by comparison to an analytical solution.

Unfortunately, the velocity vector plots so commonly used to illustrate vortex flow patterns are of little use in quantitative comparisons of different velocity regimes. For example, during the development and "debugging" of the SSMCR program, an error was discovered in which the viscous drag term of the Navier-Stokes equations was incorrectly described. This had a considerable effect on the magnitude of the calculated velocities, but as Figures 5.3 and 5.4 show, the vector plots of the velocities calculated by the erroneous (Figure 5.3) and correct (Figure 5.4) conditions are very similar. In fact, it was not until actual numerical values were examined that this error was discovered. Therefore, these plots by themselves are not suitable for comparison between experimental and

calculated values, since a considerable disparity between velocity patterns could pass undetected.

In an attempt to quantify the comparison between the model results and the experiments, two values were defined: the mean cell angular deviation, and the mean cell magnitude deviation. These are calculated as follows:

$$\bar{D}_{\theta} = \frac{1}{n_i n_j} \sum_{i=1}^{n_i} \sum_{j=1}^{n_j} \tan^{-1}\left(\frac{u_{ij,e}}{v_{ij,e}}\right) - \tan^{-1}\left(\frac{u_{ij,c}}{v_{ij,c}}\right) \qquad (5.1)$$

$$\bar{D}_{mag} = \frac{1}{n_i n_j} \sum_{i=1}^{n_i} \sum_{i=1}^{n_j} \frac{\sqrt{u_{ij}^2,_e + v_{ij}^2,_e} - \sqrt{u_{ij}^2,_c + v_{ij}^2,_c}}{\sqrt{u_{ij}^2,_e + v_{ij}^2,_e}} \qquad (5.2)$$

The angular deviation gives an indication of how well the shapes of the computed and measured vortices agree, by comparing the orientation of the velocity vectors. The magnitude deviation indicates how well the predicted velocity distribution agrees with the experimental measurements. However, a non-zero magnitude deviation can indicate two possibilities:

1. The overall predicted bulk motion of the fluid is too high or low - that is, the left hand boundary condition used by the program is imparting too great or too small a velocity to the fluid. This would be the case in which the highest calculated velocities are located in the same region as the highest measured velocities, but the relative magnitudes of these values differ.

2. The overall distribution of the predicted velocity field is incorrect. This would be the case in which the highest predicted velocities are not located in the same region as the highest measured velocities.

To identify which of these effects is significant, an additional factor, the velocity distribution deviation defined by:

$$\bar{D}_{dist} = \frac{1}{n_i n_j} \sum_{i=1}^{n_i} \sum_{j=1}^{n_j}$$

$$\frac{(u_{ij}^2{}_{,e} + v_{ij}^2{}_{,e})^{1/2} - \left[\left(\frac{u_{ij,c}\, V_{max,e}}{V_{max,c}}\right)^2 + \left(\frac{v_{ij,c}\, V_{max,e}}{V_{max,c}}\right)^2\right]^{1/2}}{(u_{ij}^2{}_{,e} + v_{ij}^2{}_{,e})^{1/2}} \qquad (5.3)$$

is calculated. If this value is low relative to the magnitude deviation, it can be concluded that the first of these effects is predominant, and the predicted fluid velocity distribution is essentially correct, but the bulk of the fluid is moving too slowly or too fast. If the velocity distribution deviation is high relative to the magnitude deviation, the second effect is predominant, and the general velocity distribution is incorrect.

This relatively complex method of comparison between the predicted and measured velocity distributions allows precise, quantitative, conclusions to be drawn as to the success or failure of both the model as a whole and its various boundary approximations. This in turn allows the model to be "tuned" or fitted to the experimental data. When considered along with the vector plots, the three deviation values give a good indication of the accuracy of a given flow calculation.

Once the program had been verified in the manner mentioned previously, calculations were performed in attempts to compute the experimental flow patterns. A variety of approximations (shown below) were used for the gas-liquid boundary. As well, the value for the turbulent viscosity used by the model was varied from run to run in an attempt to obtain good agreement with the experiments. The algebraic effective viscosity model of Sahai and Guthrie (44) was tested, as were completely empirical viscosity values. The effective viscosity values predicted by the model of Sahai and Guthrie (44) are shown in Table 5.1.

5.1. Constant Vertical Velocity

The first approximation to the two-phase region used by the mathematical model was that of constant upward velocity. That is, the bubbles in the experimental tank were considered to impart a constant upward velocity to the fluid in this region. This shearing of the liquid was then transmitted into the bulk of the fluid by viscous forces. This assumption was incorporated into the mathematical model by applying a constant vertical velocity to the cells in the left wall boundary region, and setting the horizontal velocity of these cells to be zero. The initial pressure distribution was assumed to be hydrostatic.

Calculations were performed by the program until steady state had been attained. The onset of steady state was arbitrarily determined to occur when the velocities of each cell changed by less than 5% over 20 time steps. An additional check on this condition was made by comparing a

"steady state" velocity profile with profiles calculated at several previous times, and ensuring that the difference was both small and diminishing with time.

The results of many of the calculations performed using this boundary condition are shown in Table 5.2. Many other calculations were performed besides those shown in Table 5.2, but these were generally of a preliminary nature, and served mainly to determine the optimum values of the two input parameters (viscosity and left wall velocity).

By examining Table 5.2, a number of inferences may be drawn:

1. It is possible to obtain very low values of both the mean cell velocity deviation and the velocity distribution deviation (< 10%) using this boundary condition.
2. Generally speaking, the three deviation values are relatively constant for all experiments. That is, the calculations performed at certain values of viscosity and velocity seem to apply equally well (or poorly) to all of the experimental measurements.
3. In all cases calculated with this boundary condition, the mean cell directional deviation is very high: between 30 and 60 degrees. However, this disagreement appears to be more pronounced with the experiments performed at lower air blowing rates.
4. Increasing the boundary velocity does not seem to lower the directional deviation at all. By increasing the boundary velocity it is possible to lower the mean cell velocity deviation to be only 10%, but the directional deviation remains high at 30 to 40 degrees.

5. The effect of increasing the viscosity also appears to be slight. Increasing the viscosity from about 10 g/(cm•s) to 40 g/(cm•s) and to 400 g/(cm s) lowers the mean cell velocity deviation but does not change the values of the directional deviation appreciably.

Observations 4 and 5 above indicate that the overall shape of the velocity profile is relatively independent of either the viscosity or the boundary velocity, and is instead determined mainly by the nature of this boundary condition itself.

This conclusion is supported by comparing Figures 5.5, 5.6 and 5.7 with the experimental plots of Chapter 3 (the velocity and viscosity values used to generate the calculated figures are shown on the plots themselves). It is obvious that the effect of increasing the viscosity (from 10 to 40 to 400 g/(cm•s)) is to increase the vertical velocity of the cells to the right of the boundary, and to transmit this increased velocity further into the fluid (this is reasonable, as viscosity is the main means of energy transfer from the boundary to the liquid). This is turn has two effects: firstly, the mean cell magnitude deviation is lowered due to the increased overall velocity of the flow. Secondly, the velocity distribution deviation is lowered, as the interior and surface cells increase in velocity with respect to the left wall cells (Figures 5.6 and 5.7); the bulk of the fluid motion is no longer completely confined to a small region in the left side of the computational regime (as in Figure 5.5). This is closer to the experimental plots of Figures 3.7 to 3.16, where the largest fluid velocities occur in the region of the surface, and not at the left side of the tank. The velocity

distribution deviation cannot be reduced to zero however, as the maximum calculated velocities still occur at the left wall.

However, the overall directions of the calculated velocity vectors do not change significantly from Figure 5.5 to 5.7: those near the left wall possess the highest velocities, and are largely vertical. The surface velocities remain generally low, and largely horizontal. Both of these predictions are strongly contradicted by the experimental vector plots.

Therefore, because of the inability of the mathematical model to agree with the direction of the experimental velocity vectors, one is forced to conclude that this description of the gas-liquid boundary is not accurate. Thus the stirring of the water in the experimental tank was not significantly due to the shearing action of the bubbles on the liquid; if it were, this boundary condition would have been able to fit the experimental data. An entirely different mechanism must therefore be responsible for stirring the liquid in the tank.

5.2. Variable Density

Apart from shear due to bubble rise velocity, another mechanism that may be significant in causing the experimental flow regimes is the lowering of the density of the liquid in the region of the bubbles. An hypothesis for such a mechanism is as follows:

1. The effect of the presence of a bubble in the liquid is to lower the density (and therefore the hydrostatic pressure) in the region of the bubble.
2. This low pressure region then causes an influx of the higher-density adjacent fluid.
3. As this bubble rises under the influence of buoyant and inertial forces, this low-density (and therefore low pressure) region moves upward with it.

This approximation has been used in a great many mathematical studies of gas injection into liquid ladles (31,40,42,43).

To apply this method to a mathematical model, the average density of finite difference cells in the left hand boundary is lowered by employing a void fraction:

$$\rho_{ij} = \alpha \rho_g + (1 - \alpha) \rho_f \qquad (5.4)$$

to simulate the presence of gas bubbles. The liquid in the boundary cells will rise due to the vertical pressure difference term in the Navier-Stokes equations. Modifications have to be made to the continuity equation to allow for this reduction of fluid density:

$$\frac{\rho_{ij} v_{ij} - \rho_{ij-1} v_{ij-1}}{\Delta y} + \frac{\rho_{ij} u_{ij} - \rho_{i-1,j} u_{i+j}}{\Delta x} = 0 \qquad (5.5)$$

Frequently, the shearing effect mentioned above is applied along with this approximation. In this case, a vertical velocity is applied to these boundary cells, along with a reduced density. Both methods were tested in this investigation.

To apply the variable-density method to the SSMCR program, it is necessary to obtain values for the void fraction in the bubble column. Unfortunately void fraction measurements of this type were not made directly. An estimate of this value can be derived from the bulk voidage measurements shown in Figure 3.19. Direct observation indicates that virtually all of the bubbles are confined to the region 6 cm from the left wall of the tank. Assuming that these bubbles alone are responsible for the increase in the overall tank volume, the bubble column gas holdup can be calculated as follows:

$$\alpha_{column} = \alpha_{bulk} \cdot \left(\frac{A_{tank}}{A_{column}}\right) \qquad (5.6)$$

The gas concentrations in the bubble column calculated by this means are shown in Table 5.3. These voidage values are at best only a crude estimate since they assume a constant gas concentration throughout the length of the two-phase region, while observations indicate that the gas concentration is higher at the free surface than in the bubble column.

Applying these values to the SSMCR program yields the velocity vector plots such as those shown in Figures 5.8 and 5.9. The values for the mean cell velocity, angle and distribution deviation are shown in Table 5.4

for the best run with this boundary condition.

It is immediately clear from Table 5.4 (and from the vector plots of Figures 5.8 and 5.9) that this boundary condition gives very different results from the constant velocity condition. For example, the comparison of run VK.4 with the experimental measurements shows that for all cases, the mean angular deviation is very low, with a maximum (absolute) value of -12.4 degrees and a minimum value of 0.40 degrees. This certainly very good agreement, and is far better than that attained by the previous condition.

However, the velocity deviations indicate that this boundary approximation is not perfect. For run VK.4, the mean velocity deviation is very high at 99.8% for all experiments. This indicates that the calculated velocities were only about 0.2% of the measured velocities which is extremely poor agreement. More important however, the velocity distribution deviation is quite high, at a value of 10 to 30%. An examination of Figure 5.8 explains this: the maximum velocities still occur at the left side of the tank and not at the surface as is shown by the experiments.

This indicates that the main effect of lowering the density in the boundary cells is to impart a vertical velocity to them, as in the previous boundary condition. However, this condition has been shown to be more accurate than the constant upward velocity condition. Therefore, this increased agreement with experiments (the lowering of the angular deviation) must be due to the effect of the $\frac{\partial p}{\partial x}$ term. This term was initially zero in the constant upward velocity condition, but was non-zero (and negative) in

this case. As shown by the x-wise momentum equation this term directly affects the x-wise velocity. Thus, the major effect of this term is to cause a negative horizontal velocity in cells adjacent to the gas boundary.

Imparting a positive vertical velocity to the boundary cells (along with the lowered density) results in velocity plots such as that shown in Figure 5.9. The deviation values shown in Table 5.4 indicate that the increased boundary velocity lowers the mean velocity deviation, but correspondingly increases the mean angular deviation. In effect, this case is a reversion to the constant upward velocity boundary condition. The effect of the $\frac{\partial p}{\partial x}$ term on shaping the flow is reduced by the greatly increased vertical boundary velocities.

From the results of the calculations made with this condition, it can be concluded that the reduced density boundary condition accurately predicts the overall shape of the experimental velocity profiles. This indicates that there is, in fact, a small net horizontal flow of fluid into the bubble column. Unfortunately, this method was unable to predict the magnitude or the distribution of the experimental velocities accurately. Thus it can be concluded that this approximation, by itself, it is not an accurate description of the bubble column.

5.3. Pulsed Boundary

The third attempt to characterize the bubble column mathematically involved "pulsing" the velocity in the boundary cells. The bubbles were

once more considered to give a vertical velocity to the surrounding liquid, but the effect of the bubbles was crudely simulated by the following mechanism:

1. Bubbles were considered to impart a constant upward velocity to boundary cells in which they reside.
2. Boundary cells were considered to contain a bubble, or be full of fluid. The size of a bubble was one boundary cell.
3. Bubbles were moved upward to the next cell at time intervals corresponding to their rise velocity. This was initially assumed to be 40 cm/s, based on the observations of Davenport (65), but was freely varied.
4. The bubble frequency was assumed to be 10 Hz. This was based on the observations of Hoefele and Brimacombe (7).
5. Bubbles that reached the surface of the bath were allowed to escape; new bubbles were introduced at the bottom of the bath.

Thus as the imaginary (two-dimensional) bubbles move through the left hand boundary cells, they impart a vertical velocity to these cells and shear the surrounding liquid. Once the "bubbles" leave the surface of the liquid, the fluid is allowed to fall under gravitational forces.

The values used for the bubble rise velocity and formation frequency were freely varied in an attempt to obtain good agreement with experimental data. These two parameters were found to have little influence on the overall results.

The best results of this approximation are shown in Figure 5.10. Qualitatively, this method appears to yield better results than the simpler constant velocity condition. The surface velocities are larger in comparison to the cells at the left side of the tank than those produced by the previous condition. This observation is supported by the relatively low values of the velocity distribution deviation generated by this boundary condition (Table 5.5). The collapse of the surface after the passage of a bubble is responsible for these higher surface velocities.

5.4. Collapsing Surface

The previous three boundary approximations have been shown to predict that the maximum fluid velocities would occur at the bubble-liquid interface, which differs from the experimental results. It is evident from Figures 3.7 to 3.16 (particularly 3.14 through 3.16) that the flow of fluid down from the free surface is of great importance in determining the experimental velocity regime, and therefore a means of incorporating this phenomenon into the computer model was sought.

The "collapsing surface" condition described below was an attempt at describing this effect. Using this condition, the free surface was set at an initial position and allowed to collapse under gravity, causing the fluid under it to move.

The collapsing surface approximation was applied to the SSMCR program in the following manner:

The surface of the fluid in the finite difference grid was assumed to have an initial, non-horizontal, orientation. Several different ways of determining this initial surface position were utilized:

1. Calculated surface profiles were tested (for example, that occurring in Figure 5.9 was used as an initial surface position to generate Figure 5.11).
2. Experimental surface measurements.
3. Arbitrary surface profiles were also used to see the effect of changing the surface shape.

The initial velocity of the fluid was set to be zero.

With these initial conditions, the computer program was run, and allowed to calculate the fluid velocity at subsequent time intervals. As calculation progressed, the fluid surface was allowed to collapse under gravity. The effect of bubbles was taken into account by raising the surface to its initial position at time intervals corresponding to an input bubble frequency (usually set to be 8-10 s^{-1}). Thus, at computational times corresponding to every 1/10th of a second, the surface collapse was stopped, and the free surface was set to its initial position. Calculation then proceeded from this new position, with the surface allowed to collapse as before.

Detection of the onset of steady-state was somewhat more complex with this boundary condition as compared to the previous four conditions.

This is because the fluid velocity changes continuously throughout the time that the surface is collapsing. Therefore, to detect steady-state, it was necessary to compare velocity profiles taken at identical time intervals in the surface movement cycle. For example, if the surface was reset every 0.1 seconds, and the system time step was 0.005 seconds, then two velocity profiles calculated at 0.110 s and 0.210 s could be compared; two profiles calculated at 0.110 s and 0.215 s should not be compared for this purpose however.

Figures 5.11 and 5.12 show steady-state velocity vector plots generated by this condition at two points in the surface collapse cycle. It is obvious that there is, in fact, little difference between these three plots. The initial surface shape used was that of Figure 5.9. The mean cell deviation values for calculations performed by this condition are shown in Table 5.6.

By examining Table 5.6, it is obvious that this boundary condition gives very low values for the mean cell angular deviation (a minimum value of 0.8 degrees and a maximum value of 12 degrees). In addition, this approximation also yields very low velocity distribution deviation values (8 to 15%). One can conclude by these facts that the computer model accurately predicts both the direction and the relative magnitudes of the experimental velocity vectors. This boundary approximation is even more successful than the reduced density method described in Section 5.2.

However, the mean cell magnitude deviations of the plots generated by this boundary condition are all very high, (greater than 99%), indicating that the predicted velocities are much lower than those occurring in the experimental tank. This is reasonable, as it is unlikely that the collapse of a surface only a few centimetres would be capable of producing water velocities as high as those found in the experiments.

In an attempt to increase the velocities predicted by this condition, a positive vertical velocity was applied to the left wall boundary cells. The results of this approxiation are also shown in Table 5.6, and it is clear that this attempt is only partially successful: the mean cell magnitude deviation values are lowered, but there is a corresponding increase in the directional and distribution deviations. This indicates that as the left wall velocity is increased, this boundary condition tends to the constant upward velocity condition, with a corresponding decrease in accuracy.

Therefore, it can be concluded that the collapsing surface condition accurately predicts both the orientation and the velocity distribution of the experimental flow patterns, though is unable to predict the absolute magnitude of the experimental velocities. This indicates that, if each velocity value predicted by this boundary condition were multiplied by the ratio of the maximum measured velocity to the maximum predicted velocity, one would obtain excellent agreement between the calculated results and the experiments.

5.5. Discussion

Based upon the results discussed above, it can be concluded that the stirring of the water in the experimental tank must be largely driven from the surface. The first three boundary approximations - all of which assumed that the flow was driven from the left boundary - were all unsuccessful in predicting the experimental velocity profiles. However, when a boundary condition was used in the mathematical model that assumed all of the liquid motion was due to the action of a collapsing surface, much better agreement with the experimental results was achieved, even though the magnitudes of the predicted velocities are too low.

It would not be correct to assume that the rather simplistic "collapsing surface" model is necessarily a true description of what is actually occurring in the experiments. Rather, this model indicates that the free surface is of paramount importance in determining the experimental velocity regimes. In fact, the bulk of the stirring in the tank appears to be driven from the surface, and not from the left side as has been assumed previously.

Figures 3.7 to 3.16 and the calculations discussed above allow an hypothesis of the stirring mechanism within the water tank to be proposed:

1. The effect of the bubble column is to cause the water in this region of the tank to rise, largely due to density differences.

2. The air-water column rises along the left side of the tank, but does not shear the adjacent fluid significantly.
3. At the surface, the trapped air escapes. The water then falls under the influence of gravity, but is displaced outward by more fluid rising from below.
4. This water then travels downward and outward across the free surface at high speed. It is this fluid which is largely responsible for the stirring of the liquid in the tank.

In this case, the "collapsing surface" condition would only be an approximation to the actual case - even though this approximation agrees with the experiments. It is proposed that the high experimental surface velocities are due to fluid being continuously introduced across the entire length of the surface, and not due to a "collapse" of the surface itself. Therefore, even though the collapsing surface boundary condition yields relatively accurate results, it would not necessarily be a physically accurate description of the experimental process of stirring.

A more physically correct boundary condition, might be to constantly introduce downward-directed fluid along the length of the mathematical free-surface, while maintaining a constant surface shape. Unfortunately, all attempts made to apply this type of condition failed due to computational instability.

Therefore, a completely accurate description of the bubble-liquid boundary appears only to be possible with a mathematical model capable of performing calculations on two phases (air and water) simultaneously. A single-phase model (such as SSMCR) is clearly limited in its ability to describe the intricacies of the gas-liquid boundary.

6. INDUSTRIAL CALCULATIONS

6.1. Fluid Flow in a Copper Converter

6.1.1. Assumptions

The dimensions and physical constants that were used to model the flow in a Peirce-Smith converter are presented in Table 6.1. This data was obtained mainly from Johnson (63), as well as from Bustos et al. (17) and Hoefele and Brimacombe (7).

A number of simplifying assumptions were made about the flow regime in this industrial vessel to allow calculation to proceed:

1. All of the flow is two dimensional and due only to the influence of bubbles. Temperature gradients have no effect.
2. The effect of slag on the surface of the copper matte was neglected.
3. The bath was assumed to be completely isothermal, and incompressible.
4. The reaction of air with the matte and the generation of sulphur dioxide was neglected.
5. Calculations were only performed on the bulk of the fluid. The bubble column itself, and all fluid between this region and the adjacent wall was neglected from calculations.

The value for the effective viscosity was determined from the calculations presented in the previous chapter: the viscosity values which were the most successful in predicting the experimental data (400 g/cm s) were

"scaled up" to apply to the industrial system. This was done be defining a new constant to apply to the effective viscosity model of Sahai and Guthrie (44).

The effective viscosity predicted by the model of Sahai and Guthrie is given by:

$$\mu_{eff} = K H\rho \left[\frac{(1-\alpha)gQ}{R}\right]^{1/3} \qquad (6.1)$$

where K is taken to be 5.5×10^{-3}.

Setting the effecting viscosity value of 400 g/cm s equal to the left hand side of Equation (6.1), a new value for K can be determined that applies to the side-blown, multi-tuyere systems of interest:

$$K = \frac{\mu_{eff}}{\rho H \left[\frac{(1-\alpha)gQ}{R}\right]^{1/3}} = 6.28 \qquad (6.2)$$

which is three orders of magnitude larger than that previously used.

Employing this new value of K to the copper converter yields an effective viscosity value of approximately 5000 g/cm s.

6.1.2. Mathematical Description of Gas-Liquid Interface

Based on the calculations presented in the previous chapter, it was concluded that the most accurate description of the bubble column in the

distribution of the velocities, are probably predicted accurately.

2. The highest fluid velocities are predicted to lie in the region of the free surface.
3. The kinetic energy of the fluid bath appears to be poorly distributed compared to that observed in the experimental tank: there are large regions of the copper converter that have very low fluid velocities relative to the surface. This may be due to two effects:

   a) The copper converter (when 35% full) is bounded by a much larger area of wall (40% larger) than does a square tank of equivalent volume. This indicates that the wall will retard the fluid to a much greater extent in the copper converter than in the experimental tank.
   b) The bubble column in the copper converter does not enter near the bottom of the vessel (as in the experimental tank). Instead, the air column enters through tuyeres that are elevated 0.5 m off the bottom of the converter (Figure 2.1). This has the effect of reducing the buoyant input power of the injected air relative to bottom-injection. As well, operating with the tuyeres close to the surface reduces the amount of fluid that is able to come in contact with the air column at any given time. The closer the tuyeres are placed to the surface, the shorter the length of the bubble column becomes, and therefore the volume available for stirring and reaction is reduced.

It is reasonable to conclude therefore that the stirring efficiency in the copper converter could be increased by the following factors:

a) If the converter were arranged as a vertical cylinder instead of a horizontal cylinder, the amount of wall that contacts the fluid would be reduced by as much as 40%. This would have the effect of reducing the wall drag effect, and increasing the circulation velocities.

b) Blowing from the bottom of the vessel, rather than from the sides would increase the buoyant input power to the bath, and consequently (in the absence of channelling) increase the recirculation velocity.

As has been discussed by Bustos et al. (17) an unstable gas envelope forms at the mouths of the tuyeres in the copper converter. Based on the experimental investigation in which this effect was observed, it can be concluded that the stirring efficiency in the Peirce-Smith converter is less than optimal when operating in this manner. An increased tuyere spacing or a reduction in air flowrate could conceivably increase this efficiency.

6.2. Fluid Flow in a Zinc Slag Fuming Furnace

The following set of predictions for the fluid flow regimes in a zinc slag-fuming involve significantly greater approximation than those made for the Peirce-Smith copper converter. This is for two reasons:

1. The liquid in the fuming furnace has an extremely high concentration of entrapped gases. Studies by Richards (9,10) indicate that the porosity of the furnace approaches 40%. Therefore, the single-phase SSMCR model is greatly limited in its ability to model this system. A two phase model is needed if accurate calculations are to be performed.

2. Unlike the case of the copper converter, solids (powdered coal) are injected into the slag fuming furnace along with gas. It is not known how this will affect the bubble formation and stirring effects within the furnace.

However, as no experimental or mathematical studies of the flow in a slag fuming furnace have been published to date, the mathematical model predictions are presented below as a general qualitative description of the flow in this vessel.

6.2.1. Assumptions

As with the previous calculations it was necessary to make several simplifying assumptions to allow computation of fluid flow profiles in this process vessel. All of the assumptions outlined in Section 6.1.1 were used, with the following additions:

1. The very high concentration of entrained gases in the liquid phase of the slag fuming furnace was taken into account by lowering the density of the furnace slag. Thus the actual slag density was assumed to be:

$$\rho = \rho_{slag} (1-\alpha) + \alpha \rho_g \qquad (6.3)$$

where α is the fraction of gas in the slag. This value was set to be 30% (9,10).

2. The effective viscosity of the furnace slag was calculated as for the copper converter.
3. The effects of the particle injection were neglected, along with the heat and gas evolution from coal oxidation.

The data used to model the furnace are presented in Table 6.2 and are taken from Richards (9,10).

6.2.2. Modifications to Program

The nature of the boundary conditions of the slag fuming furnace necessitated modifications to the SSMCR program. While both the experimental tank and the Peirce-Smith copper converter have flow regimes that are driven from only one side or from the surface, the slag-fuming furnace is driven from both sides. The finite difference code for the SSMCR program was written in central and backward differences, and calculations were repeatedly performed over the computational mesh from left to right (Section 4.3). This has the effect of "left-biasing" the flow - right side boundary conditions do not have as much effect as left side conditions.

A simple way of overcoming this difficulty is to rotate the mesh through 90 degrees. Unfortunately in this case, the influence of the free surface would be reduced and complicated by such a method.

In an attempt to reduce this effect while maintaining the free-surface conditions, calculation over the finite difference mesh was

altered to sweep from left to right, and then from right to left. The continuity equation was re-written in both forward and reverse finite difference approximations. However, the momentum equations and the free surface conditions were not altered and remained in their "left-justified" code.

Calculations performed with this new solution procedure were seen to have a diminished (but slightly noticeable) "left-biasing" effect - i.e. fluid flow profiles with identical left and right boundary conditions were not found to be perfectly symmetrical. However, due to the extreme difficulty in making additional adjustments to the SSMCR program, and the amount of approximation already introduced into these calculations, further refinements were not made to the program. All calculations shown below contain some of the "left-biasing" effect.

6.2.3. Mathematical Description of Bubble Column

Describing the bubble column in the slag fuming furnace was not as straightforward as that in the copper converter. Initially, the collapsing surface condition was applied. This produced plots such as Figure 6.3. It can be seen that this condition predicts the surface at the centre of the bath to rise as the left and right sides collapse. Therefore, if this condition were true, the slag bath would be constantly oscillating, with the centre velocities switching from positive to negative as the surface rose and fell.

Qualitative observations of the experimental tank when injected with air from two sides indicate that this is not what is occurring at all. The surface of the experimental tank was seen to be highly stable, and not to fluctuate to any significant extent. In addition, two stable and distinct vortices were observed to exist in the separate halves of the tank.

The reasons for the failure of the collapsing surface condition in this case have been discussed in the previous chapter, where it was noted that, although this boundary condition can result in accurate predictions, it is not necessarily an accurate description of what is occurring in the tank. With one-sided injection this was acceptable - the approximation of a collapsing surface successfully modelled the constant influx of high-velocity fluid falling away from the bubble column without creating obviously incorrect results. However, in the case of two-sided gas injection, the shortcomings of this approximation are more obvious, as it is evident from observations that the surface cannot possibly be continuously collapsing and reforming. The collapsing surface condition fails because it is forced to predict - by conservation of mass - a corresponding rise in the surface at the centre of the tank which is a physically unrealistic result.

This predicted surface rise does exist in the calculations made for the flow in the copper converter, as can be seen in Figure 6.2. However, since the surface is distorted less, and is collapsing from one side only, the effect is much less obvious.

Therefore, even though this condition can predict the expected high surface velocities in the slag fuming furnace, it should not be used, as the orientation of the predicted velocities must certainly be incorrect. Instead, the variable density and the constant velocity boundary conditions were employed to model the bubble column, in the hope of obtaining at least a correct qualitative description of the flow regime in the slag-fuming furnace.

The variable density condition has been shown to be the next most accurate boundary condition, after the collapsing surface approximation. The value used for the porosity of the bubble column was set to 80% to give the predictions of Figure 6.5. The wall velocity used to generate Figure 6.4 was 1.0 m/s.

6.2.4. Results

The results of the calculations performed on the zinc slag fuming furnace are shown in Figures 6.4 and 6.5. The general recirculatory nature of the flow is clearly discerned, with the fluid rotating in two distinct convective cells as mentioned earlier. The "left-biasing" is noticeable in the asymmetry of the flow pattern, particularly in the region of the right wall.

It must be stressed that the accuracy of these flow predictions is quite poor, even when compared to the predictions made for the flow in the copper converter.

However, even such inaccurate flow predictions as these indicate that the slag fuming furnace appears to be more highly stirred than the copper converter, with the fluid maintaining relatively high velocity throughout the vessel. As well, the slag in the centre of the furnace appears to acquire a very high downward velocity due to the meeting of the two opposing vortices. However, this seems to have the effect of leaving a relatively stagnant zone at the bottom centre of the tank, where the two vortices diverge.

7. CONCLUSIONS

7.1. Experimental

In the experimental section of this research, air was injected through side-mounted tuyeres into a water-filled plexiglas tank at modified Froude numbers varying from 0.4 to 15.6 and the resulting fluid velocity and surface profiles were recorded.

Under all conditions, the water was found to move in a recirculating vortex with the highest velocities in the region of the free surface. Little variation in flow was found through the width of the tank.

At gas injection rates greater than approximately 90 1/min. (corresponding to a modified Froude number of 2.3) the mean kinetic energy of the fluid was found to diminish with increasing air flowrate. Photographic evidence suggests that this effect is largely due to interaction of bubbles originating from adjacent tuyeres.

Integration of the steady-state surface profiles has shown that the experimental tank contains a significant amount of entrapped air. The air holdup in the tank has been seen to vary linearly with air flowrate.

7.2. Calculations - Agreement with Experimental Results

In an attempt to predict the experimental (and industrial) flow regimes, a mathematical model capable of predicting both fluid velocity and surface profiles in both rectangular and circular geometries has been developed, based on the SOLASMAC method of Hill (48). Turbulence has been modeled in the program by applying the Bousinesq approximation, and assuming a constant effective viscosity.

The algebraic viscosity model of Sahai and Guthrie (35) was tested, as were completely empirical viscosity values, and their respective predictions were compared with the experimental data. Overall, the model of Sahai and Guthrie was found to under-predict the effective viscosity in the experimental system.

A number of different boundary conditions were applied to the mathematical model in an attempt to predict the experimental flow patterns. The boundary approximation that was found to yield the most accurate results was the "collapsing surface" condition, wherein the recirculation of the fluid was driven from the free surface. This was the only boundary approximation tested that predicted the maximum fluid velocities to occur in the region of the free surface.

Based upon this observation, it was suggested that the stirring in the experimental tank was "driven" from the surface, and largely due to fluid falling away from the top of the bubble column across the free surface.

7.3. Industrial Calculations

7.3.1. Flow in a Copper Converter

Utilizing the "collapsing surface" boundary approximation, predictions have been made for the fluid flow regime in a Peirce-Smith copper converter. The effective viscosity was determined by redefining the constant K in the model of Sahai and Guthrie.

The resulting fluid flow profiles indicate that the stirring in the copper converter is very poor. The bath recirculates very slowly, with velocities in the bulk of the bath an order of magnitude lower than those occurring at the surface near the bubble column. It has been suggested that this is due to both the large amount of wall exposed to the bath, and the relatively short length of the bubble column.

It has also been proposed that the stirring efficiency would be much higher in a vertically-oriented cylindrical vessel, with air injected at the bottom.

7.3.2. Flow in the Zinc Slag-Fuming Furnace

With significant approximation, a qualitative prediction of the flow in a slag-fuming furnace has been made. Employing the constant upward velocity boundary condition, this prediction indicates that the fluid in the furnace recirculates in two counter-rotating vortices, with high velocities located in the centre of the vessel.

7.4. Recommendations for Further Work

It has been observed during the course of this investigation that the fluid within the mathematical model of the copper converter could be induced to "slop" by varying the left side boundary condition. That is, under the right conditions, the program predicts a collapse of the fluid surface at the left side of the converter, and a corresponding rise in the right side fluid.

It is suggested that this "slopping" behaviour in the mathematical model be investigated more fully, to possibly yield information on the prevention of this phenomenon in industrial practice.

REFERENCES

1. T. Rosenqvist, Principles of Extractive Metallurgy, McGraw-Hill, 1974.
2. R.D. Pehlke, Unit Processes of Extractive Metallurgy, Elsevier North Holland, 1973.
3. N.J. Themelis, P. Tarassoff and J. Szekely, Trans. AIME 245, p. 2425, 1969.
4. K. Nakanishi and J. Szekely, Unpublished Research, from J. Szekely, "Turbulence Phenomena in Agitated Ladles - Heat Mass and Momentum Transfer", Scaninject I, p. 5:1, 1977.
5. R.M. Figueira and J. Szekely, Met. Trans. B, 16B, March 1985, pp. 67-75.
6. Encyclopedia Britanica, 15th ed., Vol. 8, 1985.
7. E.O. Hoefele and J.K. Brimacombe, Met. Trans. B, Vol. 10B, pp. 631-648, 1979.
8. G.G. Richards, Unpublished Research, 1986.
9. G.G. Richards, Ph.D. Thesis, University of British Columbia, 1983.
10. G.G. Richards, J.K. Brimacombe and G.W. Toop, "Kinetics of the Slag Fuming Furnace, Parts I-III, Met. Trans. B, 16B, Sept. 1985, pp. 513-549.
11. G.N. Oryall, M.A.Sc. Thesis, The University of British Columbia, 1975.
12. G.N. Oryall and J.K. Brimacombe, Met. Trans. B, 7B, pp. 391-403, 1976.
13. G.A. Irons and R.I.L. Guthrie, Met. Trans. B, 9B, pp. 101-110, 1978.
14. A.E. Wraith and M.E. Chalkley, "Advances in Extractive Metallurgy", Int. Symp. Inst. Min. Metall., London, pp. 27-33, 1977.

15. D.W. Ashman, J.W. McKelliget and J.K. Brimacombe, Can. Metall. Quart., Vol. 20, 4, pp. 387-395, 1981.

16. J.F. Davidson and B.O.G. Schuler, Trans. Inst. Chem. Engrs., 38, p. 335, 1960.

17. A.A. Bustos, G.G. Richards, N.B. Gray and J.K. Briacombe, Met. Trans. B, 15B, 3, pp. 77-89, 1984.

18. R. Kumar and N.R. Kuloor, Adv. Chem. Engng. 8, p. 255, 1979.

19. R. Clift, J.R. Grace and M.E. Weber, Bubbles, Drops and Particles, Academic Press, New York, pp. 321-328, 1978.

20. M. Nilmani and D.G.C. Robertson, "Gas Injection into Liquid Metals", University of Newcastle-upon-Tyne, 1979.

21. M. Nilmani and D.G.C. Robertson, Inst. Min. Metall., pp. C42-53, March, 1980.

22. P.S. Bulson, Dock and Harbour Authority, May 1961, pp. 15-22.

23. A. Kumar, T.E. Degaleesan, G.S. Laddha and H.E. Hoelscher, Can. J. Chem. Eng., 54, pp. 503-508, 1976.

24. J. Szekely and S. Asai, Trans. ISIJ, Vol. 15, pp. 276-285, 1975.

25. J. Szekely and S. Asai, Trans. ISIJ, Vol. 15, pp. 270-275, 1975.

26. J. Szekely, H.J. Wang and K.M. Kiser, Met. Trans. B, 7B, pp. 287-295, June 1976.

27. M. Salcudean and R.I.L. Guthrie, Met. Trans. B, 9B, pp. 181-189, June 1978.

28. M. Salcudean and R.I.L. Guthrie, Met. Trans. B, 9B, pp. 673-680, December 1978.

29. M. Salcudean and R.I.L. Guthrie, Met. Trans. B, 10B, pp. 423-429, September 1979.

30. J. Szekely, A.H. Dilawari and R. Metz, Met. Trans. B, 10B, pp. 33-41, March 1979.

31. J. Szekely, N.H. El-Kaddah and J.H. Gravet, pp. 5:1-5, Scaninject II, Lulea, Sweden, June 1980.

32. T. Hsiao, T. Lehner and B. Kjellberg, Scand. J., Met., 9, pp. 105-110, 1980.

33. Y. Sahai and R.I.L. Guthrie, Met. Trans. B, 13B, June 1982, pp. 193-202.

34. Y. Sahai and R.I.L. Guthrie, Met. Trans. B, 13B, June 1982, pp. 203-211.

35. Oeters, Dropmar and Kepurga, Scaninject II, Lulea, Sweden, June 1980.

36. D. Mazumdar and R.I.L. Guthrie, Met. Trans. B, 16B, March 1985, pp. 83-89.

37. O. Haida and J.K. Brimacombe, Trans. ISIJ, Vol. 25, 1985, pp. 14-20.

38. A.D. Gosman, W.M. Pun, A.K. Runchal, D.B. Spalding and M. Wolfshtein, Heat and Mass Transfer in Recirculating Flow, London and New York, Academic Press, 1969.

39. D.B. Spalding, VDI-Forsch, 38, 5, 1972.

40. T. Deb Roy, A.K. Majumdar and D.B. Spalding, Appl. Math. Modelling, 1978, Vol. 2, pp. 146-150.

41. W.M. Pun and D.B. Spalding, Proceedings XVIII International Astronautical Congress, Pergamon Press, 1967, Vol. 3, pp. 3-21.

42. J.H. Grevet, J. Szekely and N. El-Kaddah, Int. J. Heat Transfer, Vol. 25, 4, pp. 487-497.

43. N. El-Kaddah and J. Szekely, Injection Phenomena in Extraction and Refining, 1982, PR1-R19.

44. Y. Sahai and R.I.L. Guthrie, Met. Trans. B, 13B, March 1982, pp.125-127.

45. S.V. Patankar and D.B. Spalding, Int. J. Heat Mass Transfer, 15, 1972, 1787.

46. M. Salcudean, C.H. Low, A. Hurda and R.I.L. Guthrie, Chem. Eng. Commun., Vol. 21, pp. 89-103, 1983.

47. M. Salcudean and R.C.L. Wong, Scientific Computing, IACS, North-Holland Publishing Company, pp. 329-336, 1983.

48. M. Salcudean, K.Y.M. Lai and R.I.L. Guthrie, Can. J. Chem. Eng., 63, February 1985, pp. 51-60.

49. D. Mazumdar and R.I.L. Guthrie, Met. Trans. B, Vol. 16B, pp. 83-90, 1985.

50. W.P. Jones and B.E. Launder, Int. J. Heat Mass Transfer, Vol. 15, pp. 301-314, 1972.

51. R.E. Nickell, R.I. Tanner and B. Caswell, J. Fluid Mech., Vol. 65, pp. 189-206, 1974.

52. R.I. Tanner, R.E. Nickell and R.W. Bilger, Comput. Methods Appl. Mech. Eng., Vol. 6, pp. 155-174, 1975.

53. R.V. Southwell, Proc. Roy Soc., pp. 117-160, 1946.

54. F.H. Harlow and J.E. Welch, Phys. Fluids, Vol. 8, 12, December 1965, pp. 2182-2189.

55. J.A. Viecelli, J. Comp. Phys., 4, 1969, p. 543.

56. J.A. Viecelli, J. Comp. Phys., 8, 1971, pp. 119-143.

57. G.A. Hill, Ph.D. Thesis, Univerisity of Saskatchewan, 1979.

58. C.W. Hirt, B.N. Nichols and N.C. Romero, LA - 5852, Los Alamos Scientific Laboratory, New Mexico, 1975.

59. A.A. Amsden and F.H. Harlow, LA - 4370, Los Alamos Scientific Laboratory, New Mexico, 1970.

60. C.W. Hint and J.P. Shannon, J. Comp. Phys., 2, 403-411, 1968, pp. 403-411.

61. W.E. Pracht, J. Comput. Phys., Vol. 17, pp. 132-159, 1975.

62. F. Pan and A. Acrivos, J. Fluid Mech., Vol. 28, 4, pp. 643-655.

63. Copper and Nickel Converters, R.E. Johnson ed., Metall. Soc. AIME, New York, 1979.

64. W.G. Davenport, J. Iron and Steel Inst., Oct. 1967, pp. 1034-1042.

65. W.E.R. Davies and J.I. Unger, UTIAS Tech. Note 185, January 1973.

66. F. Durst and M. Zaré, Proc. LDA - Symposium, Copenhagen, 1975, pp. 403-429.

67. Scaninject, International Conference on Injection Metallurgy, Lulea, Sweden, July 9-10, 1977.

68. Scaninject II, 2nd International Conference on Injection Metallurgy, Lulea, Sweden, June 12-13, 1980.

69. Scaninject IV, 4th International Conference on Injection Metallurgy, Lulea, Sweden, June 11-13, 1986.

70. Gas Injection into Liquid Metals, University of Newcastle upon Tyne, 1979.

71. T. Deb Roy, A.K. Majumdar, J. Metals, November 1981. pp. 42-47.

72. N. Takemitsu, J. Comput. Phys., 36, pp. 236-248, 1980.

73. G. de Vahl Davis and G.D. Mallinson, Computers and Fluids, Vol. 4, pp. 29-43, 1976.

74. W.S. Hwang and R.A. Stoehr, J. Metals, October 1983, pp. 22-28.

75. T. Miyauchi and H. Oya, AiChE, Journal, Vol. 11, 3, pp. 395-402, 1965.

76. J.L.L. Baker and B.T. Chao, AiChE Journal, Vol. 11, 3, pp. 268-273, 1965.

77. R.D. Mills, J. Roy. Aero. Soc., 69, Feb. 1965, pp. 116-120.

78. B.J. Daly, J. Comput. Phys., 4, pp. 97-117, 1969.

79. E.O. Hoefele, M.A.Sc. Thesis, The University of British Columbia, 1978.

80. C.O. Bennett and J.E. Myers, Momentum, Heat and Mass Transfer, 2nd ed., McGraw-Hill, New York, 1962.

81. R.B. Bird, W.E. Stewart and E.N. Lightfoot, Transport Phenomena, John Wiley and Sons, New York, 1960.

82. Injection Phenomena in Extraction and Refining, University of Newcastle, April 1982.

APPENDIX 1

Finite-Difference Approximations used by SSMCR

1. Continuity Equation:

$$\frac{\partial u}{\partial x} + \frac{\partial v}{\partial y} = 0$$

where

$$\frac{\partial u}{\partial x} = \frac{u_{i,j} - u_{i-1,j}}{\Delta x}$$

$$\frac{\partial v}{\partial y} = \frac{v_{i,j} - v_{i,j-1}}{\Delta y}$$

2. x-Wise Momentum Equation:

$$\frac{\partial u}{\partial t} = -\frac{1}{\rho}\frac{\partial p}{\partial x} - g_x - \frac{\partial (uv)}{\partial y} - \frac{\partial (u^2)}{\partial x} + \frac{\mu_{eff}}{\rho}\left[\frac{\partial^2 u}{\partial x^2} + \frac{\partial^2 u}{\partial y^2}\right]$$

where:

$$\frac{\partial u}{\partial t} = \frac{u^{t+\Delta t} - u}{\Delta t}$$

$$-\frac{1}{\rho}\frac{\partial p}{\partial x} = \frac{p_{i,j} - p_{i+1,j}}{\rho \Delta x}$$

$$\frac{\partial (u^2)}{\partial x} = \frac{(u_{i,j} + u_{i+1,j})^2 - (u_{i-1,j} + u_{i,j})^2}{4\Delta x}$$

$$+ \frac{\gamma \left| u_{i,j} + u_{i+1,j} \right| (u_{i,j} - u_{i+1,j}) - \gamma \left| u_{i-1,j} + u_{i,j} \right| (u_{i-1,j} - u_{i,j})}{4\Delta x}$$

$$\frac{\partial(uv)}{\partial y} = \frac{(u_{i,j} + u_{i,j+1})(v_{ij} + v_{i+1,j}) - (u_{i,j} + u_{i,j-1})(v_{i,j-1} + v_{i+1,j-1})}{4\Delta y}$$

$$+ \frac{\gamma \left| v_{i,j} + v_{i+1,j} \right| (u_{i,j} - u_{i,j+1}) - \gamma \left| v_{i,j-1} + v_{i+1,j-1} \right| (u_{i,j-1} - u_{i,j})}{4\Delta y}$$

$$\frac{\mu_{eff}}{\rho}\left(\frac{\partial^2 u}{\partial x^2} + \frac{\partial^2 u}{\partial y^2}\right) = \frac{\mu_{eff}}{\rho}\left[\frac{u_{i+1,j} - 2u_{i,j} + u_{i-1,j}}{\Delta x^2} + \frac{u_{i,j+1} - 2u_{i,j} + u_{i,j-1}}{\Delta y^2}\right]$$

3. y-Wise Momentum Equation:

$$\frac{\partial v}{\partial t} = -\frac{1}{\rho}\frac{\partial p}{\partial y} - g_y - \frac{\partial(uv)}{\partial x} - \frac{\partial(v^2)}{\partial y} + \frac{\mu_{eff}}{\rho}\left[\frac{\partial^2 v}{\partial x^2} + \frac{\partial^2 v}{\partial y^2}\right]$$

where:

$$\frac{\partial v}{\partial t} = \frac{v^{t+\Delta t} - v}{\Delta t}$$

$$-\frac{1}{\rho}\frac{\partial p}{\partial y} = \frac{p_{i,j} - p_{i,j+1}}{\rho \Delta y}$$

$$\frac{\partial(v^2)}{\partial y} = \frac{(v_{i,j} + v_{i,j+1})^2 - (v_{i,j-1} + v_{i,j})^2}{4\Delta y}$$

$$+ \frac{\gamma \left| v_{i,j} + v_{i,j+1} \right| (v_{i,j} - v_{i,j+1}) - \gamma \left| v_{i,j-1} + v_{i,j} \right| (v_{i,j-1} - v_{i,j})}{4\Delta y}$$

$$\frac{\partial(uv)}{\partial x} = \frac{(u_{i,j} + u_{i,j+1})(v_{i,j} + v_{i+1,j}) - (u_{i-1,j} + u_{i-1,j+1})(v_{i-1,j} + v_{i,j})}{4\Delta x}$$

$$+ \frac{\gamma \left| u_{i,j} + u_{i,j+1} \right| (v_{i,j} - v_{i+1,j}) - \gamma \left| u_{i-1,j} + u_{i-1,j+1} \right| (v_{i-1,j} - V_{i,j})}{4\Delta x}$$

$$\frac{\mu_{eff}}{\rho}\left(\frac{\partial^2 v}{\partial x^2}+\frac{\partial^2 v}{\partial y^2}\right) = \frac{\mu_{eff}}{\rho}\left[\frac{v_{i+1,j}-2v_{i,j}+v_{i-1,j}}{\Delta x^2}+\frac{v_{i,j+1}-2v_{i,j}+v_{i,j-1}}{\Delta y^2}\right]$$

In these equations, γ is used to vary the amount of upwind differencing.

TABLES

Table 3.1. Experimental Air Injection Rates

Run Number	Air Flowrate (std l/min)	$N_{Fr'}$
1	38	0.43
2	68	1.40
3	78	1.80
4	88	2.30
5	120	4.40
6	142	6.30
7	154	7.40
8	166	8.70
9	178	10.20
10	216	15.60

Table 3.2. Values of $\frac{\Delta w}{\Delta z}$ at Six Locations in Experimental Tank, Experiment Number 1

Cell Location i	Cell Location j	$\frac{\Delta w}{\Delta z}$ (s^{-1})
3	3	3.4
4	4	3.8
5	5	1.5
6	6	-1.4
7	7	-3.1
8	8	-0.4

Table 3.3. Minimum Mean Values of $\frac{\Delta w}{\Delta z}$ of Experimental Runs

Experiment Number	$\frac{\Delta w}{\Delta z}$ (s^{-1})
1	1.30
2	1.60
3	0.76
4	0.90
5	2.40
6	1.10
7	0.88
8	2.90
9	1.20
10	3.00

Table 4.1. Approximations Used for Rectangular Wall Boundaries

Type of Wall	No Slip	Free Slip
Vertical	$u_{i,j} = 0$	$u_{i,j} = 0$
	$v_{i,j} = -v_{i-1,j}$	$v_{i,j} = v_{i-1,j}$
Horizontal	$u_{i,j} = -u_{i,j+1}$	$u_{i,j} = u_{i,j+1}$
	$v_{i,j} = 0$	$v_{i,j} = 0$

Table 5.1. Effective Viscosity Values Predicted by the Model of Sahai and Guthrie (44)

Experiment Number	$\mu_{eff}(\frac{g}{cms})$
1	2.9
2	3.4
3	3.5
4	3.6
5	3.8
6	3.8
7	3.8
8	3.8
9	3.8
10	3.5

Table 5.2. Comparison of Results Calculated by Constant Velocity Condition with Experiments

Run Name	μ_{eff}(g/cms)	Left Wall Velocity(m/s)	Deviation Values	Experiment Number									
				1	2	3	4	5	6	7	8	9	10
VC8.6	3	1.0	$\bar{D}_{mag}$	87.8	86.9	88.9	89.0	86.9	87.9	87.8	86.2	86.4	84.5
			$\bar{D}_{\theta}$	-40.1	-32.3	-34.3	-35.4	-33.2	-35.1	-26.8	-33.2	-20.7	-27.0
			$\bar{D}_{dist}$	47.7	44.3	40.1	41.9	39.1	35.1	45.3	49.6	52.9	45.7
VC6.6	10	0.80	$\bar{D}_{mag}$	67.6	65.4	69.3	70.5	66.6	64.8	67.2	65.5	62.6	65.6
			$\bar{D}_{\theta}$	-62.6	-54.0	-57.5	-52.1	-39.0	-51.6	-47.8	-48.5	-39.6	-47.2
			$\bar{D}_{dist}$	44.3	40.9	33.4	37.6	37.8	24.2	40.9	49.4	48.1	42.4
VC.4	40	0.80	$\bar{D}_{mag}$	51.1	46	53.1	55.4	48.9	44.1	50.9	46.6	45.1	49.2
			$\bar{D}_{\theta}$	-81.5	-70.6	-76.6	-71.1	-58.0	-64.1	-62.4	-67.5	-57.4	-60.2
			$\bar{D}_{dist}$	39.4	33.5	26.5	31.8	31.6	13.1	36.2	43.5	45.1	38.7
VC2.8	400	0.80	$\bar{D}_{mag}$	15.8	9.8	19.9	25.4	10.9	16.3	18.4	5.5	13.1	9.1
			$\bar{D}_{\theta}$	-50.6	-41.2	-46.3	-41.0	-31.0	-37.1	-30.8	-39.7	-25.5	-31.5
			$\bar{D}_{dist}$	24.2	19.4	8.9	17.4	13.3	5.7	23.0	27.5	36.9	20.4
VC7.4	400	1.0	$\bar{D}_{mag}$	-0.6	6.7	3.2	10.3	-6.5	0.6	1.3	-12.4	-5.8	-17.0
			$\bar{D}_{\theta}$	-63.3	-54.8	-59.1	-53.8	-41.1	-46.8	-43.2	-50.2	-36.8	-17.8
			$\bar{D}_{dist}$	22.0	17.8	5.1	14.3	10.7	3.4	19.7	25.7	33.8	8.2

Table 5.3. Estimated Experimental Bubble Column Porosity Values

Experiment Number	Bubble Column Porosity
1	8.7
2	19.6
3	24.1
4	26.7
5	34.9
6	43.6
7	51.9
8	56.2
9	57.2
10	70.6

Table 5.4. Comparison of Results Calculated by Variable Density Condition with Experiments

					Experiment Number									
Run Name	μ_{eff}(g/cms)	Porosity(%)	Left Wall Velocity(m/s)	Deviation Values	1	2	3	4	5	6	7	8	9	10
VK.4	400	30.0	0.0	$\bar{D}_{mag}$	99.8	99.8	99.8	99.8	99.8	99.8	99.8	99.8	99.8	99.8
				$\bar{D}_{\theta}$	-12.1	-12.4	2.1	-2.6	-8.9	-8.1	0.3	-3.6	4.3	-3.9
				$\bar{D}_{dist}$	23.7	19.0	7.1	15.1	16.5	-10.7	21.3	30.5	30.1	22.2
VL.4	400	30.0	0.4	$\bar{D}_{mag}$	57.2	59.8	65.6	65.0	67.3	61.6	58.9	63.8	59.0	60.9
				$\bar{D}_{\theta}$	-35.3	-25.7	-31.1	-28.7	-25.9	-21.6	-24.8	-21.9	-27.0	-17.8
				$\bar{D}_{dist}$	10.8	16.7	9.4	18.2	16.0	13.4	-7.3	20.9	27.0	20.5

Table 5.5. Comparison of Results Calculated by Pulsed Boundary Condition with Experiments

					Experiment Number									
Run No.	Bubble Frequency	Rise Velocity	μ_{eff}	Deviation Values	1	2	3	4	5	6	7	8	9	10
BB2.4	20	1.0	400	$\bar{D}_{mag}$	29.4	22.4	30.3	34.8	24.9	17.6	26.6	21.2	20.7	19.5
				$\bar{D}_{\theta}$	-76	-66.4	-72.3	-66.9	-54.3	-60	-56.6	-63.3	-51.4	-54.3
				$\bar{D}_{dist}$	21.1	13.8	1.52	10.2	9.2	-15.5	13.9	24.8	28.4	12.3
BB2.4	20	0.8	400	$\bar{D}_{mag}$	30.7	25.1	33.7	38.1	27.5	27.6	32.8	24.5	26.1	28.2
				$\bar{D}_{\theta}$	-67.9	-59.2	-62.5	-57.2	-44.6	-50.3	-47.6	-53.6	-42.4	-49.1
				$\bar{D}_{dist}$	26.8	21.4	11.5	19.6	17.2	4.3	25.6	32.0	37.1	26.2
BB3.8	10	1.0	40	$\bar{D}_{mag}$	68.3	64.6	69.9	71.2	66.5	64.5	68.5	65.5	64.3	67.3
				$\bar{D}_{\theta}$	-76.7	-67.7	-70.9	-65.4	-52.7	-58.4	-57.1	-61.8	-53.6	-60.6
				$\bar{D}_{dist}$	43.9	37.8	32.7	37.3	36.0	-21.3	40.8	48.0	49.0	43.7
BB4.7	10	1.0	400	$\bar{D}_{mag}$	20.4	12.3	21.9	26.8	16.5	5.5	18.2	12.6	11.8	11.6
				$\bar{D}_{\theta}$	-78.7	-68.5	-74.4	-69.0	-56.3	-62.1	-59.1	-65.4	-54.1	-57.1
				$\bar{D}_{dist}$	21.5	14.1	2.8	11.0	11.0	-16.7	15.5	26.5	29.9	15.2

Table 5.6. Comparison of Results Calculated by Collapsing Surface Condition with Experiments

				Experiment Number									
Run Name	μ_{eff}(g/cms)	Left Wall Velocity(m/s)	Deviation Values	1	2	3	4	5	6	7	8	9	10
S.COL.4	400	0.0	$\bar{D}_{mag}$	99.9	99.9	99.9	99.9	99.9	99.9	99.9	99.9	99.9	99.9
			$\bar{D}_{\theta}$	0.9	2.9	5.4	6.5	10.9	5.1	0.8	-18.0	27.0	14.1
			$\bar{D}_{dist}$	14.5	-8.1	-3.0	7.8	12.4	3.6	-5.5	27.7	15.6	12.2
VG.6	400	70.0	$\bar{D}_{mag}$	24.7	19.1	29.0	33.3	21.1	21.9	27.0	16.1	22.2	19.8
			$\bar{D}_{\theta}$	-40.1	-30.6	-35.4	-30.3	-23.9	-30.7	-27.8	-33.2	-14.6	-23.7
			$\bar{D}_{dist}$	24.1	18.9	9.6	17.3	14.0	1.4	22.8	27.9	36.7	21.3

Table 6.1. Data Used to Model Flow in Peirce-Smith Copper Converter

Quantity	Value
Bath Density	4600 kg/m^3
Bath Viscosity @ 1200°C	0.1 g/cms
Furnace Diameter	3.85 m
Tuyere Submergence	0.35 m

Table 6.2. Data Used to Model Flow in Zinc Slag Fuming Furnace

Quantity	Value
Bath Density	3500 kg/m^3
Bath Viscosity	0.2 g/cms
Furnace Width	2.9 m
Tuyere Submergence	0.68 m
Slag Porosity	0.30

FIGURES

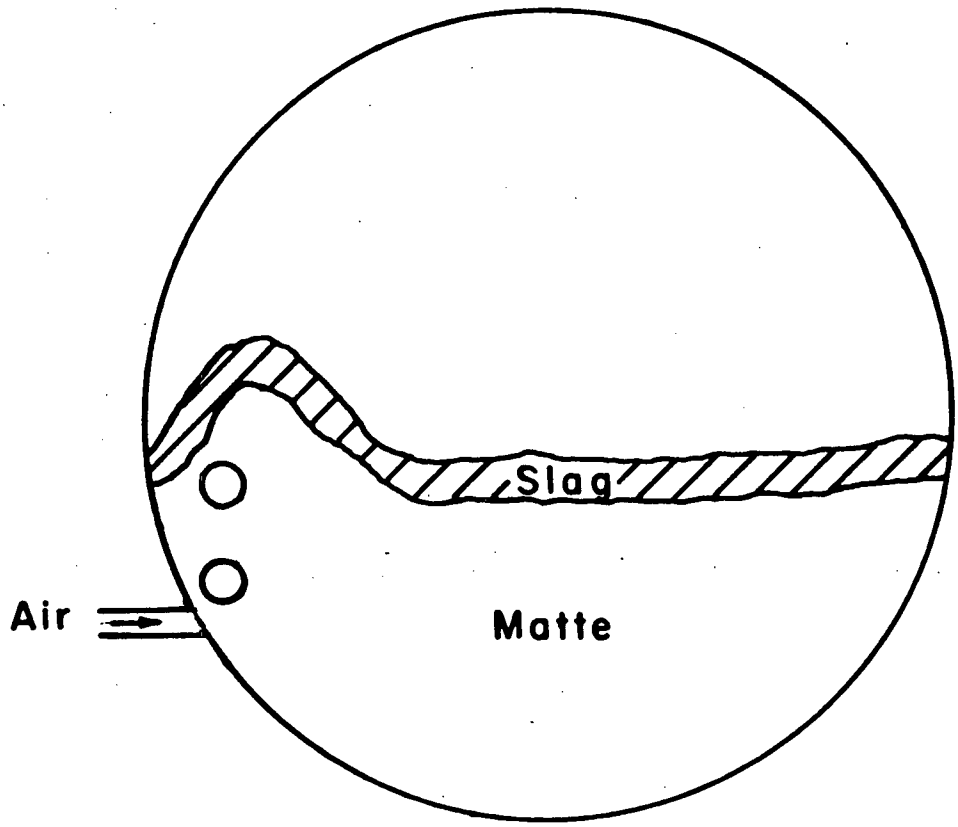

Figure 1.1. Schematic Diagram of Peirce-Smith Copper Converter.

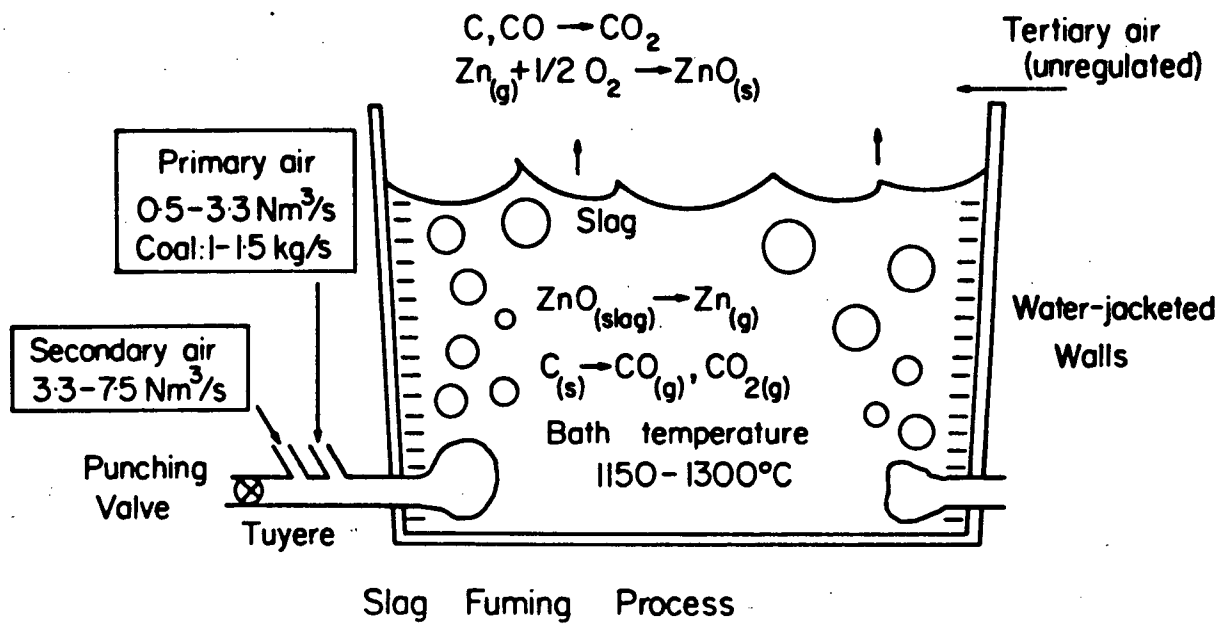

Slag Fuming Process

Figure 1.2. Schematic Diagram of Zinc Slag Fuming Furnace.

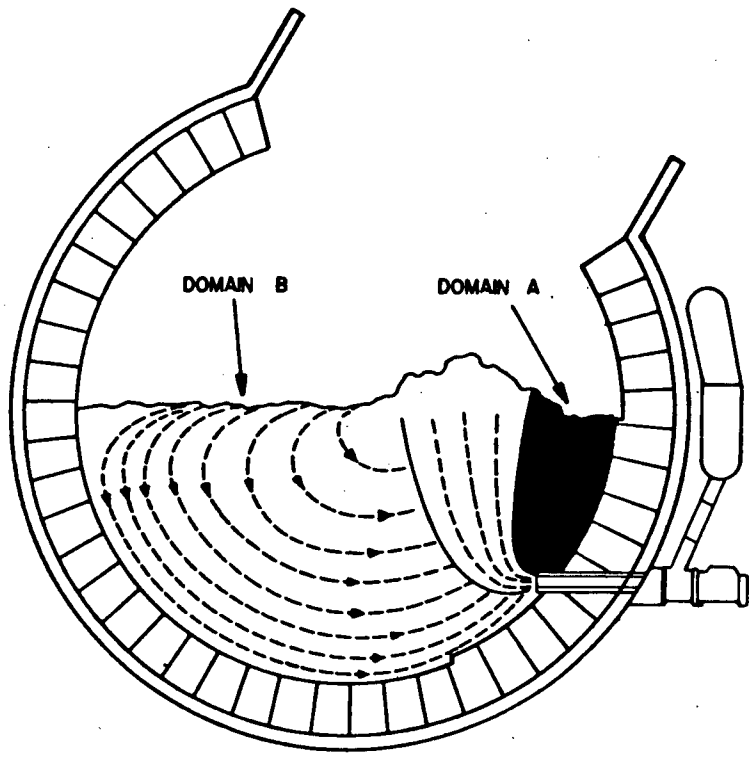

Figure 2.1. Estimate of Flow in a Copper Converter, from Themelis et al. (3).

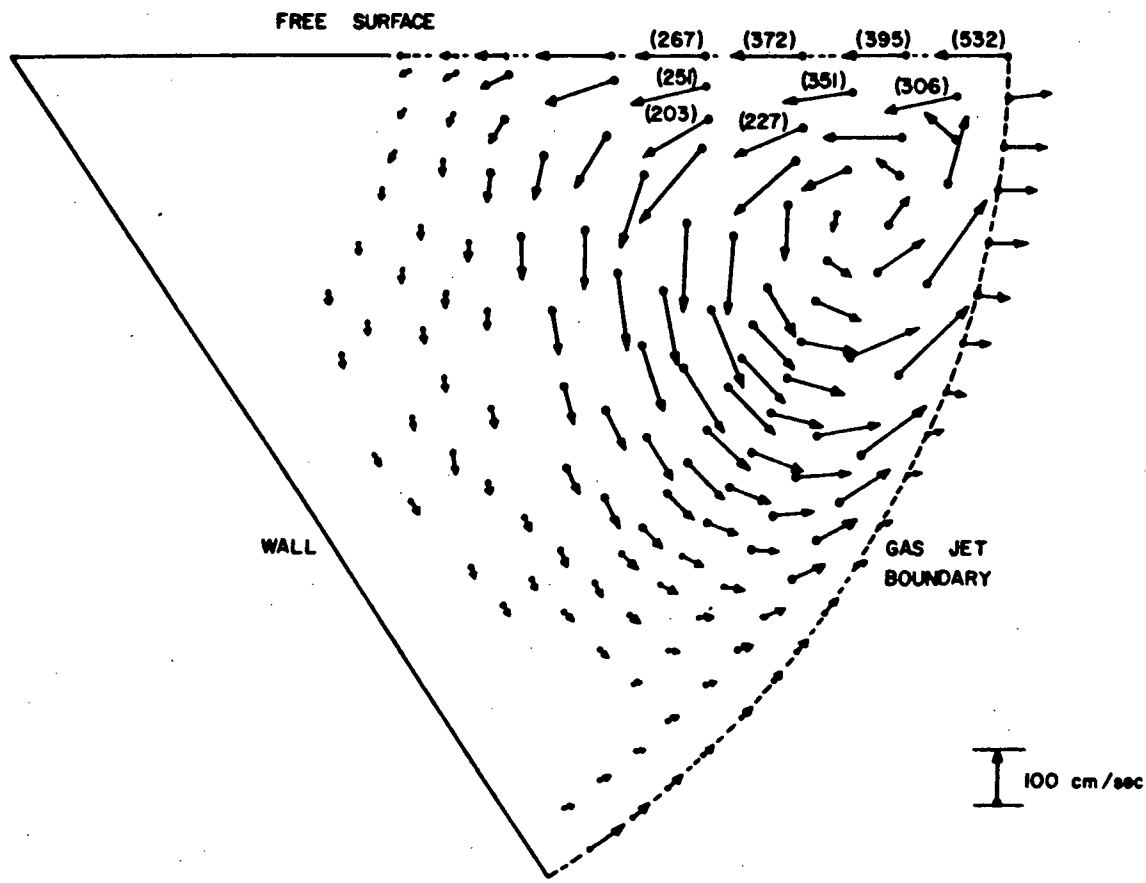

Figure 2.2. Predicted Flow Profile in Two-Phase Region of Copper Converter, from Nakanishi and Szekely (4).

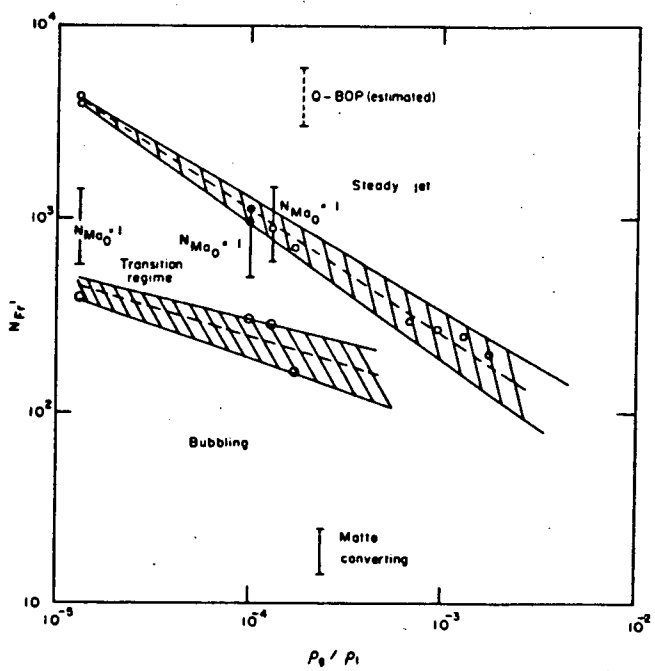

Figure 2.3. Jet Behaviour Diagram, from Hoefele and Brimacombe (7).

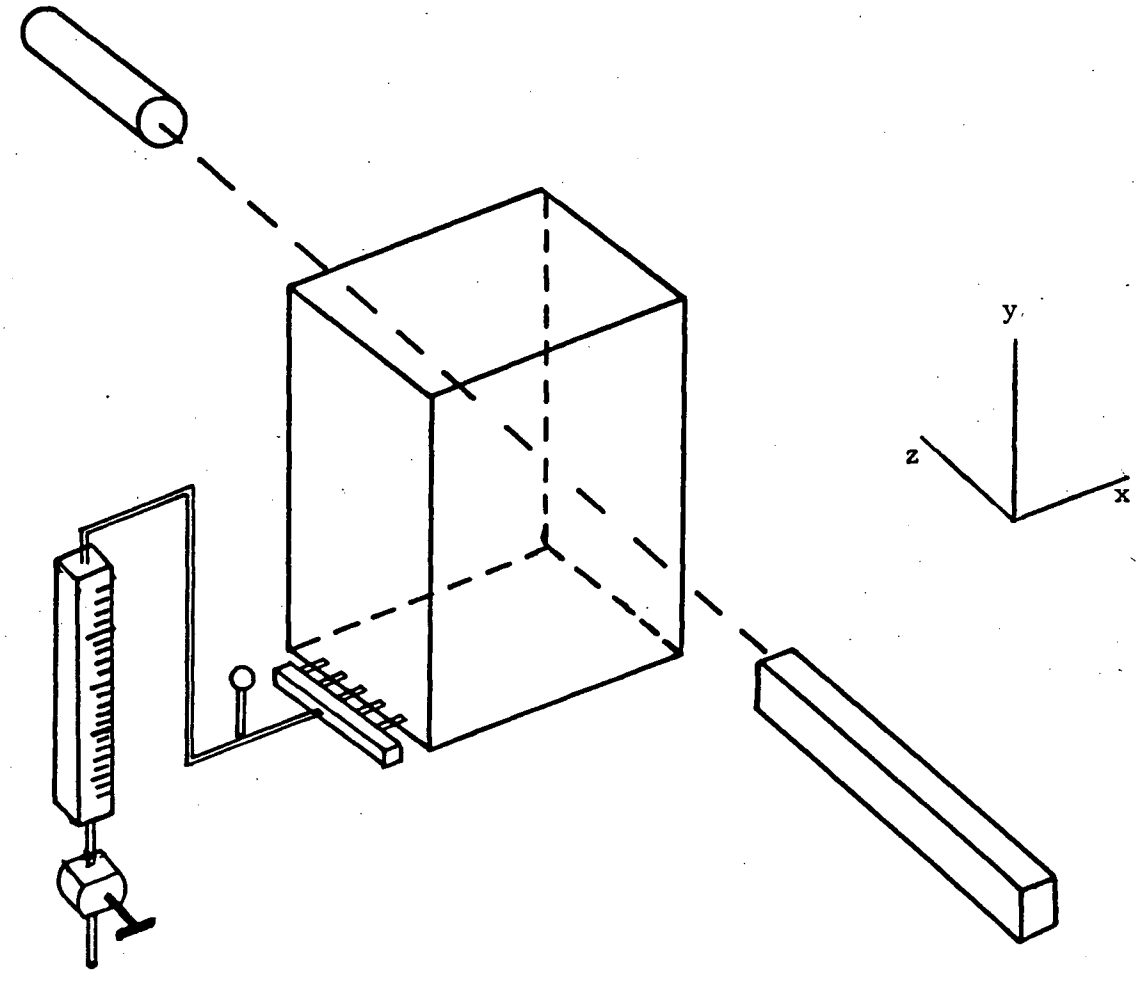

Figure 3.1. Schematic Diagram of Experimental Apparatus.

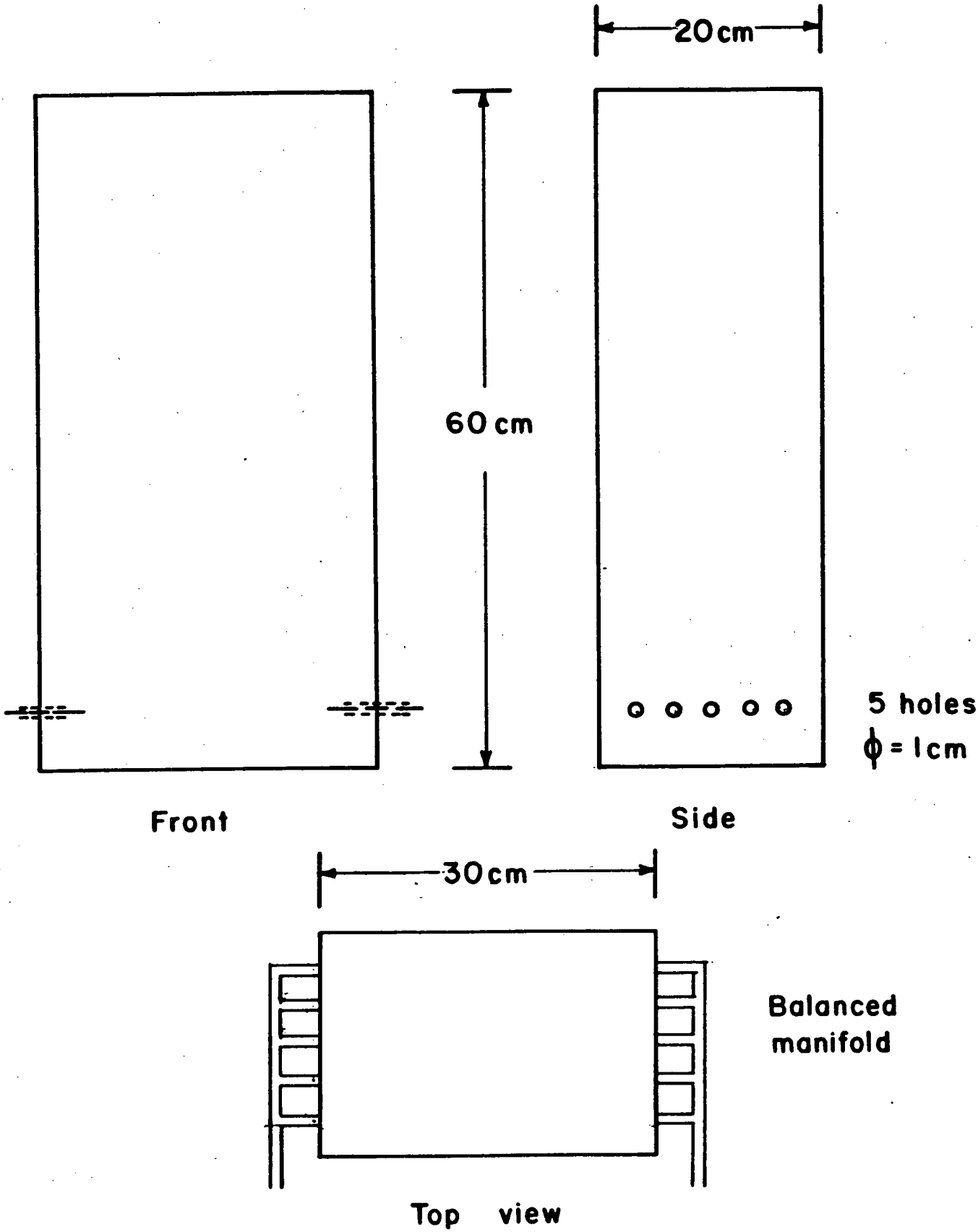

Figure 3.2. Dimensions and Construction of Experimental Tank.

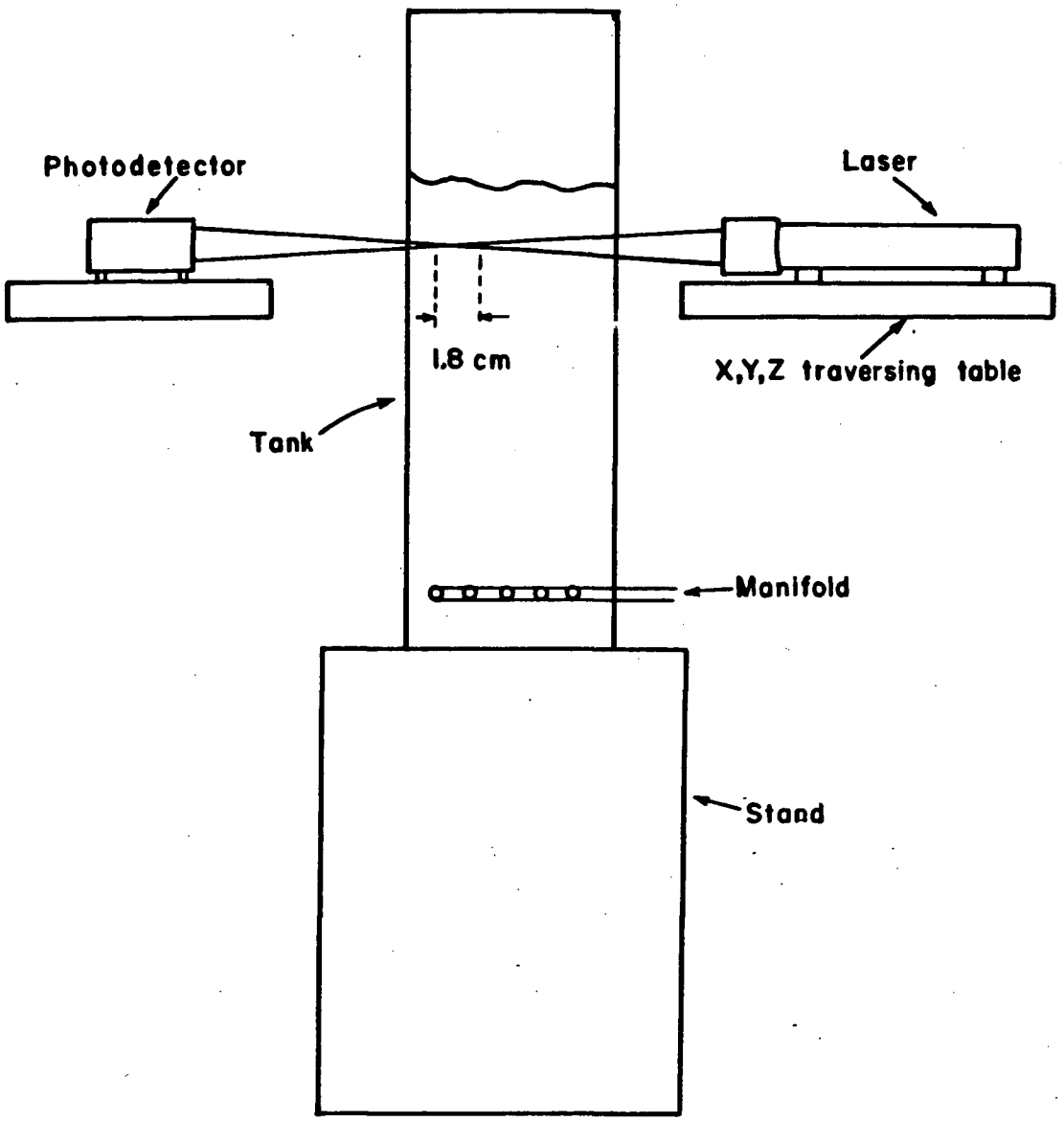

Figure 3.3. Diagram of Laser-Doppler System.

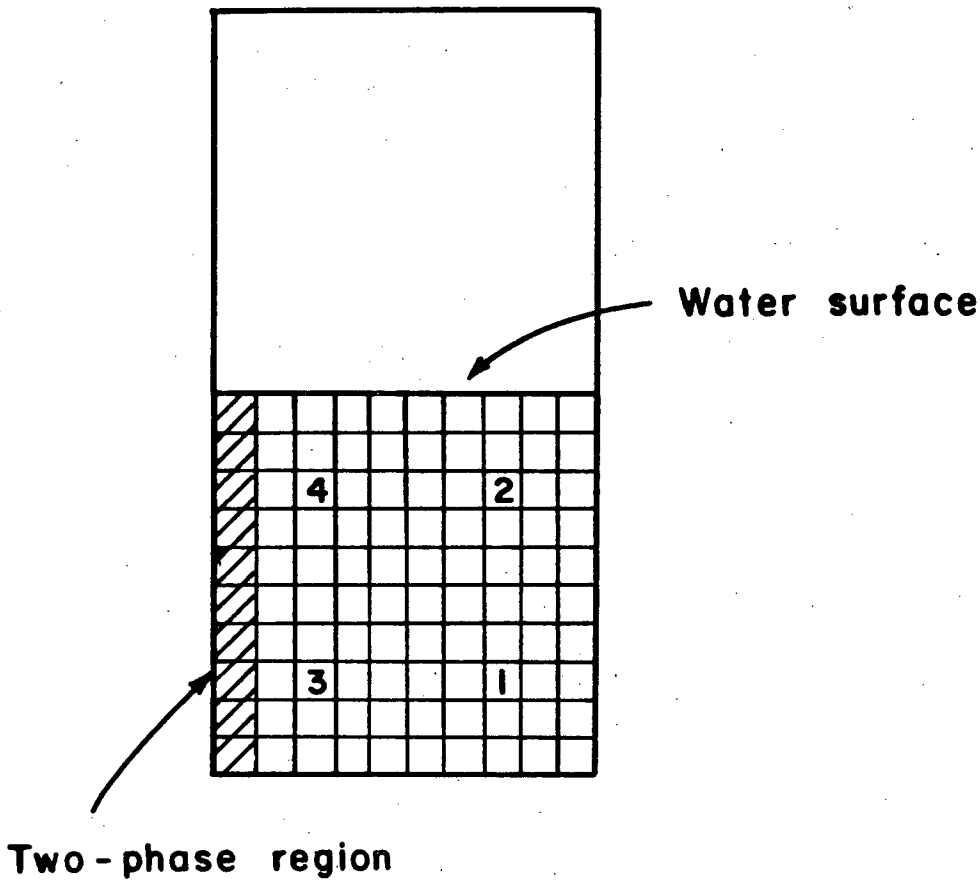

Figure 3.4. Velocity Measurement Locations Within Experimental Tank.

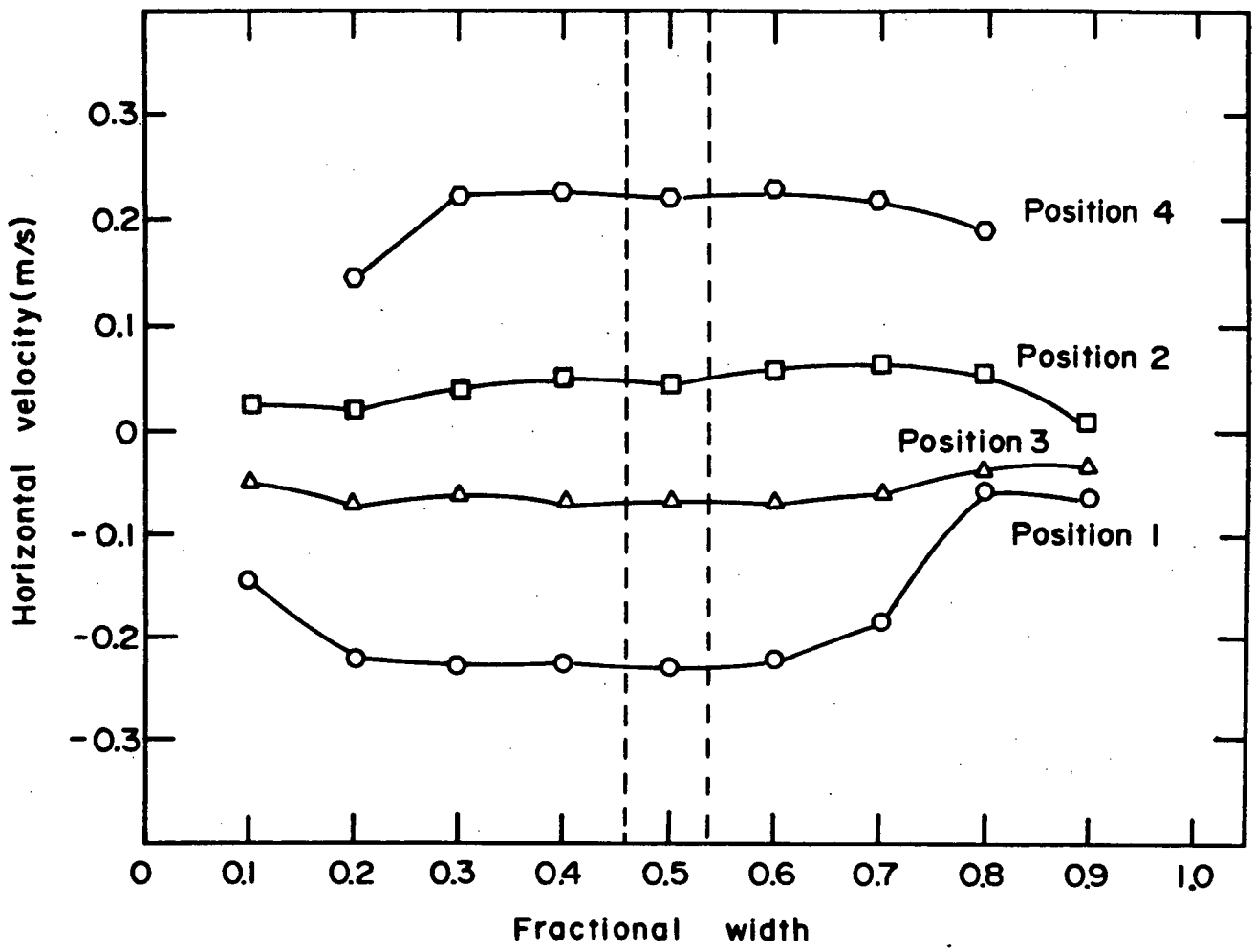

Figure 3.5. Horizontal Velocity Variation Through Depth of Tank.

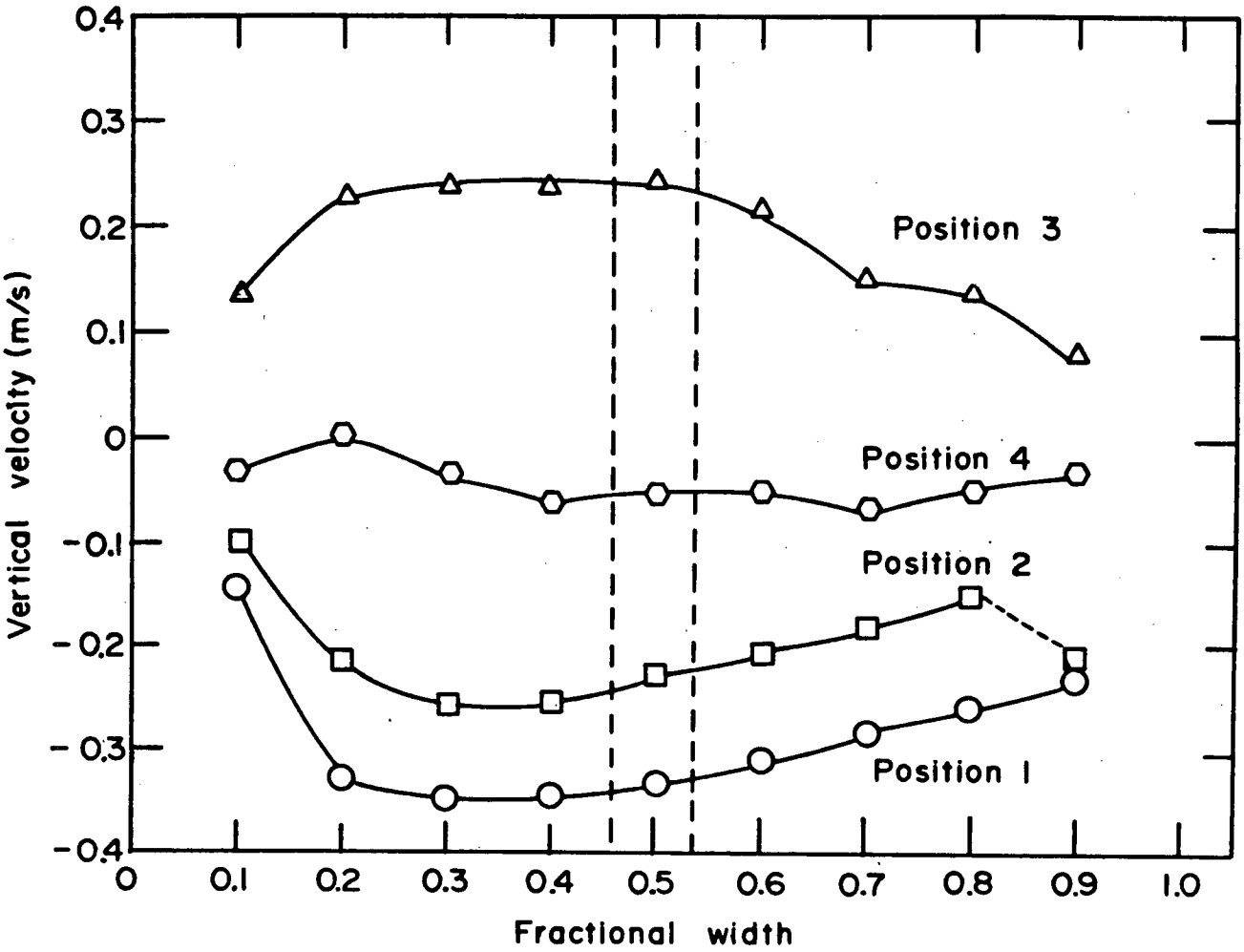

Figure 3.6. Vertical Velocity Variation Through Depth of Tank.

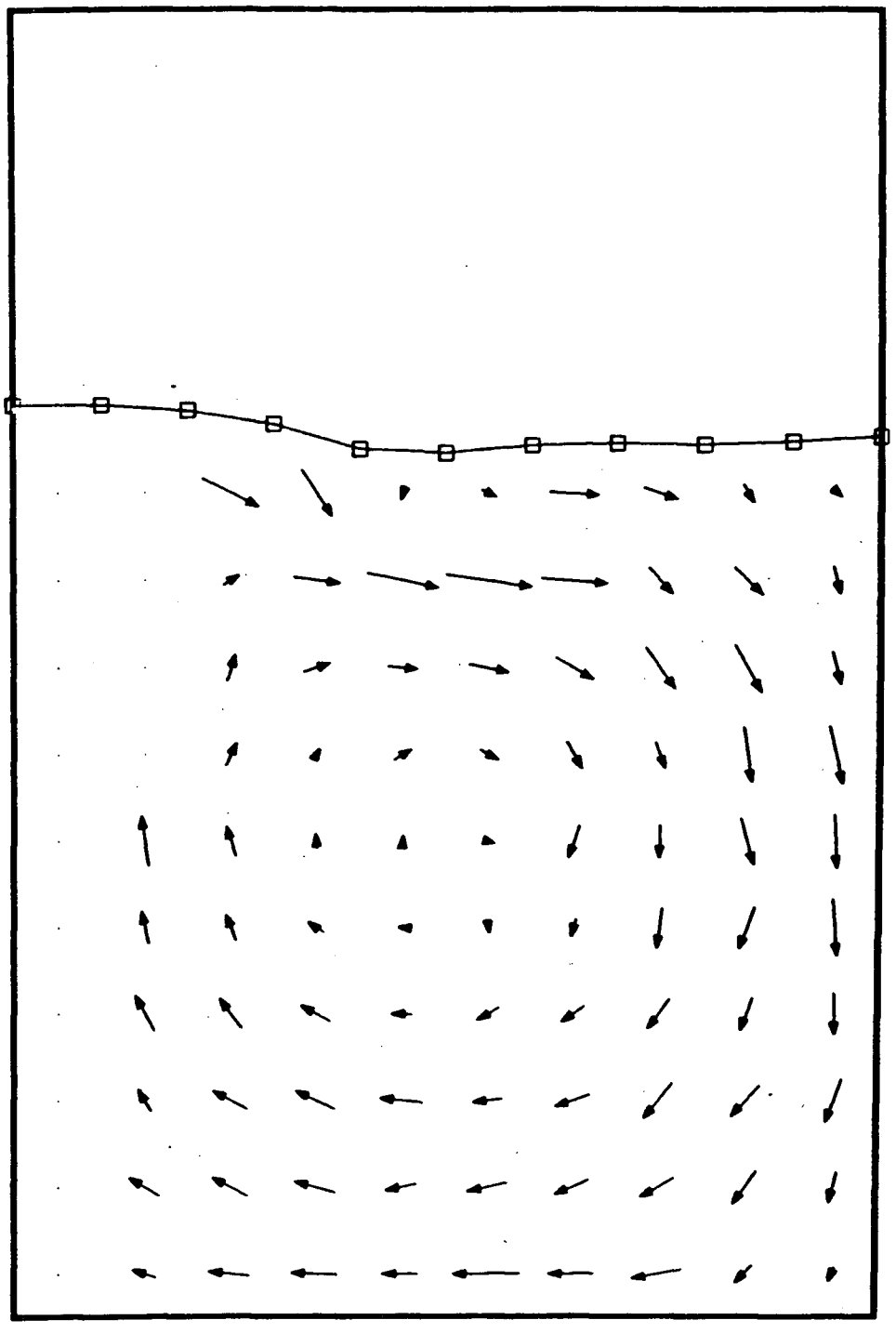

Figure 3.7. Experimental Velocity Vector and Surface Plot - Experiment 1.

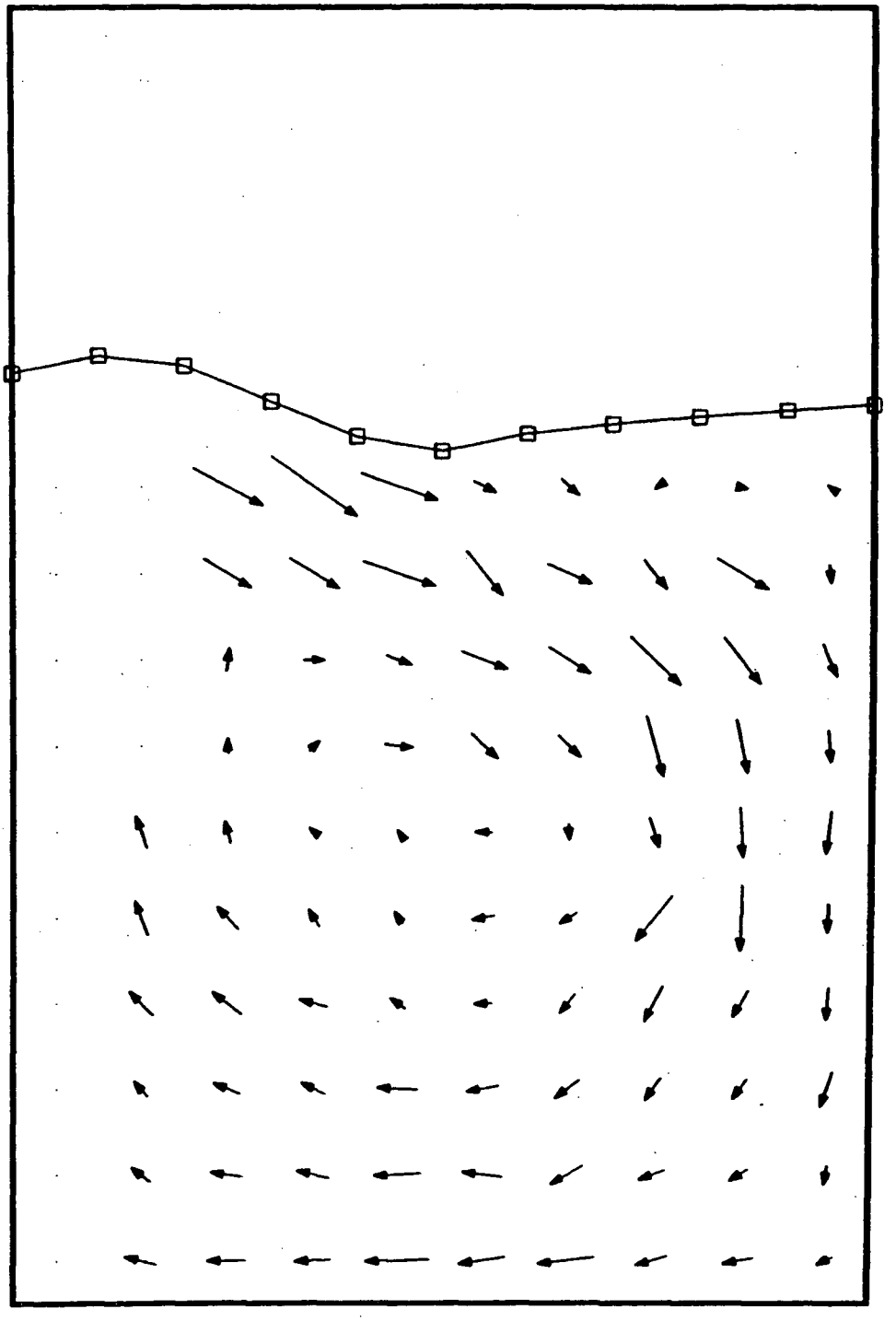

Figure 3.8. Experimental Velocity Vector and Surface Plot - Experiment 2.

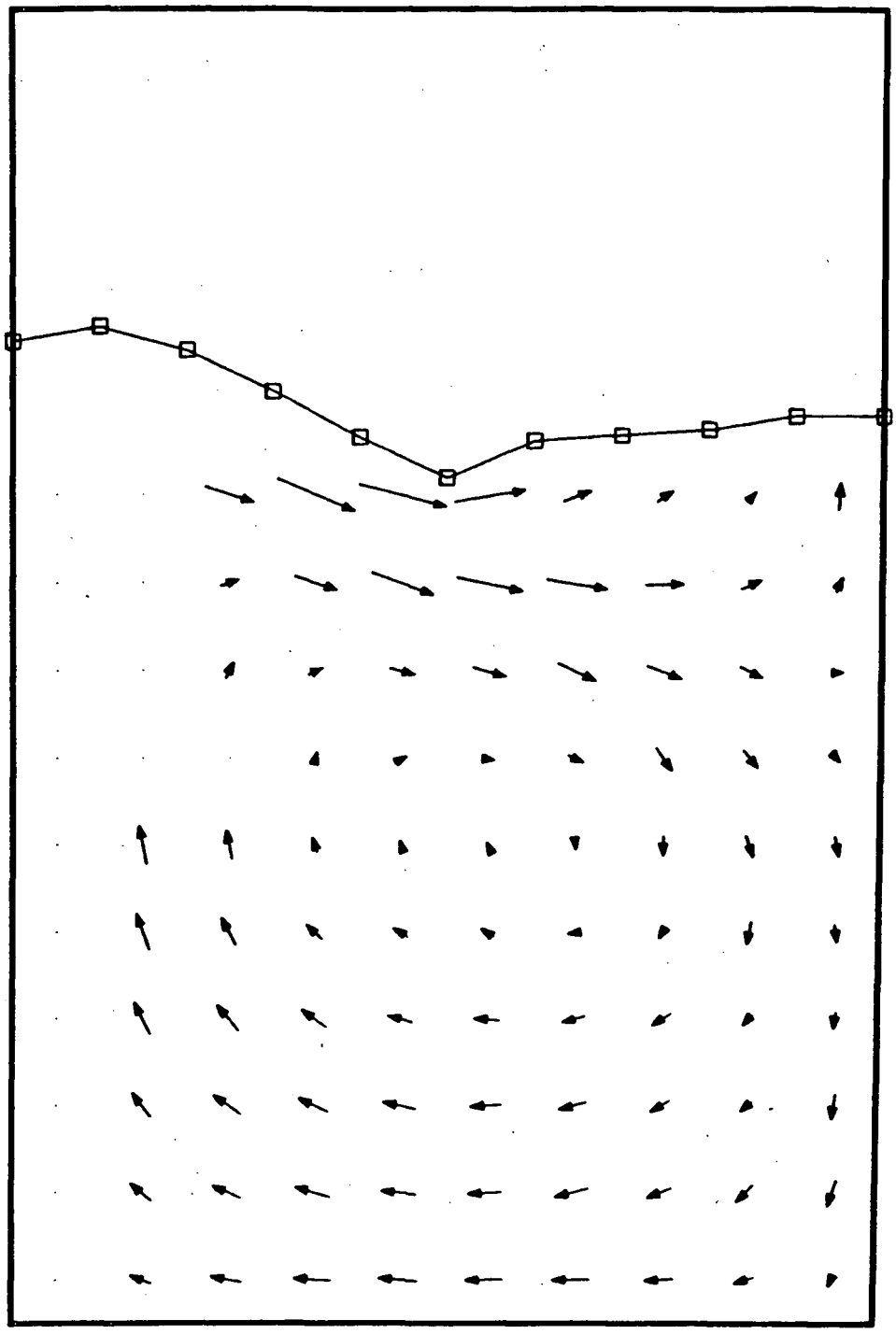

Figure 3.9. Experimental Velocity Vector and Surface Plot - Experiment 3.

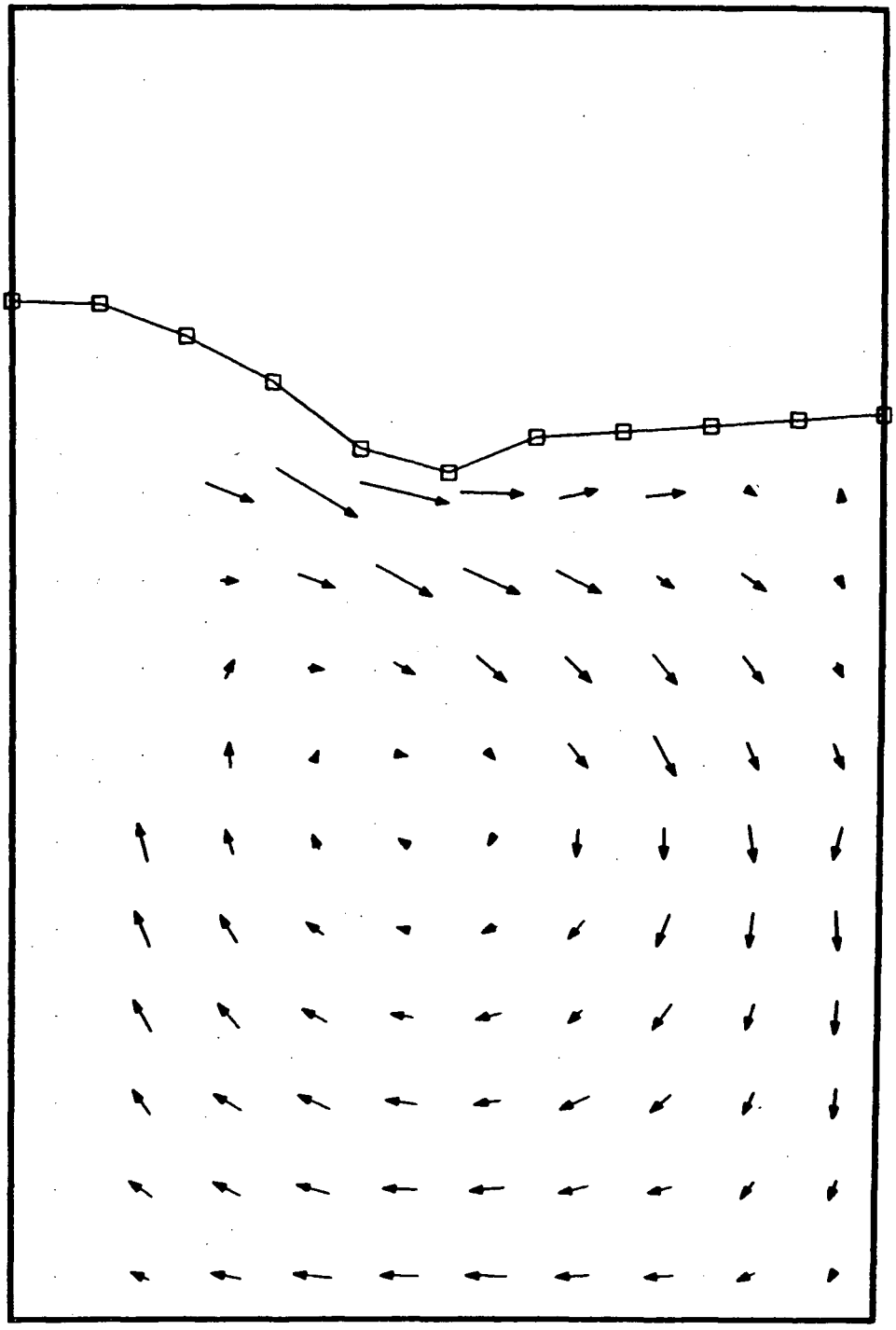

MAXIMUM VELOCITY (M/S) = 0.560

Figure 3.10. Experimental Velocity Vector and Surface Plot - Experiment 4.

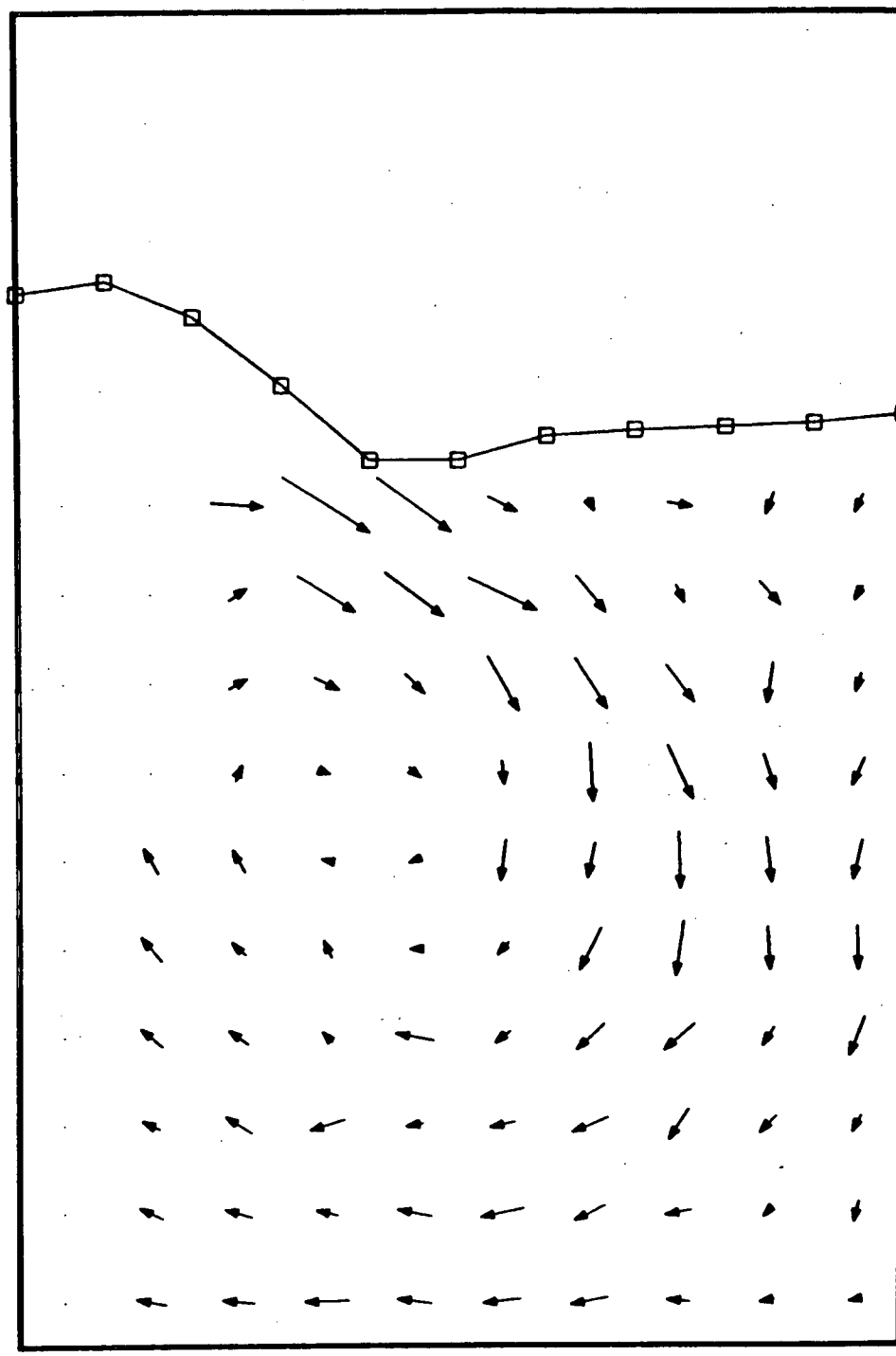

MAXIMUM VELOCITY (M/S) = 0.492

Figure 3.11. Experimental Velocity Vector and Surface Plot - Experiment 5.

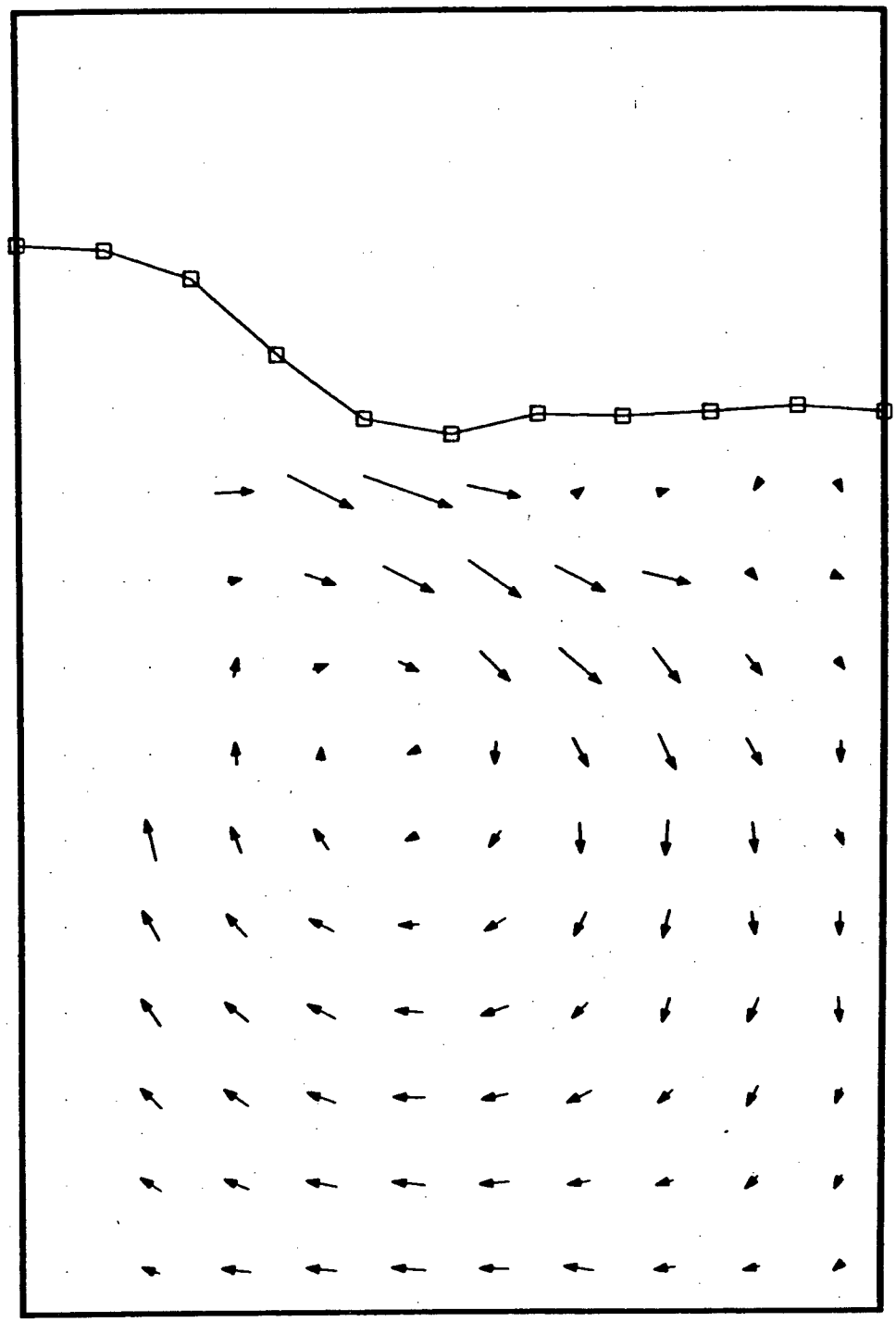

Figure 3.12. Experimental Velocity Vector and Surface Plot - Experiment 6.

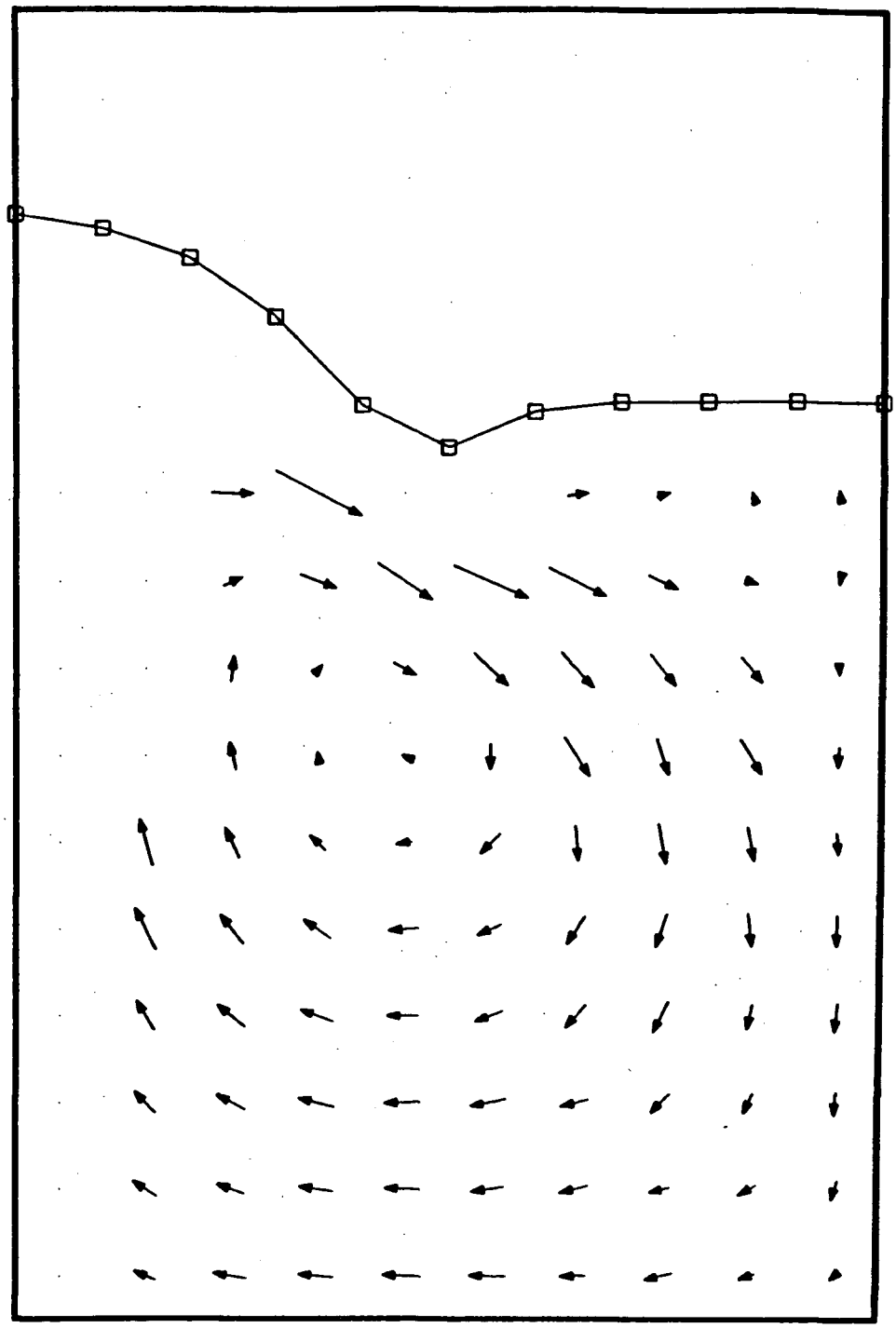

Figure 3.13. Experimental Velocity Vector and Surface Plot - Experiment 7.

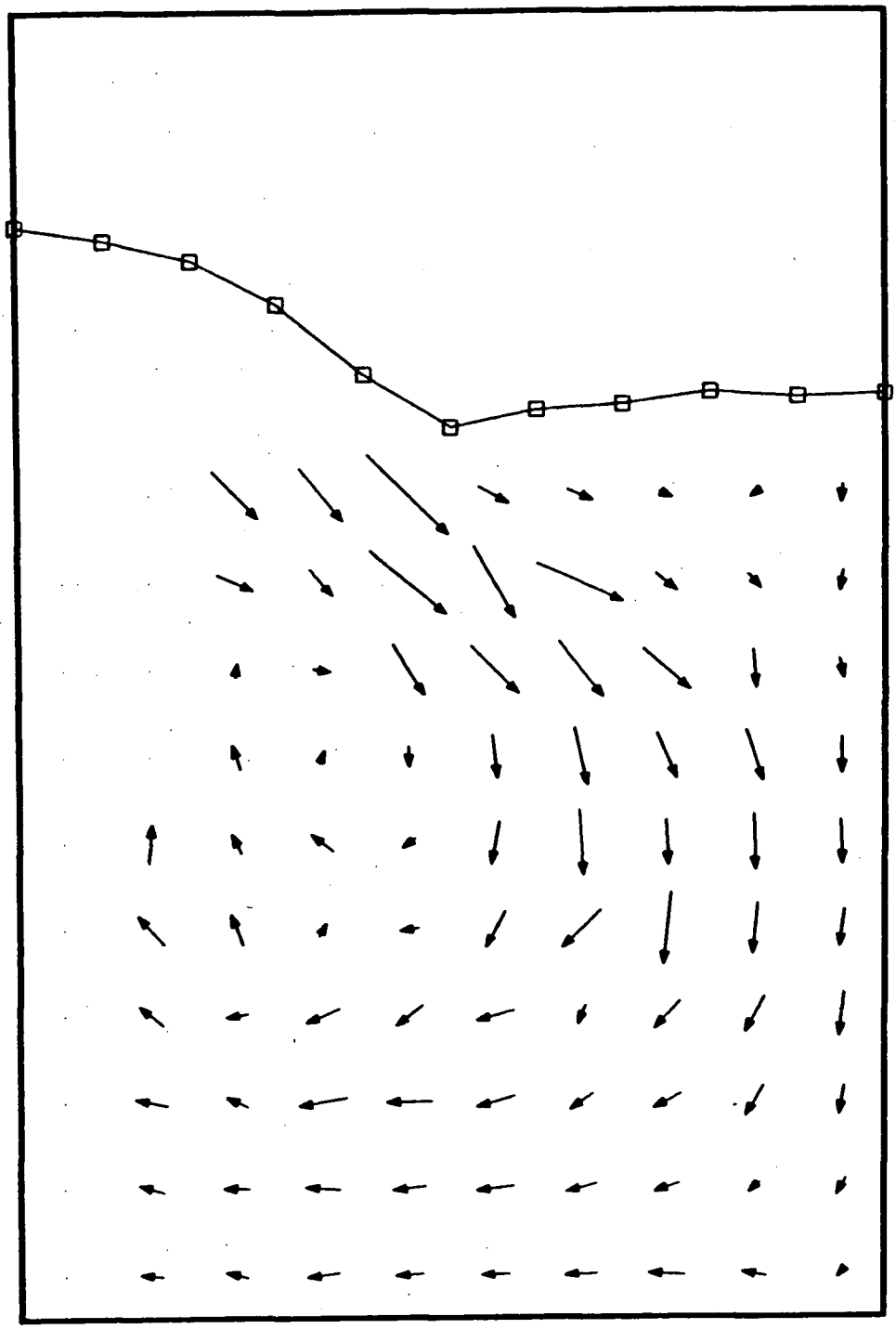

Figure 3.14. Experimental Velocity Vector and Surface Plot - Experiment 8.

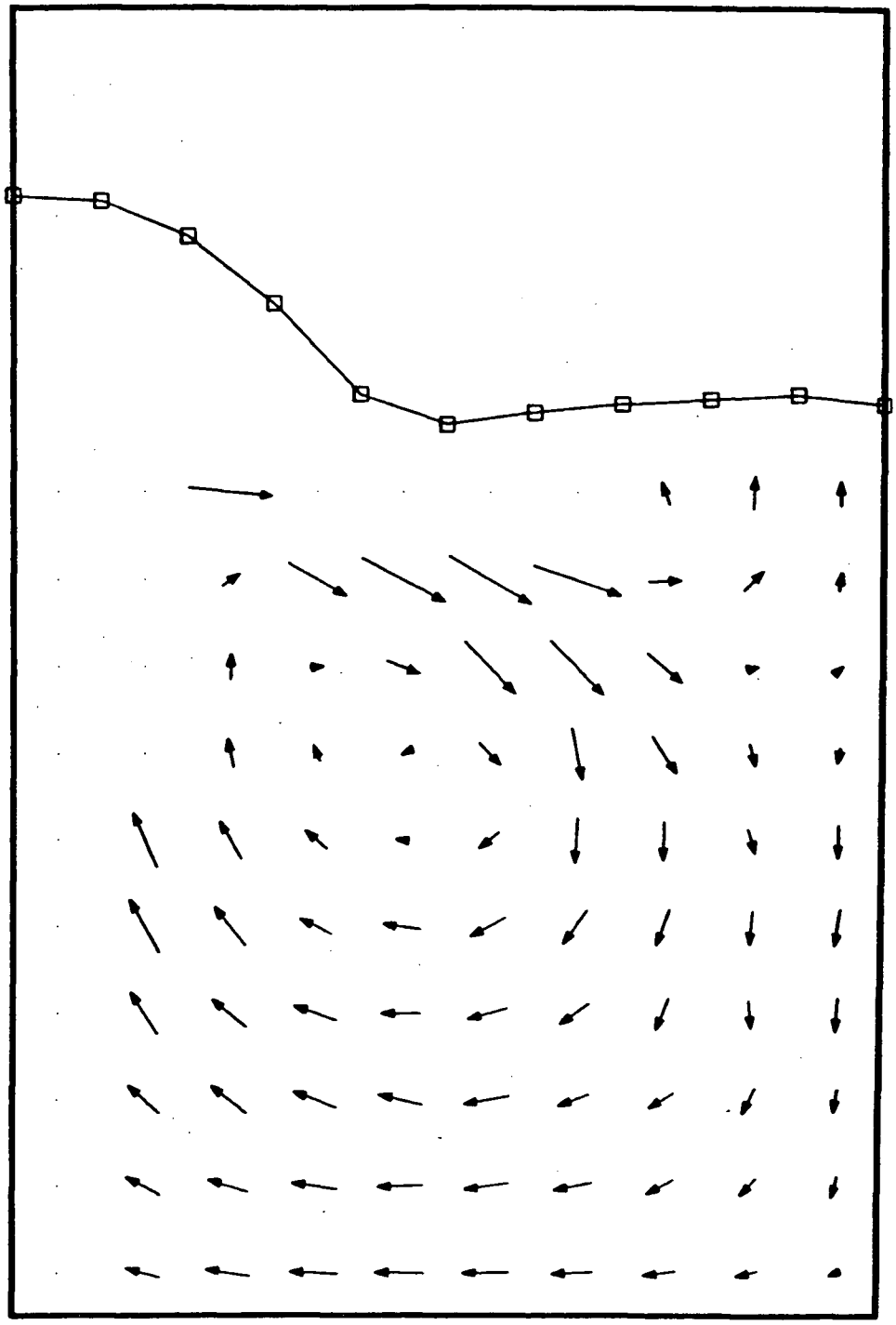

Figure 3.15. Experimental Velocity Vector and Surface Plot - Experiment 9.

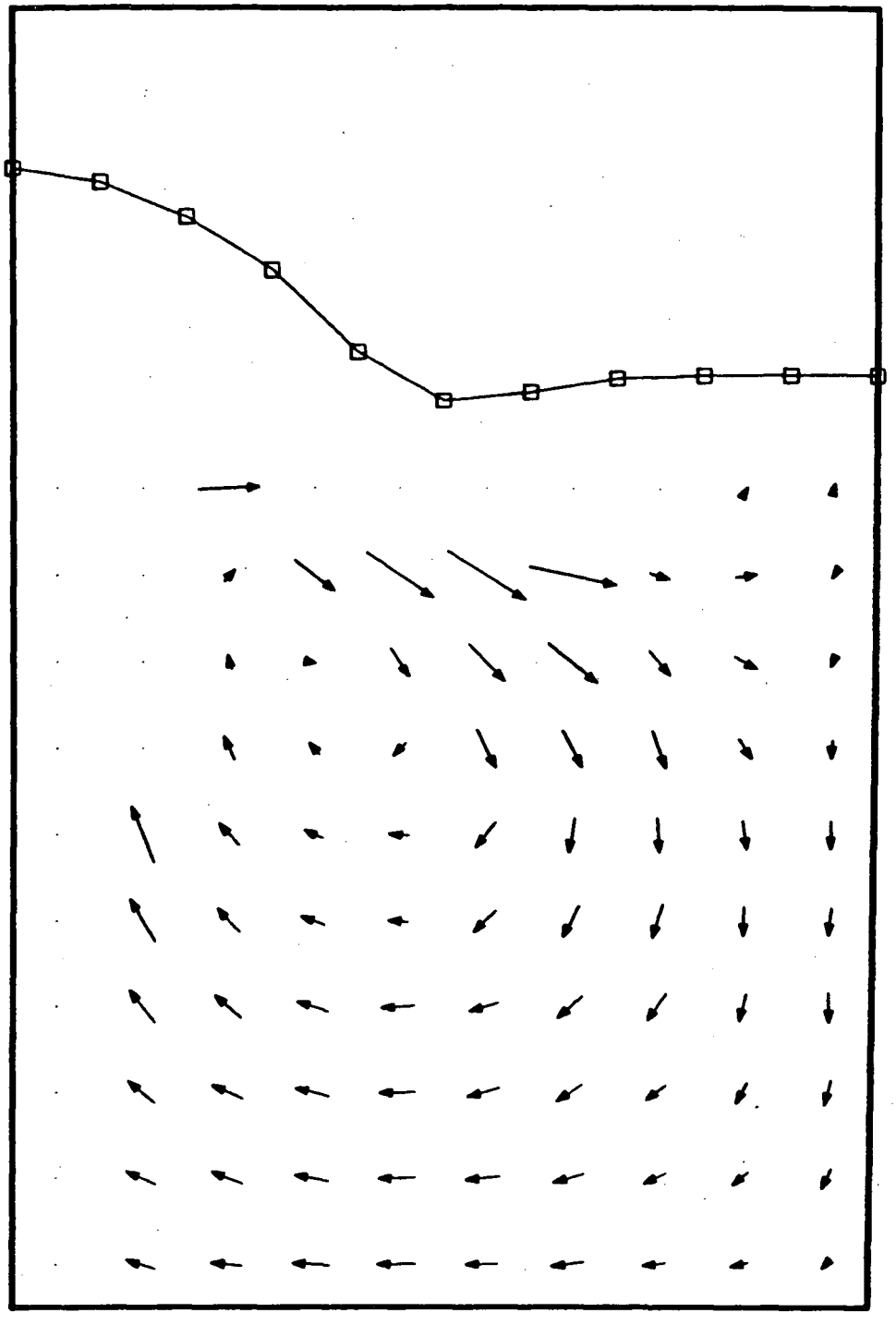

MAXIMUM VELOCITY (M/S) = 0.443

Figure 3.16. Experimental Velocity Vector and Surface Plot - Experiment 10.

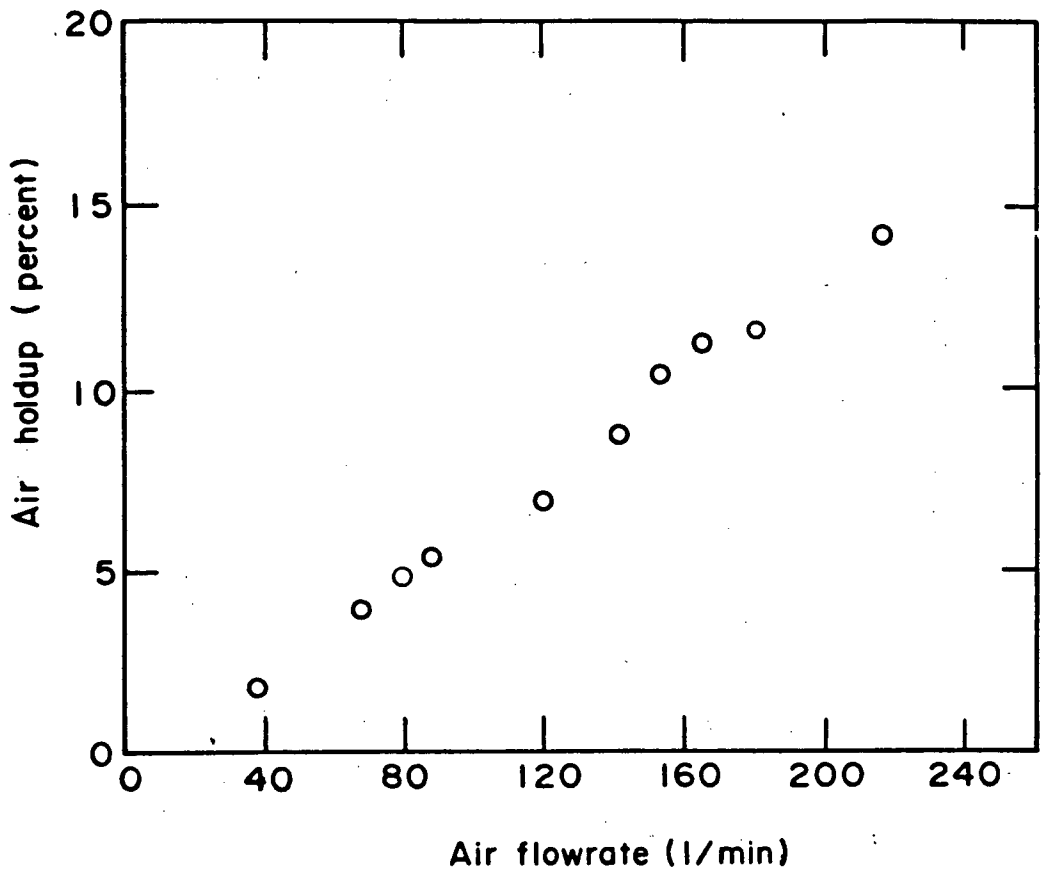

Figure 3.17. Variation of Air Holdup in Experimental Tank with Air Flowrate.

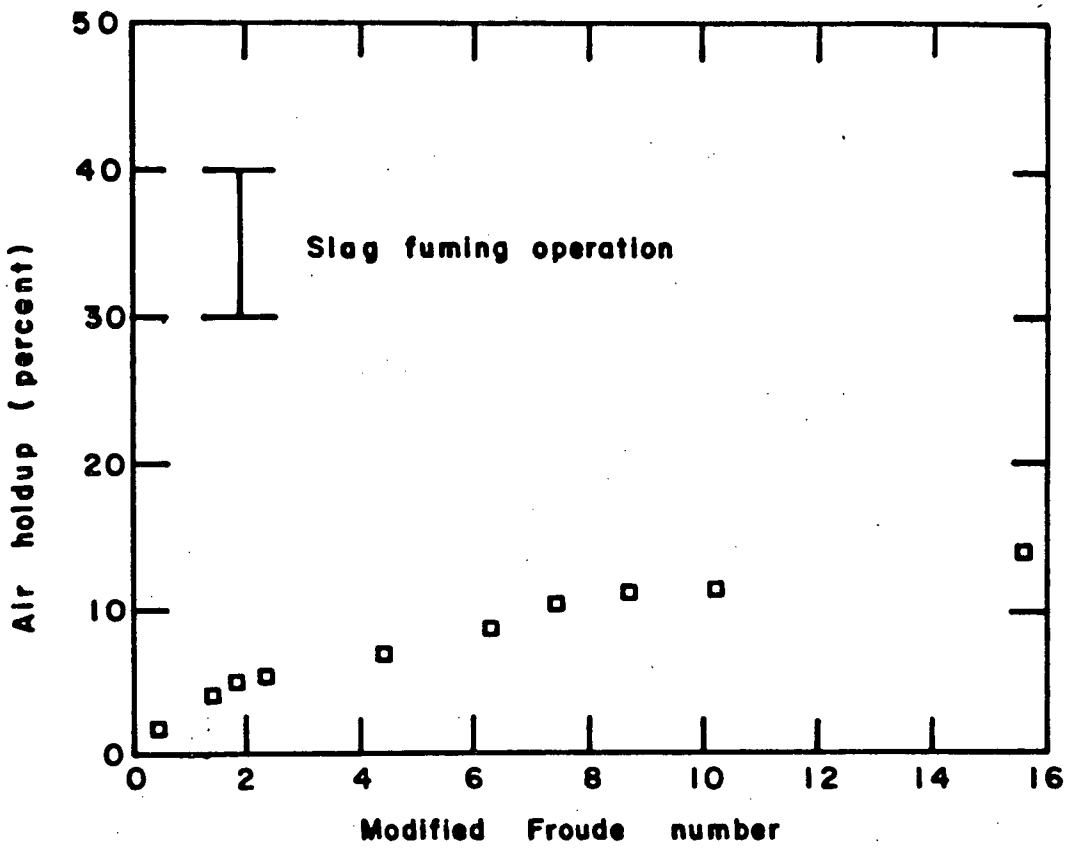

Figure 3.18. Variation of Air Holdup in Experimental Tank and Zinc Slag Fuming Furnace with Modified Froude Number.

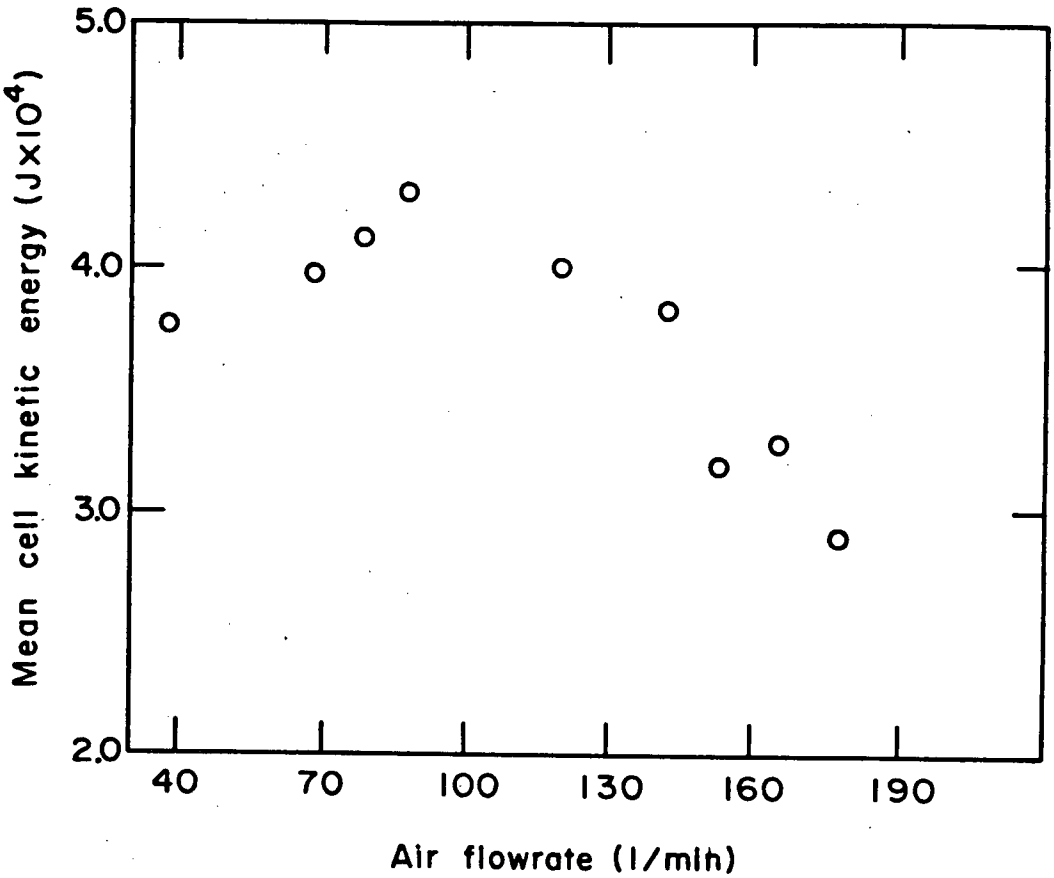

Figure 3.19. Mean Cell Kinetic Energy of Experimental Measurements as a Function of Air Flowrate.

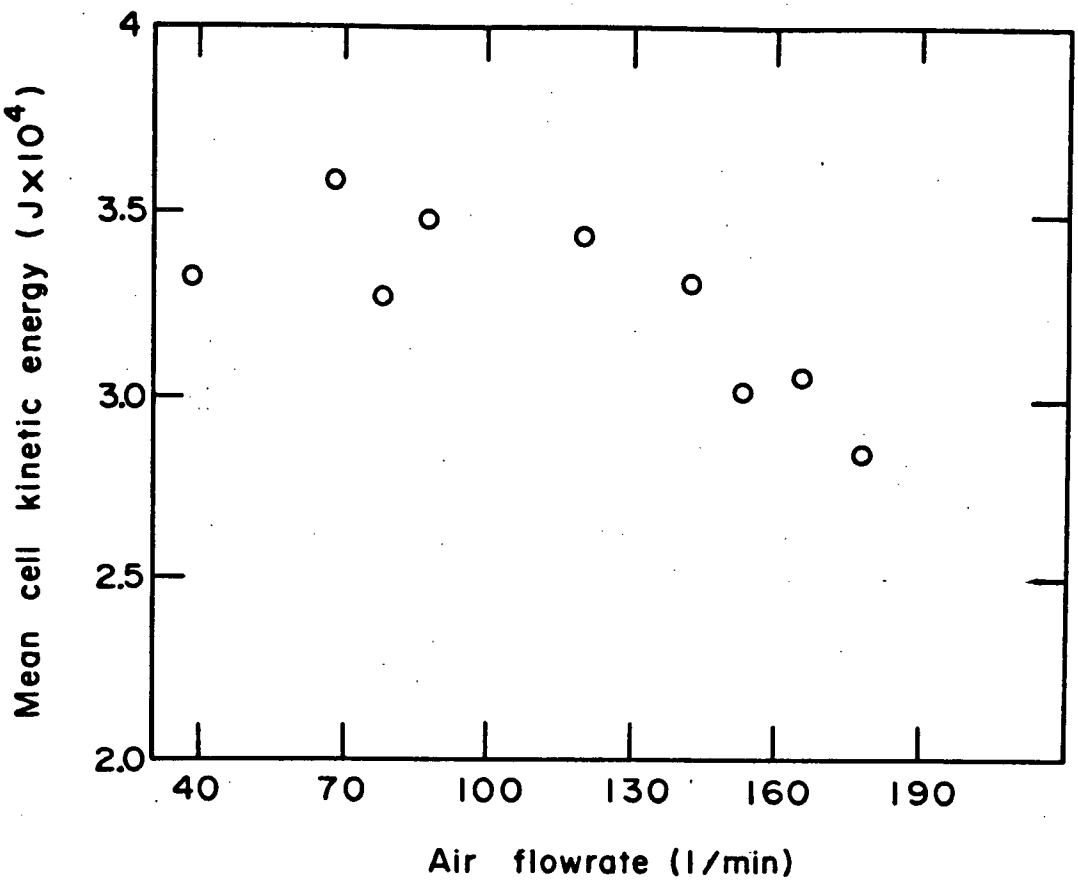

Figure 3.20. Mean Cell Kinetic Energy of Non-Surface Cells in Experimental Measurements as a function of Air Flowrate.

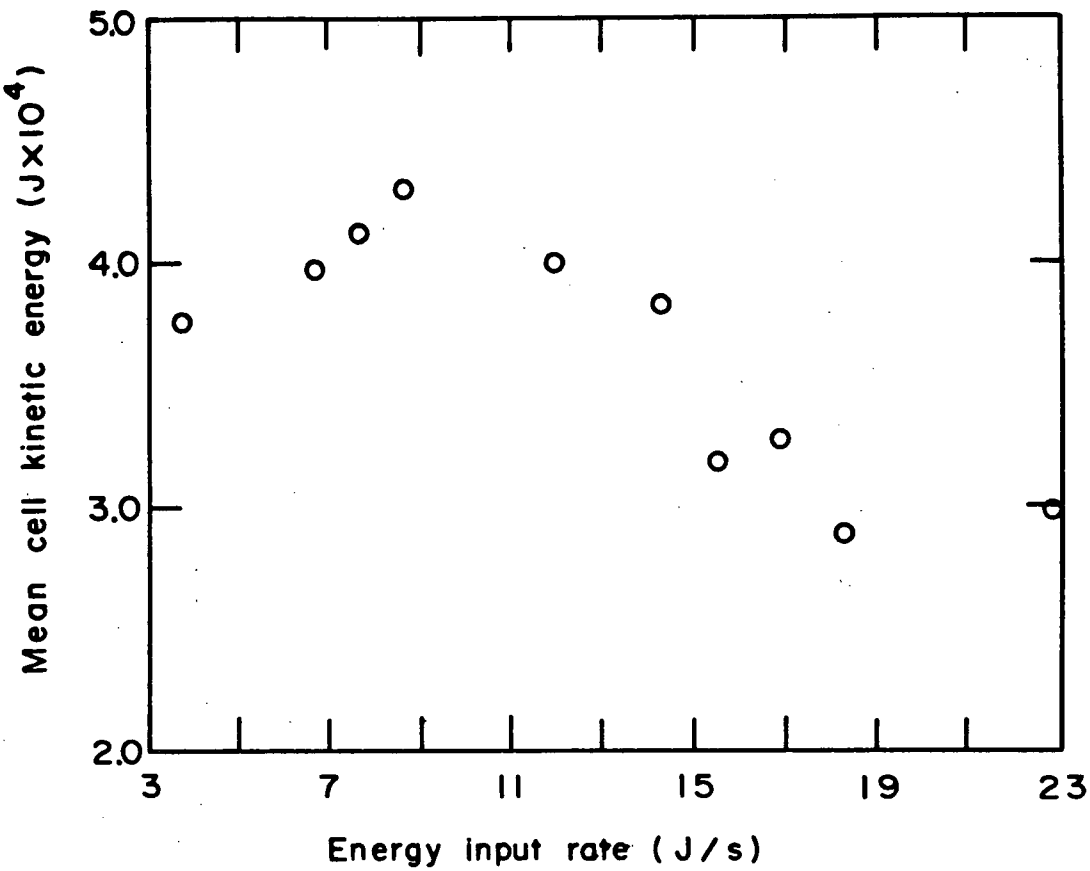

Figure 3.21. Variation of Experimental Mean Cell Kinetic Energy with Air Input Energy.

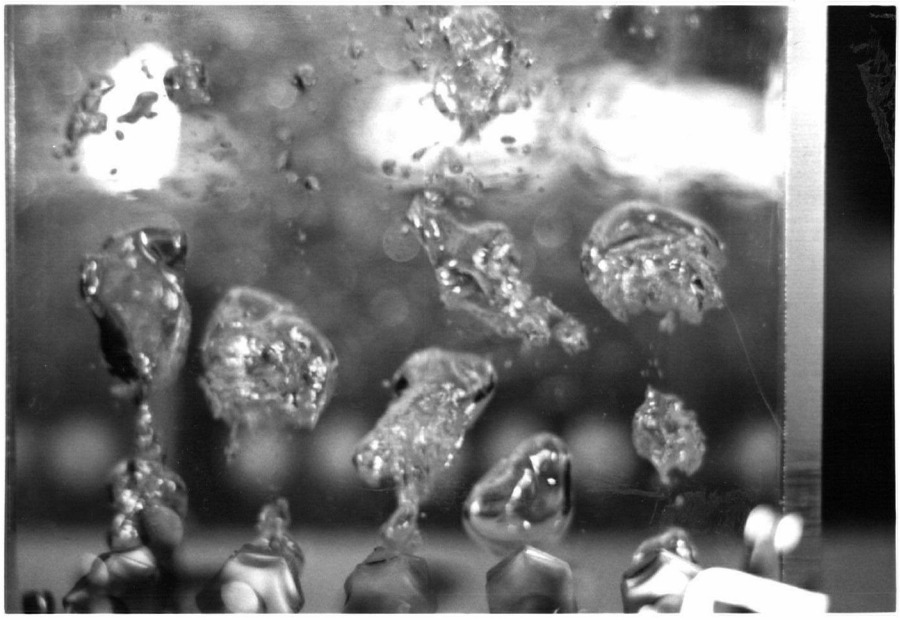

Figure 3.22. Bubble Formation at Tuyeres, $N_{Fr'}$ = 0.4.

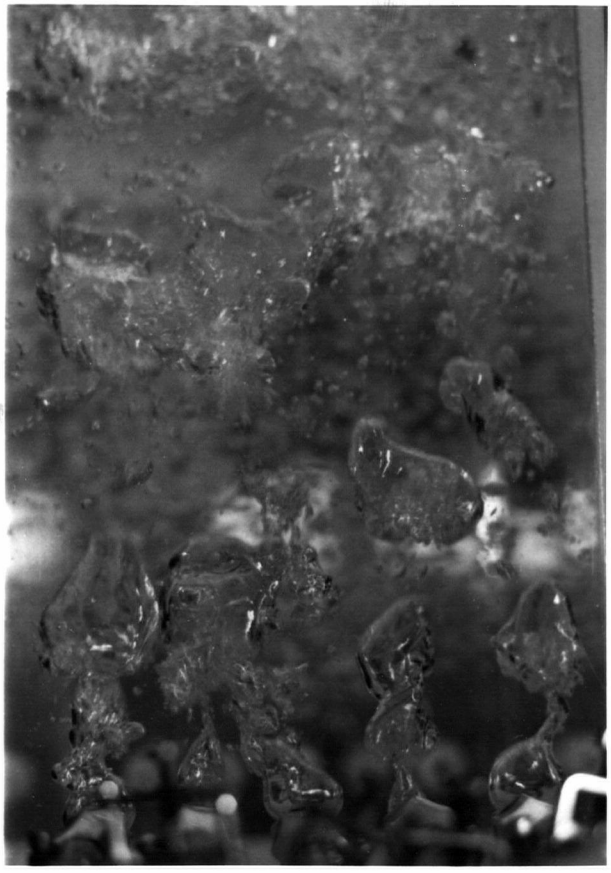

Figure 3.23. Bubble Formation at Tuyeres, $N_{Fr'}$ = 2.3.

Figure 3.24. Bubble Formation at Tuyeres, $N_{Fr'}$ = 15.6.

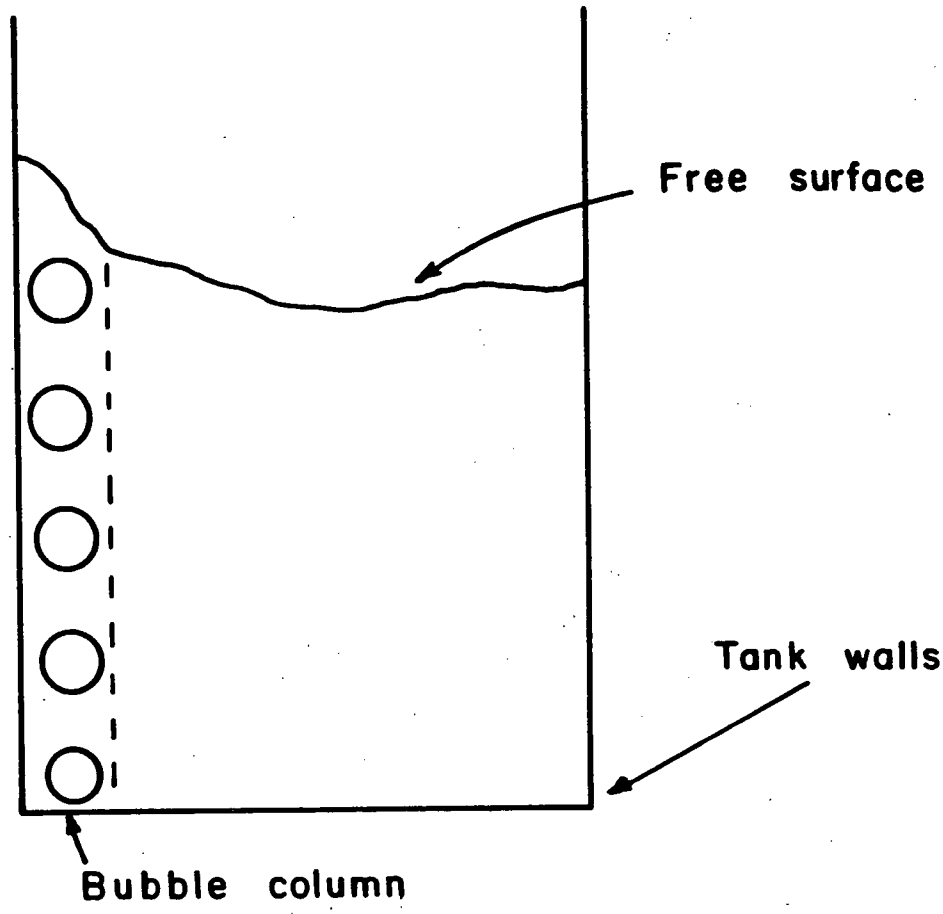

Figure 4.1. Schematic Description of Boundary Conditions Necessary to Describe the Flow in the Experimental Tank.

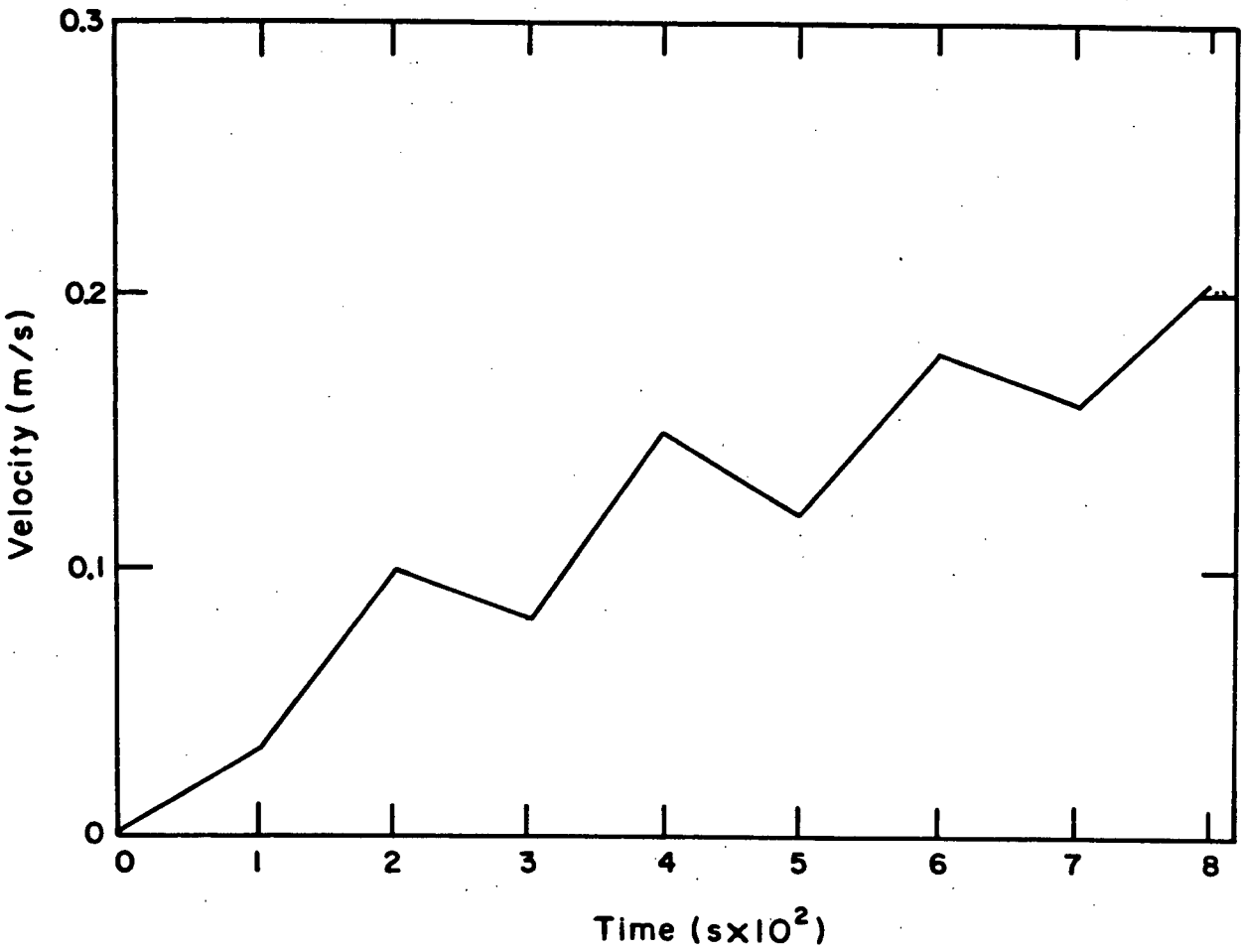

Figure 4.2. Velocity Fluctuations in a Finite-Difference Cell Computed by SOLASMAC Method.

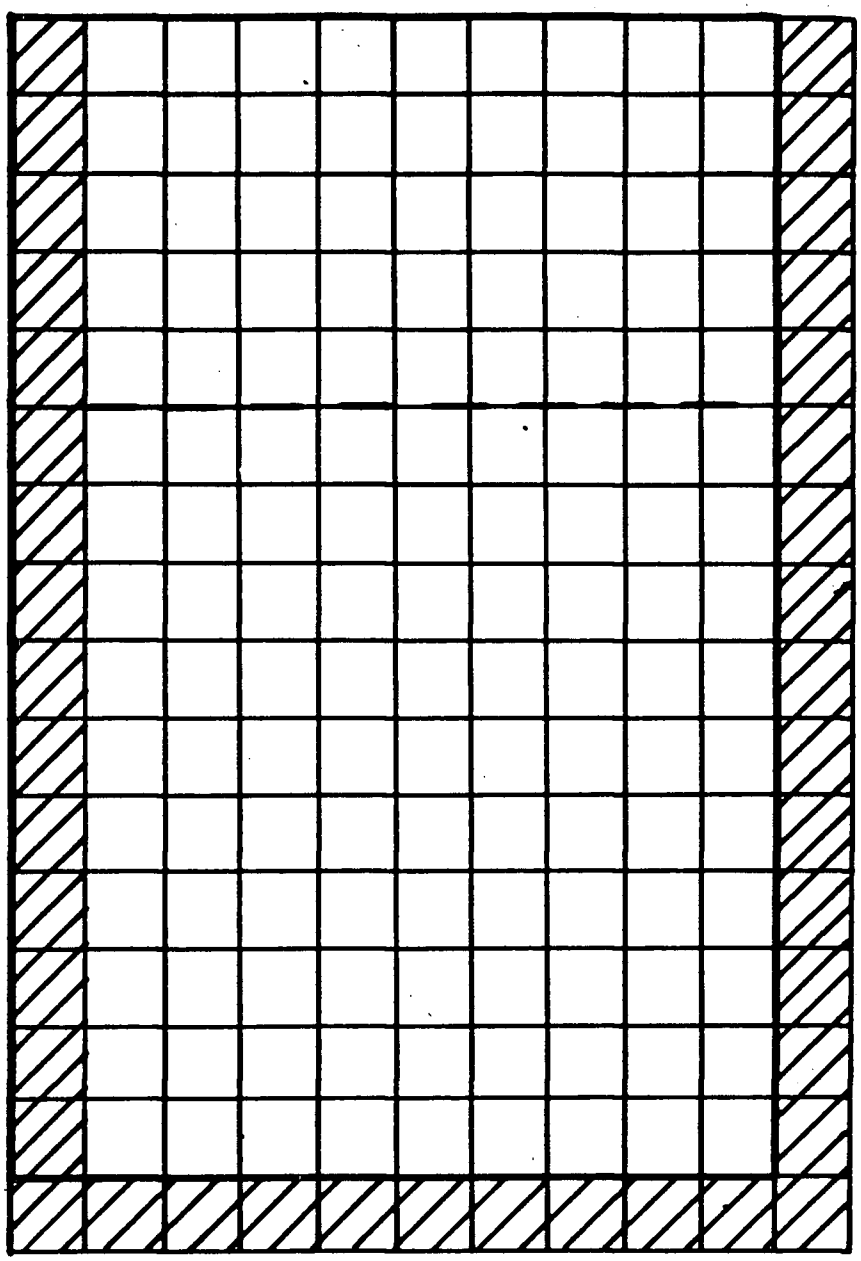

Figure 4.3. Finite Difference Grid Used to Compute Flow in Experimental Tank.

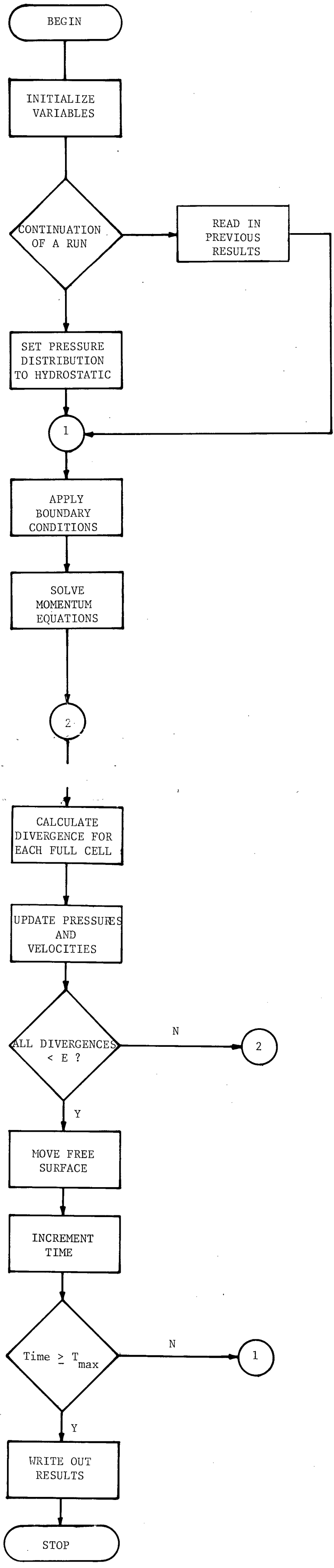

Figure 4.4. Flowchart of the SSMCR Program.

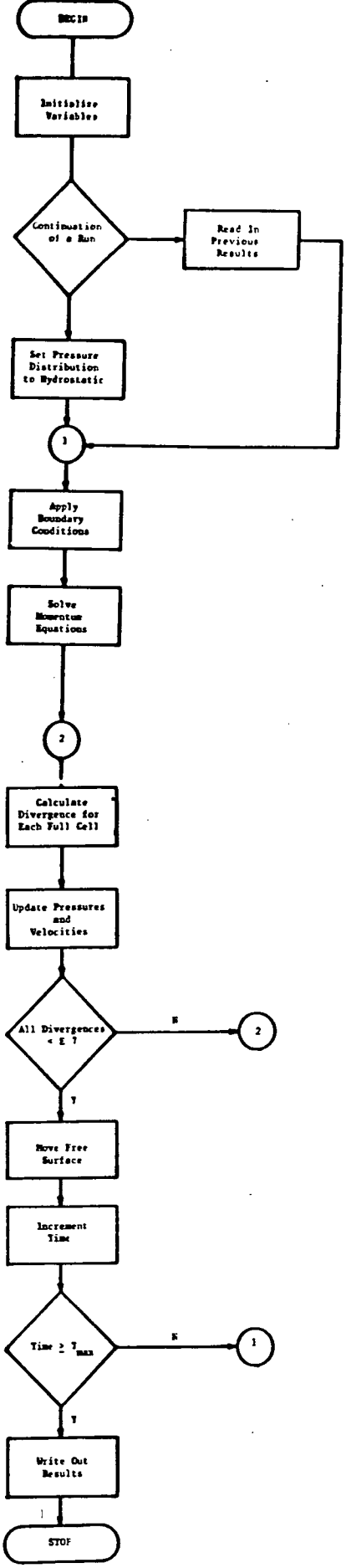

Figure 4.4. Flowchart of the SSMCR Program.

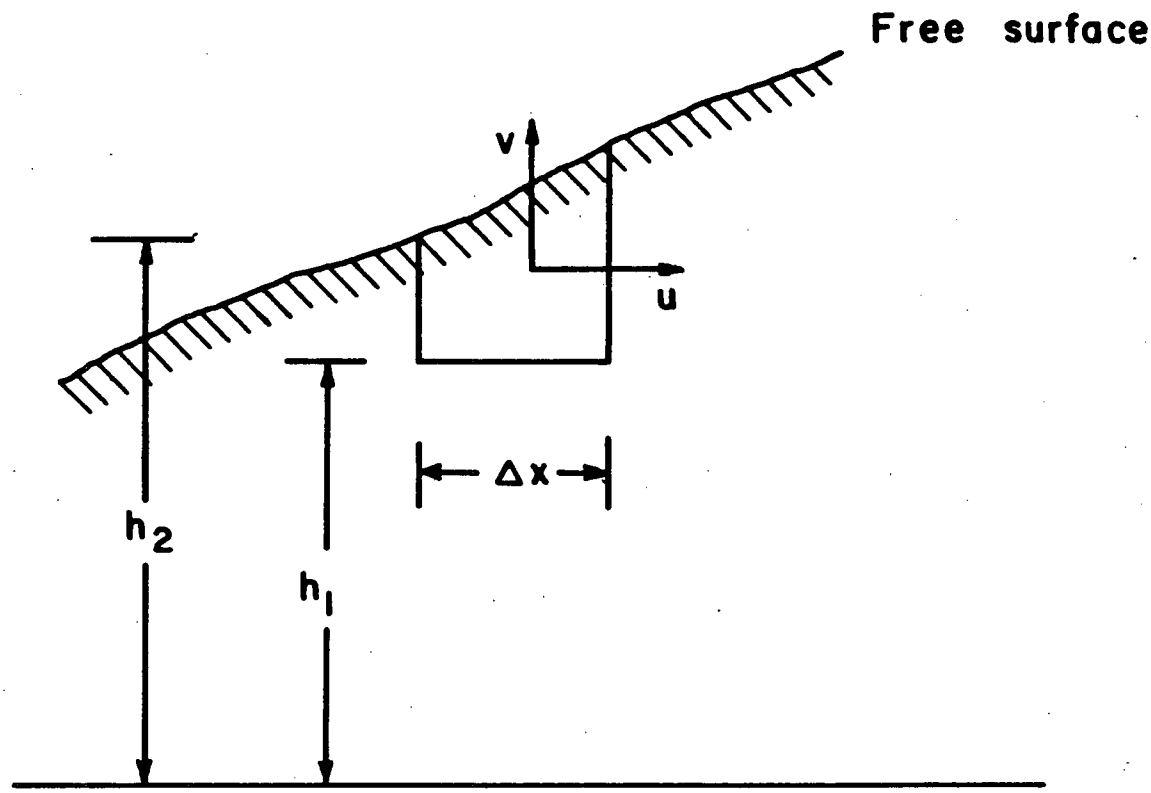

Figure 4.5. Diagram of Free Surface Location and Movement Technique as used in SSMCR.

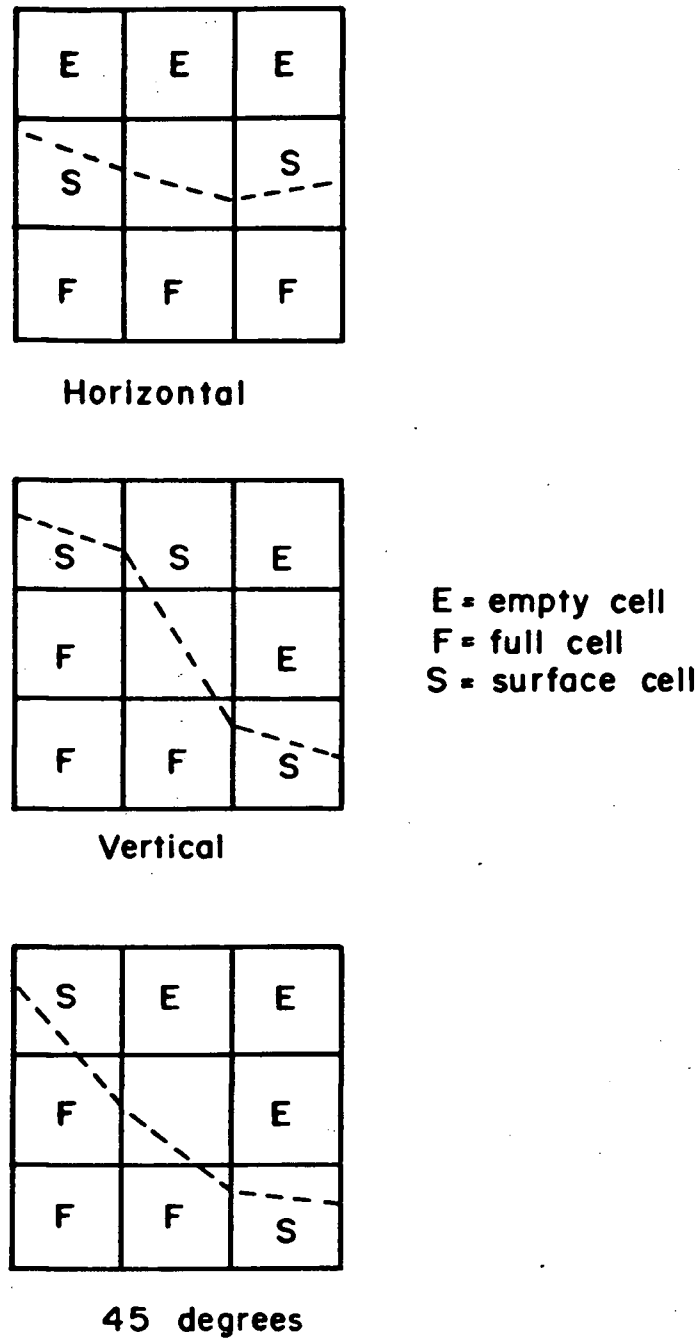

Figure 4.6. Recognition of Surface Orientation for Tangential Stress Condition.

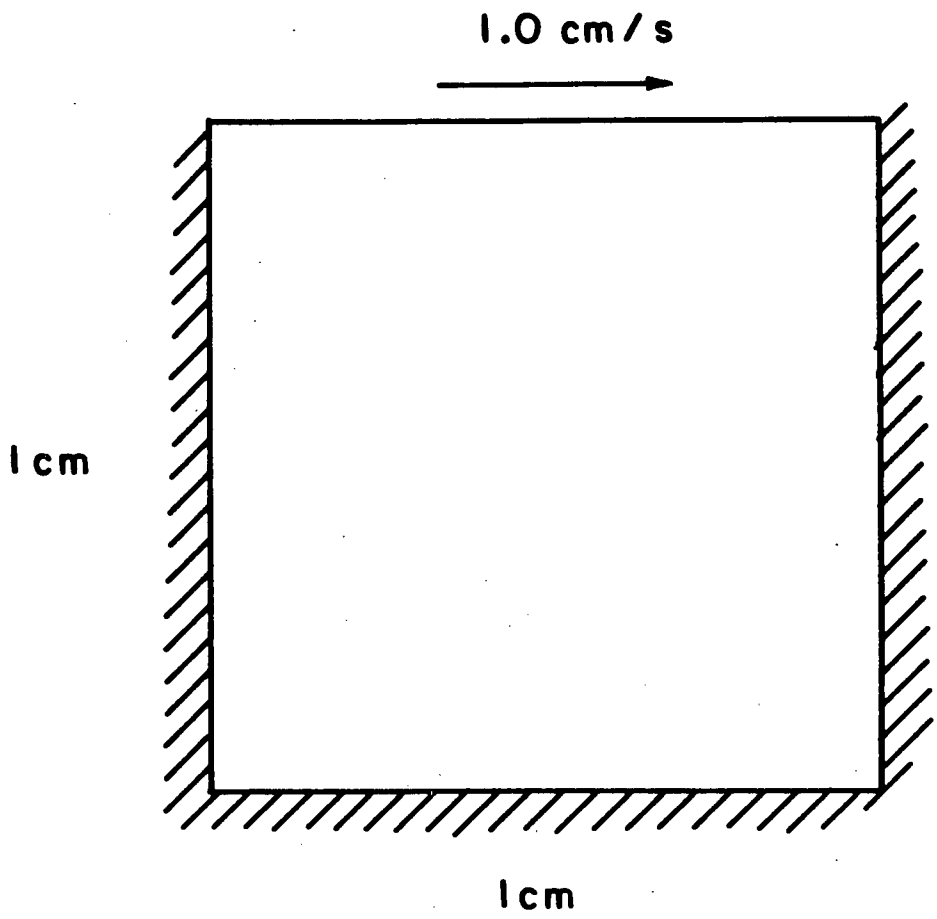

Figure 5.1. Diagram of Problem used to Test SSMCR.

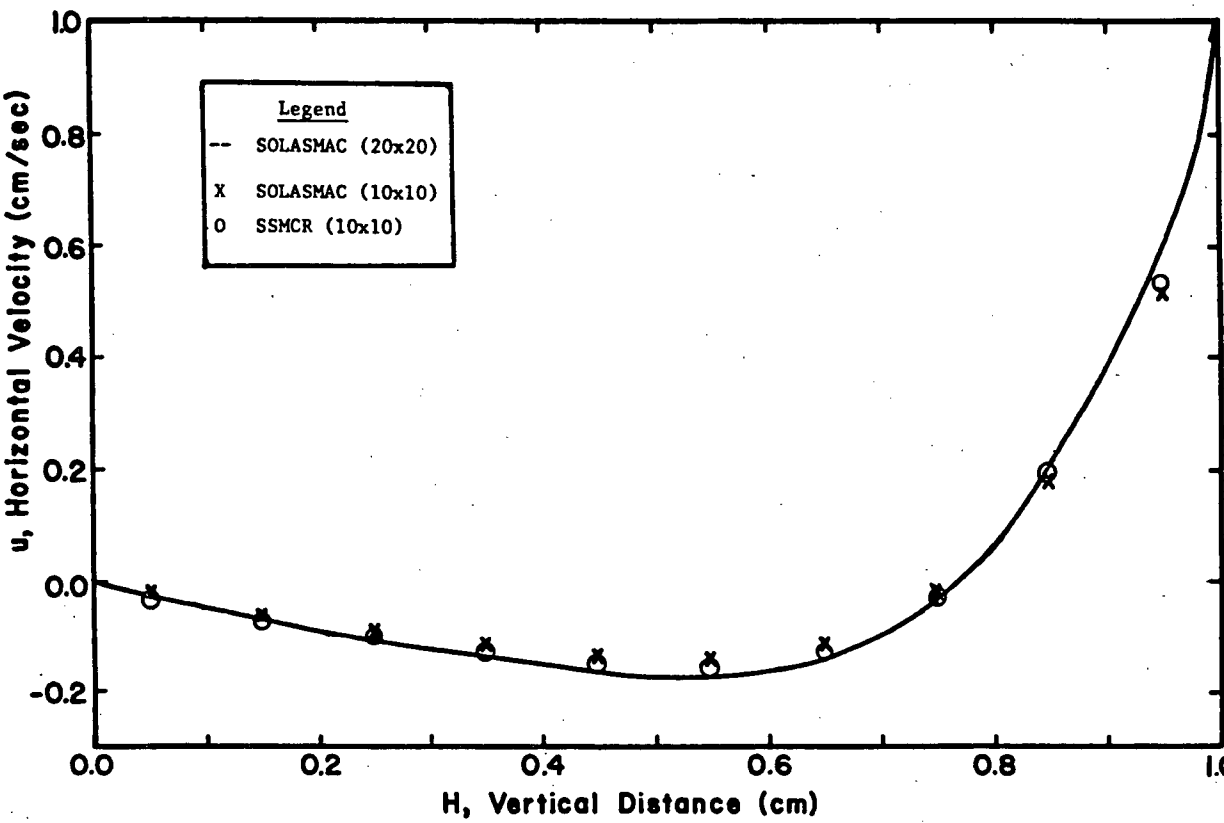

Figure 5.2. Agreement Between Predictions Made by SSMCR and SOLASMAC for Flow in a Square Cavity.

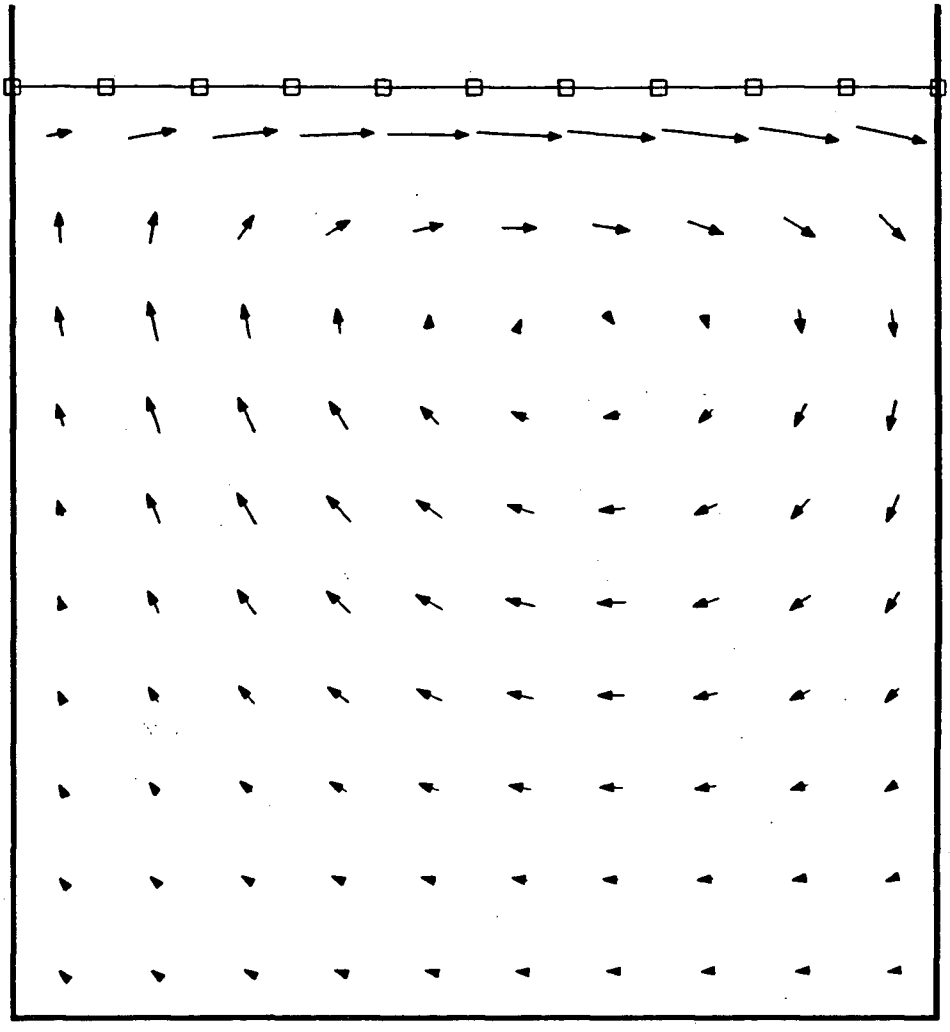

MAXIMUM VELOCITY (M/S) = 0.600

Figure 5.3. Erroneous Prediction of Square Cavity Flow.

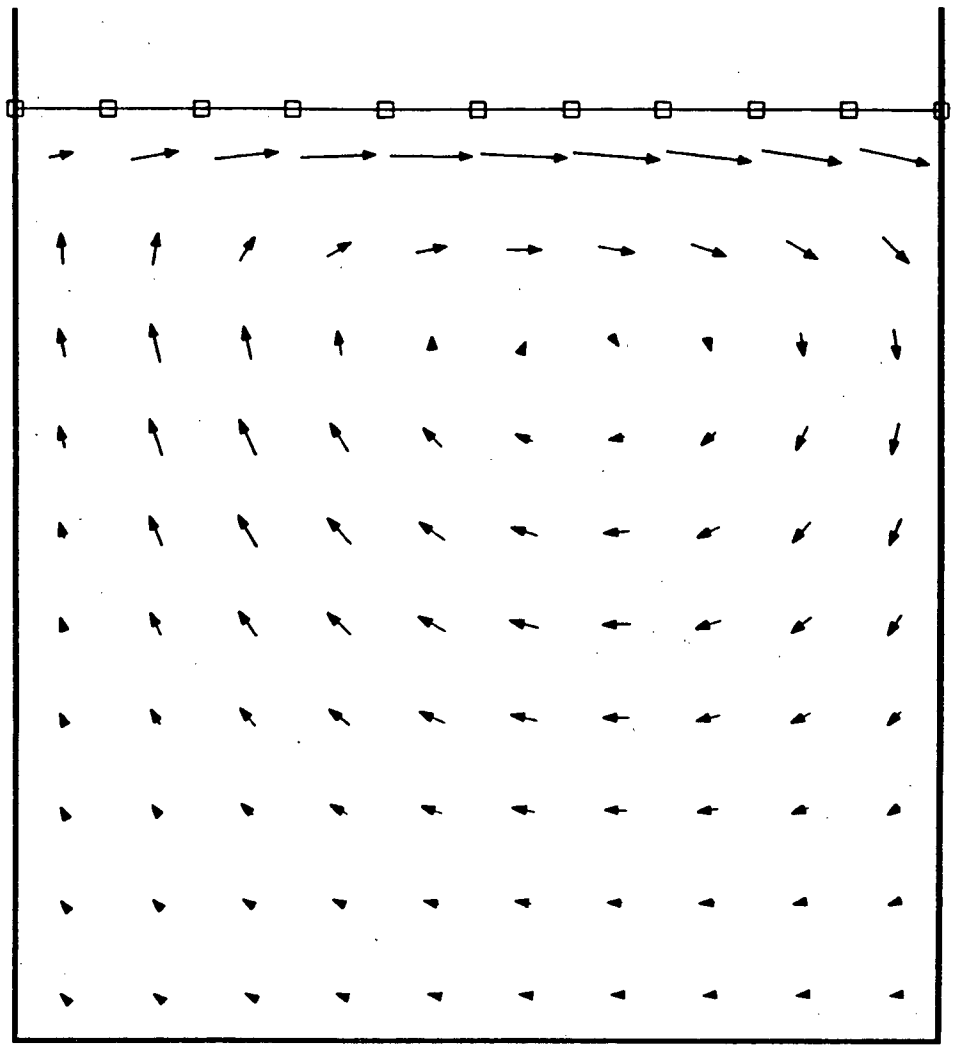

MAXIMUM VELOCITY (M/S) = 0.600

Figure 5.4. Correct Prediction of Square Cavity Flow.

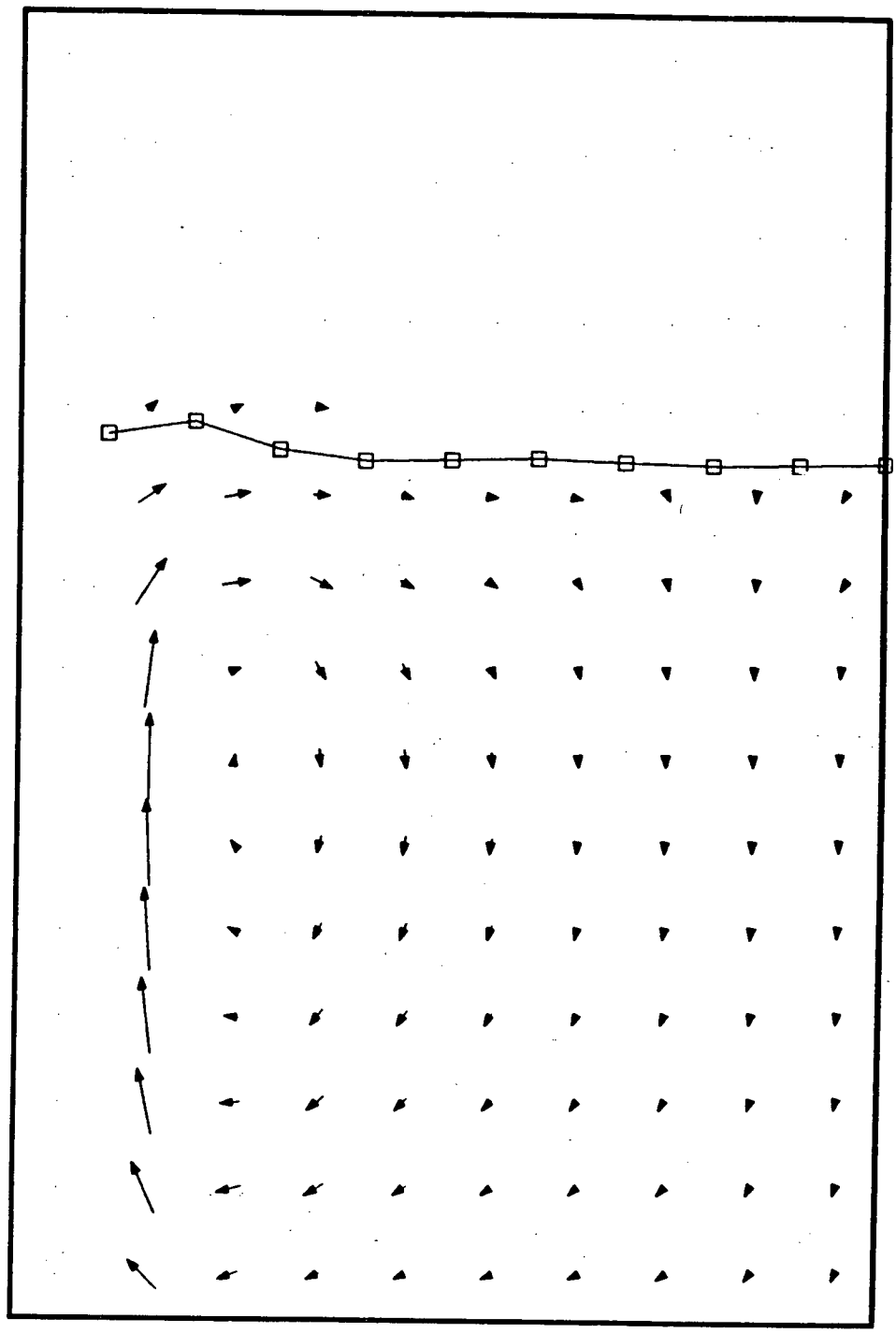

Figure 5.5. Prediction of Experimental Flow Regime Made by Constant Velocity Condition, μ_{eff} = 10 g/cm•s.

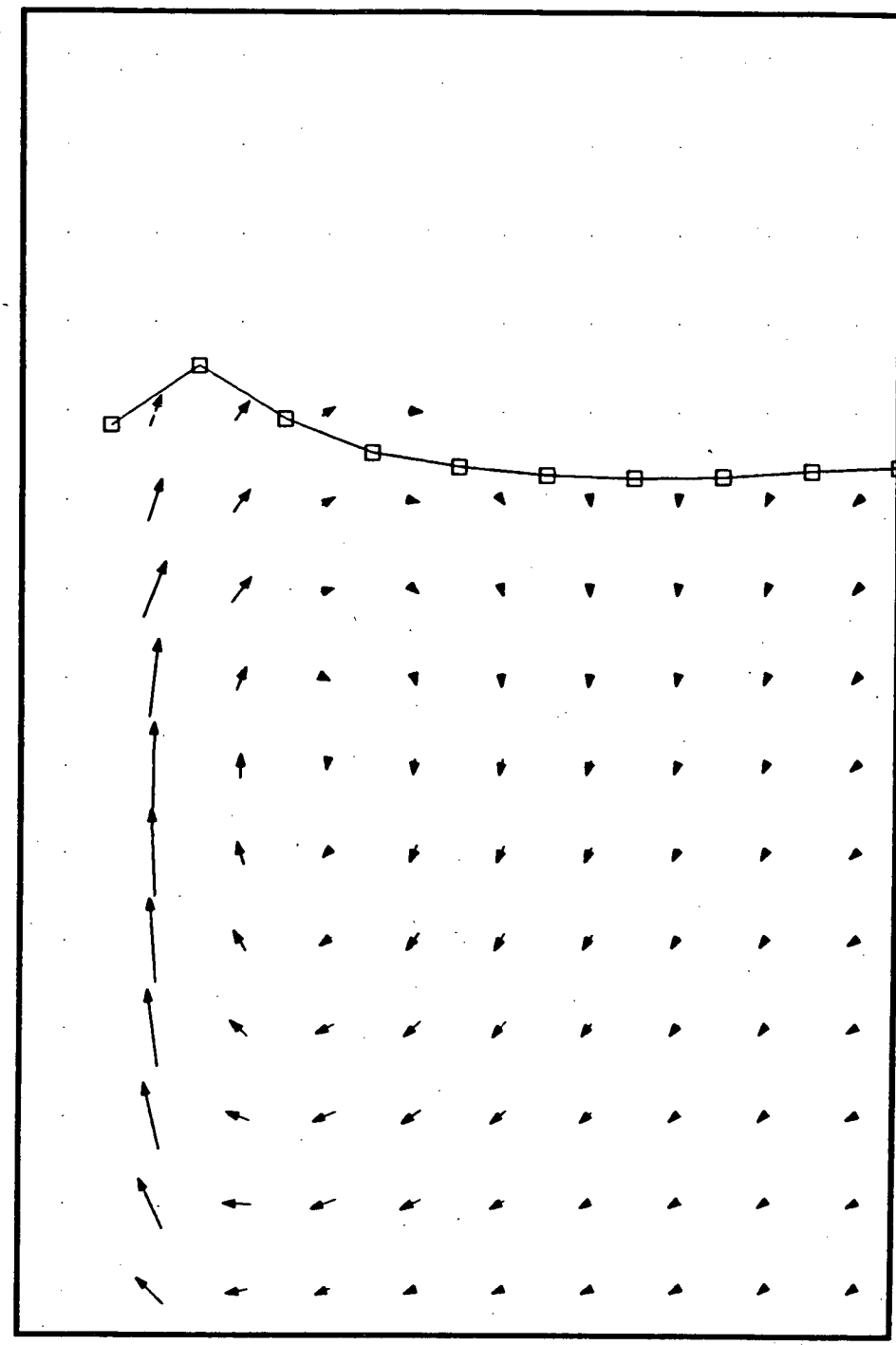

Figure 5.6. Prediction of Experimental Flow Regime Made by Constant Velocity Condition, μ_{eff} = 40 g/cm•s.

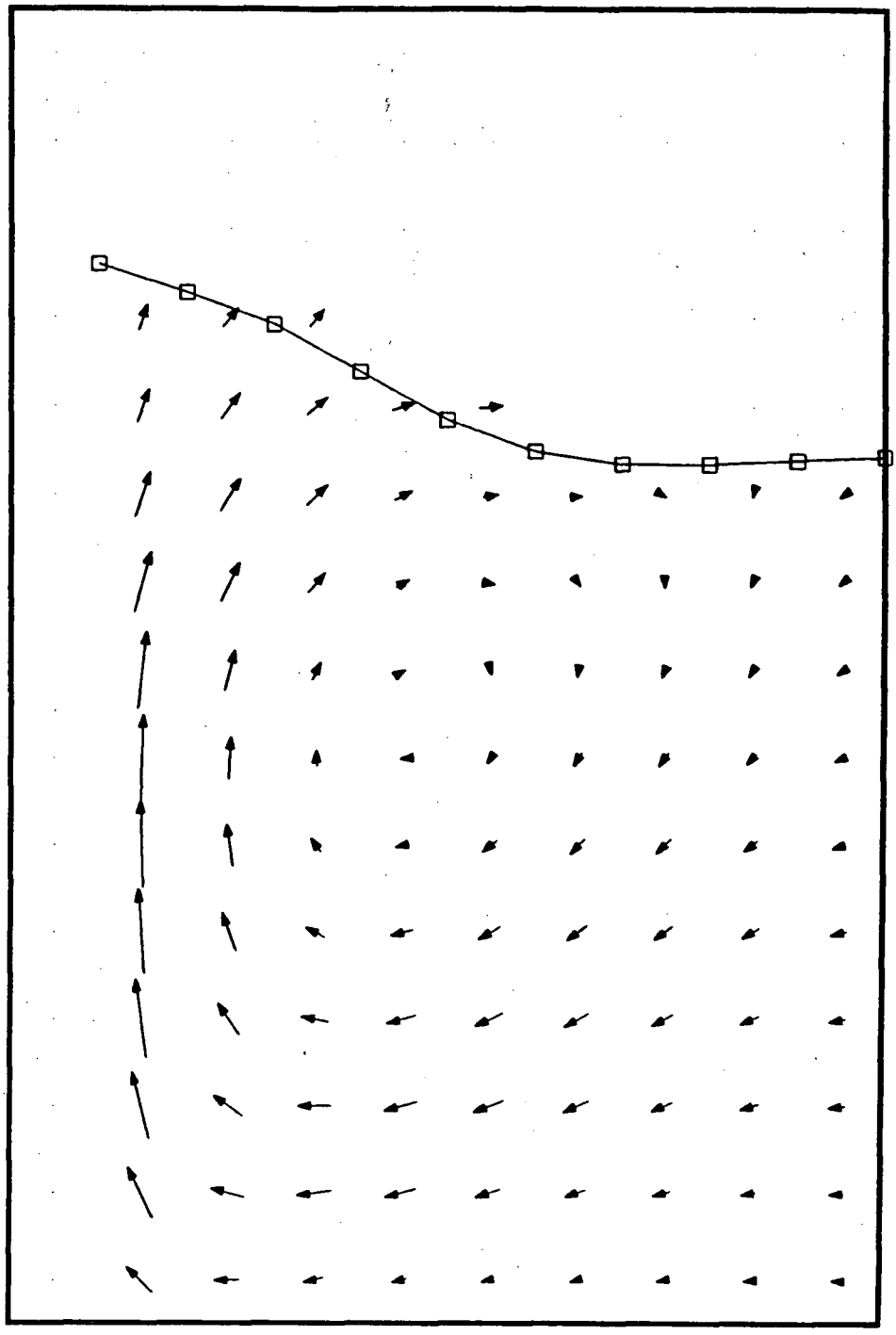

MAXIMUM VELOCITY (M/S) = 0.586

Figure 5.7. Prediction of Experimental Flow Regime Made by Constant Velocity Condition, μ_{eff} = 400 g/cm·s.

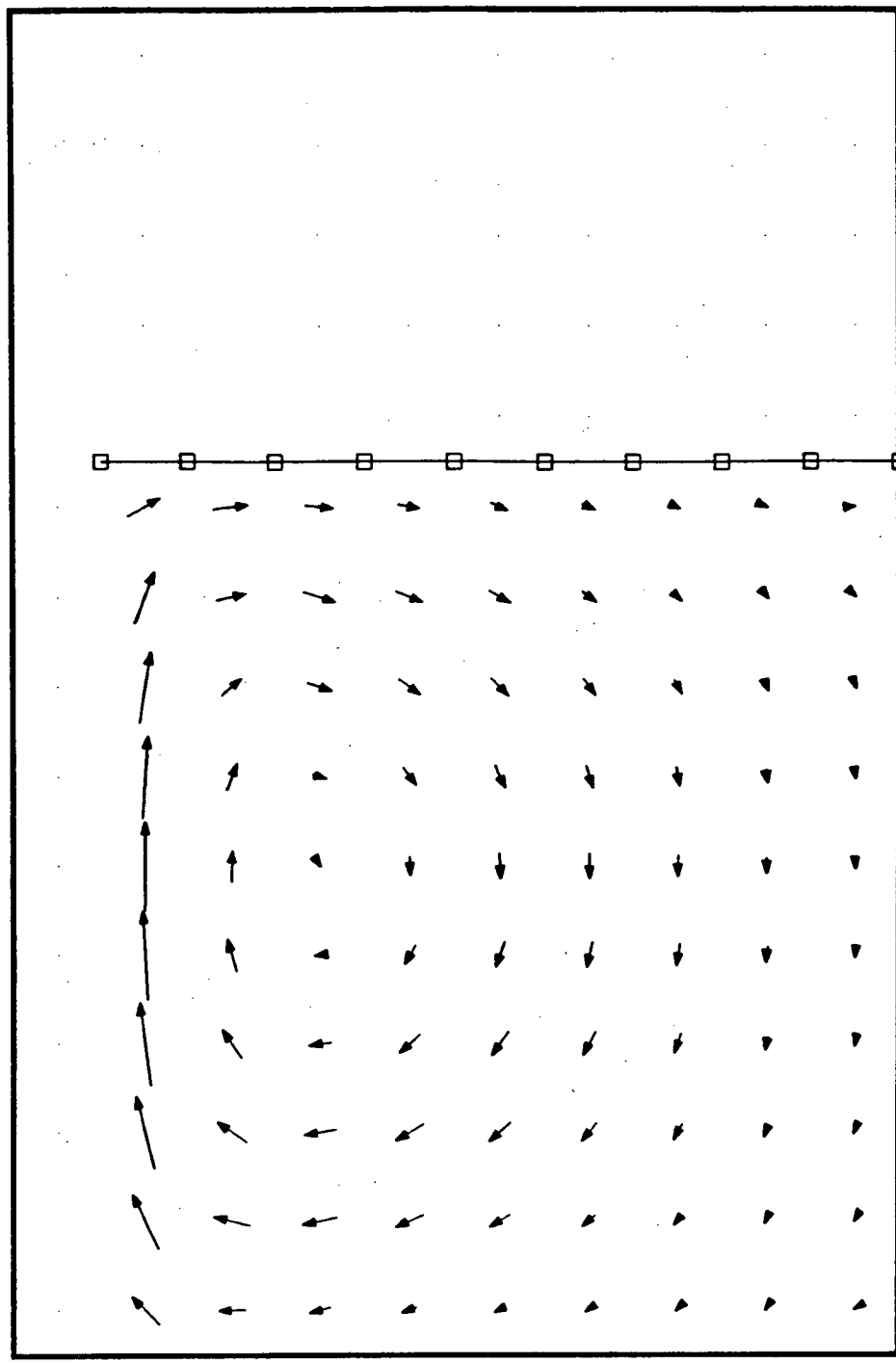

Figure 5.8. Prediction of Experimental Flow Regime Made by Variable Density Condition.

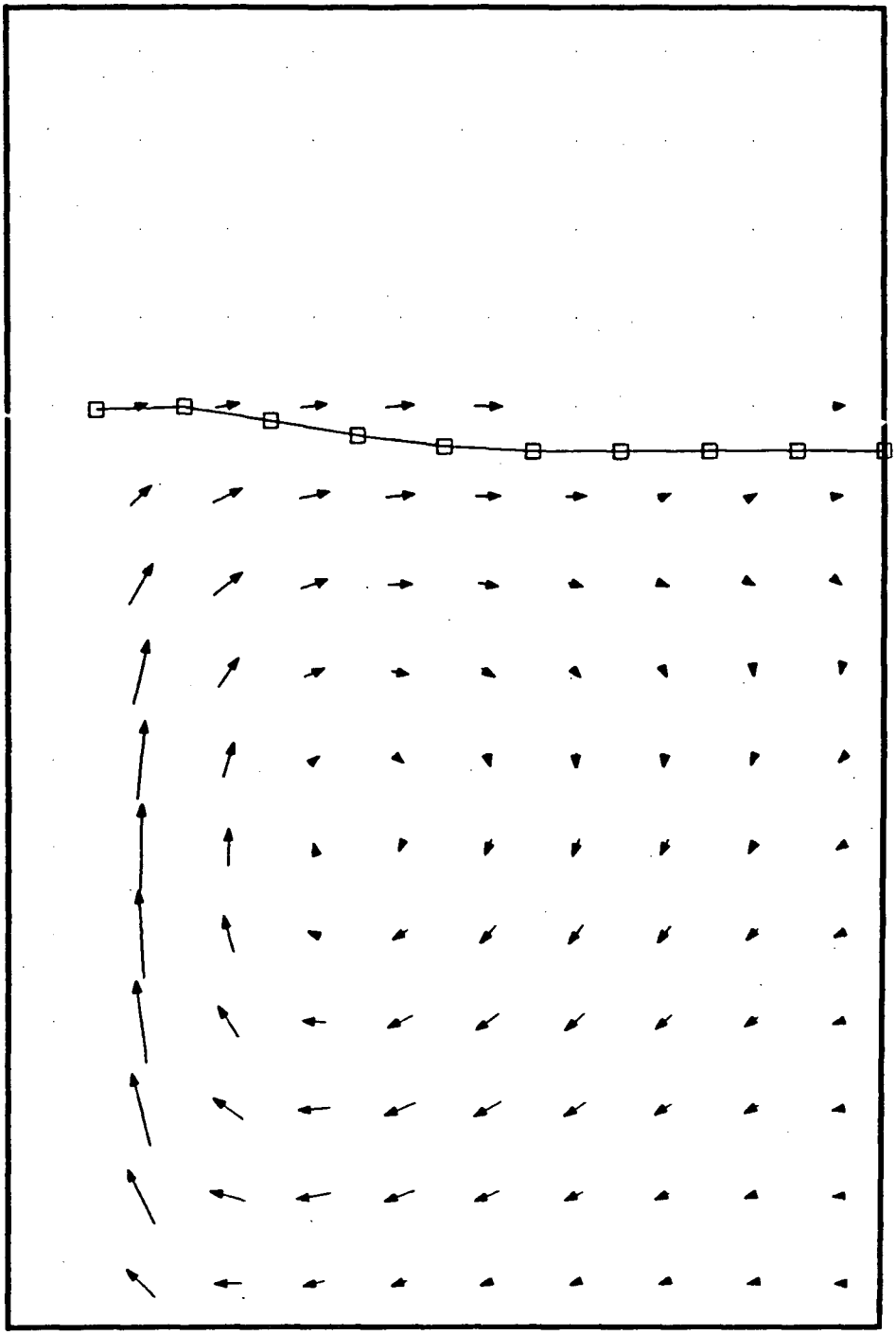

Figure 5.9. Prediction of Experimental Flow Regime Made by Variable Density Condition with Left Wall Velocity.

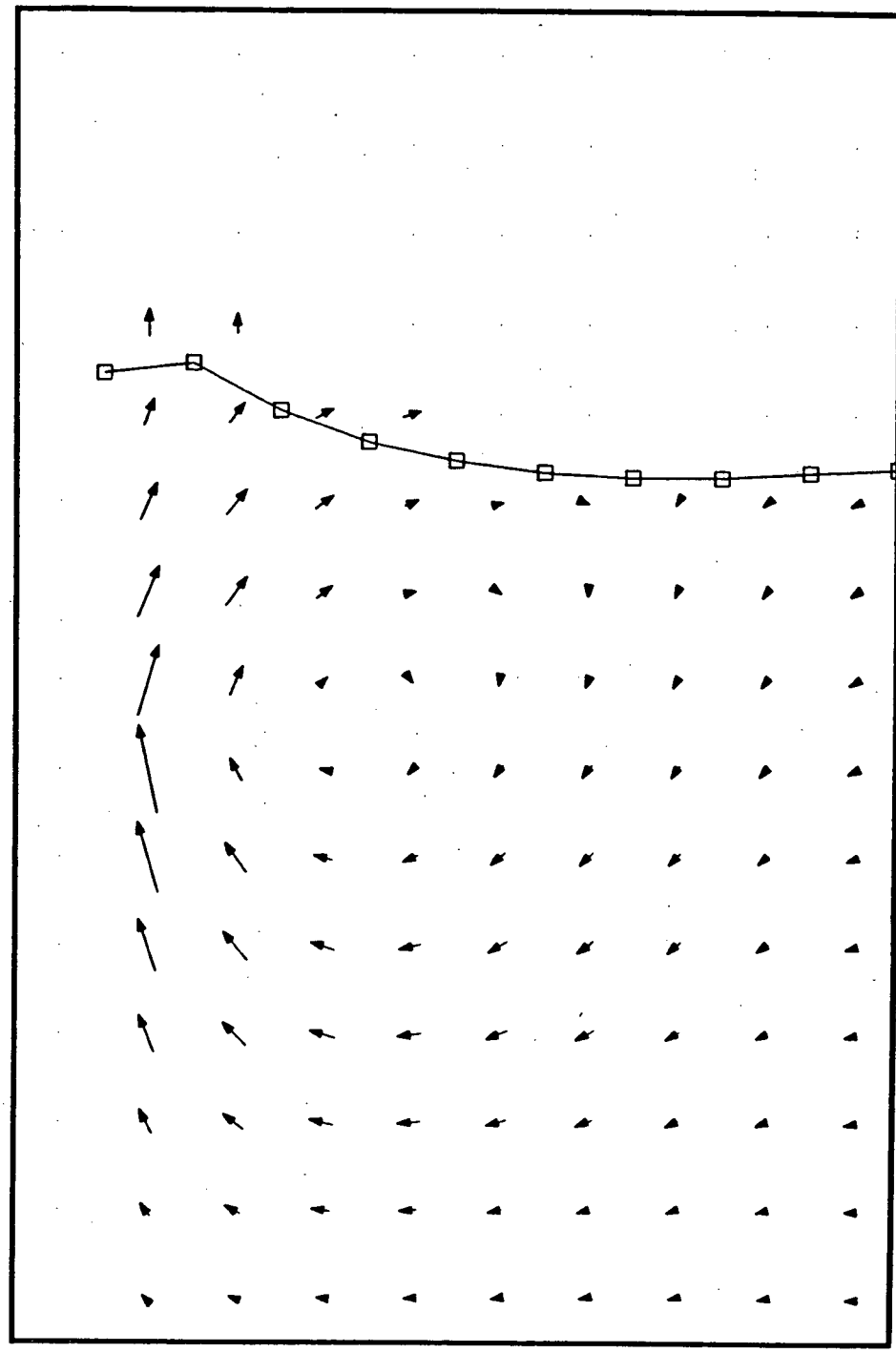

Figure 5.10. Prediction of Experimental Flow Regime Made by Pulsed Boundary Condition.

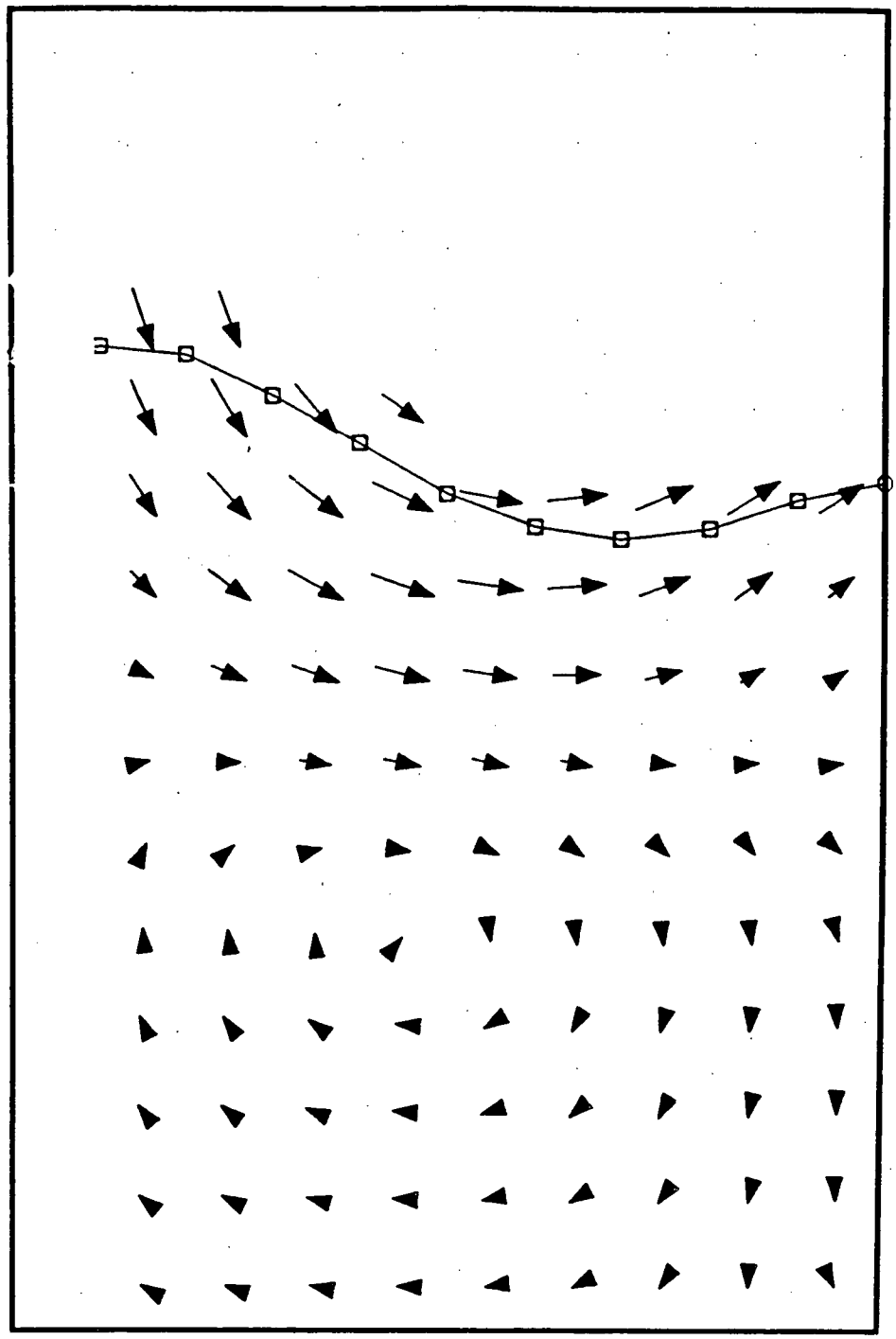

Figure 5.11. Prediction of Experimental Flow Regime Made by Collapsing Surface Condition, T = 0.5 s.

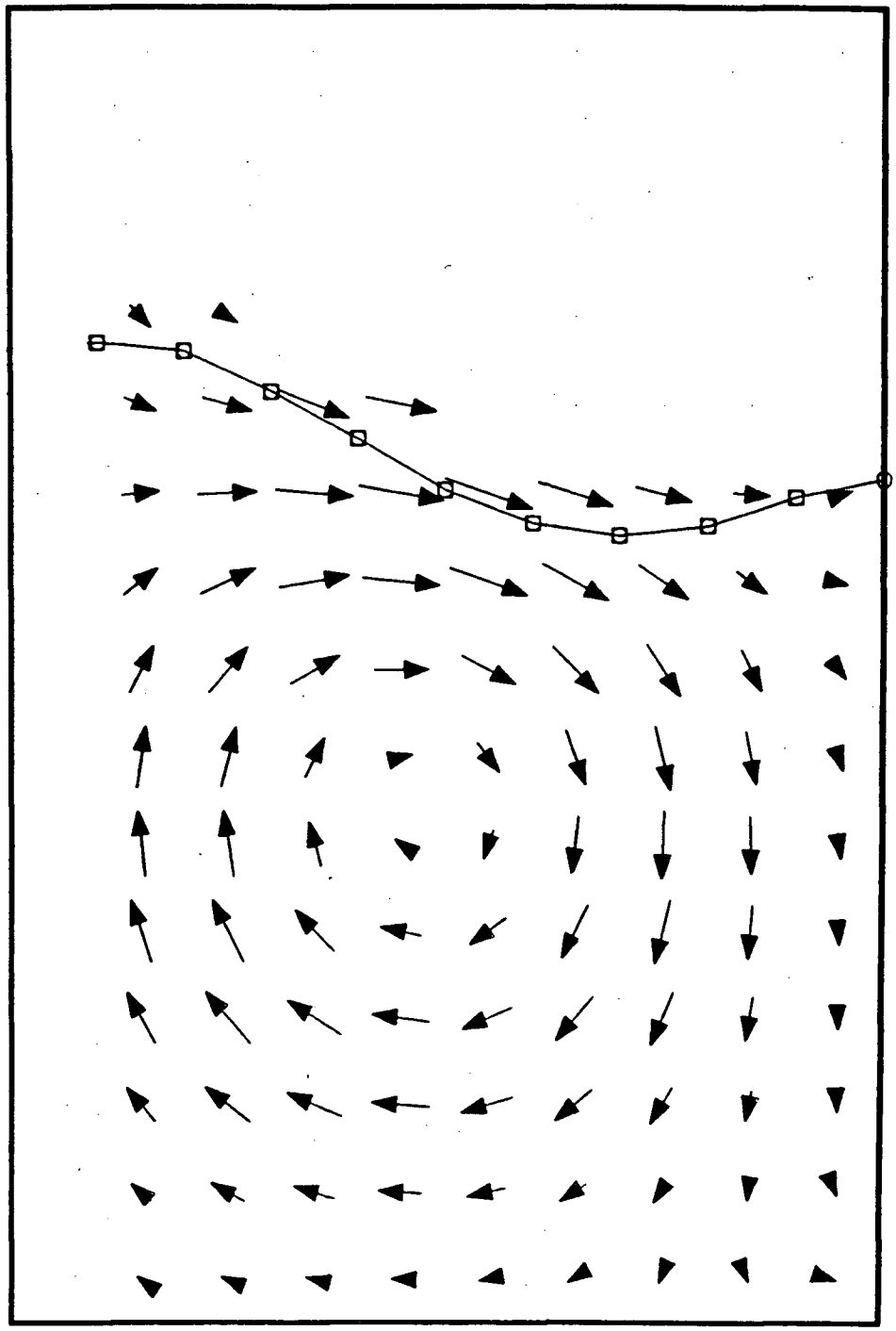

Figure 5.12. Prediction of Experimental Flow Regime Made by Collapsing Surface Condition, T = 0.7 s.

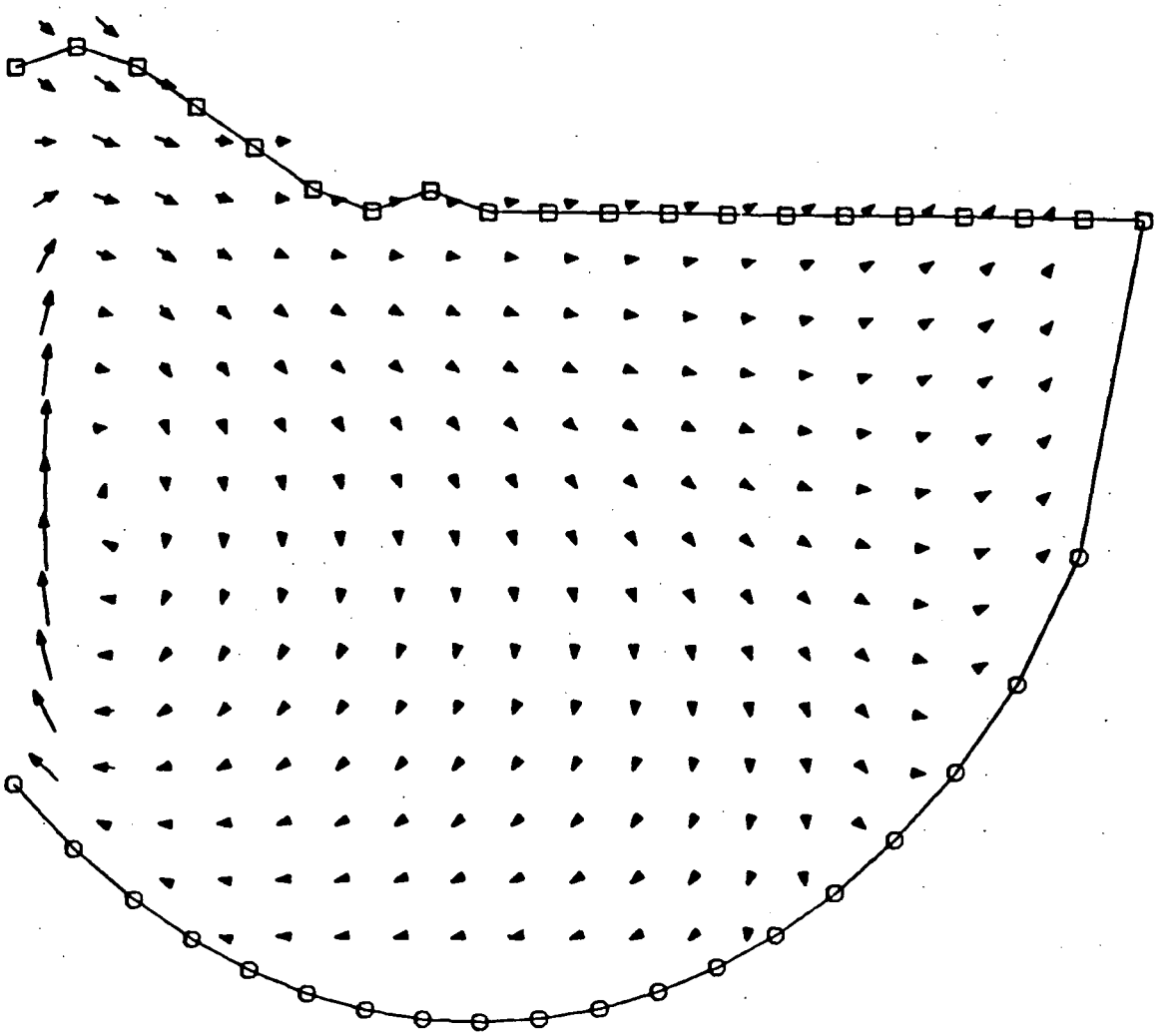

Figure 6.1. Prediction of Flow Regime in a Copper Converter Made by Constant Velocity Boundary Condition.

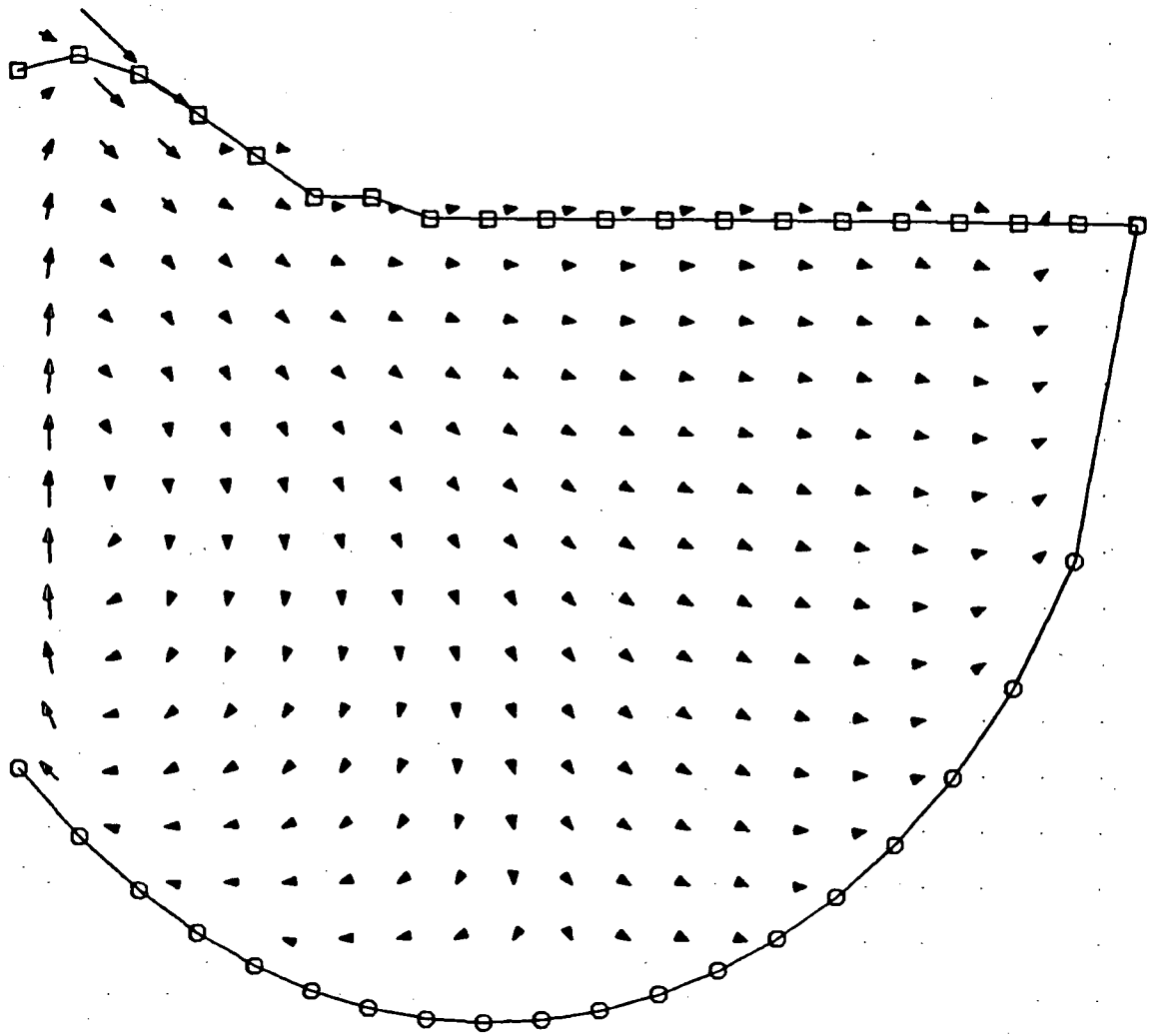

Figure 6.2. Prediction of Flow Regime in a Copper Converter Made by Collapsing Surface Condition.

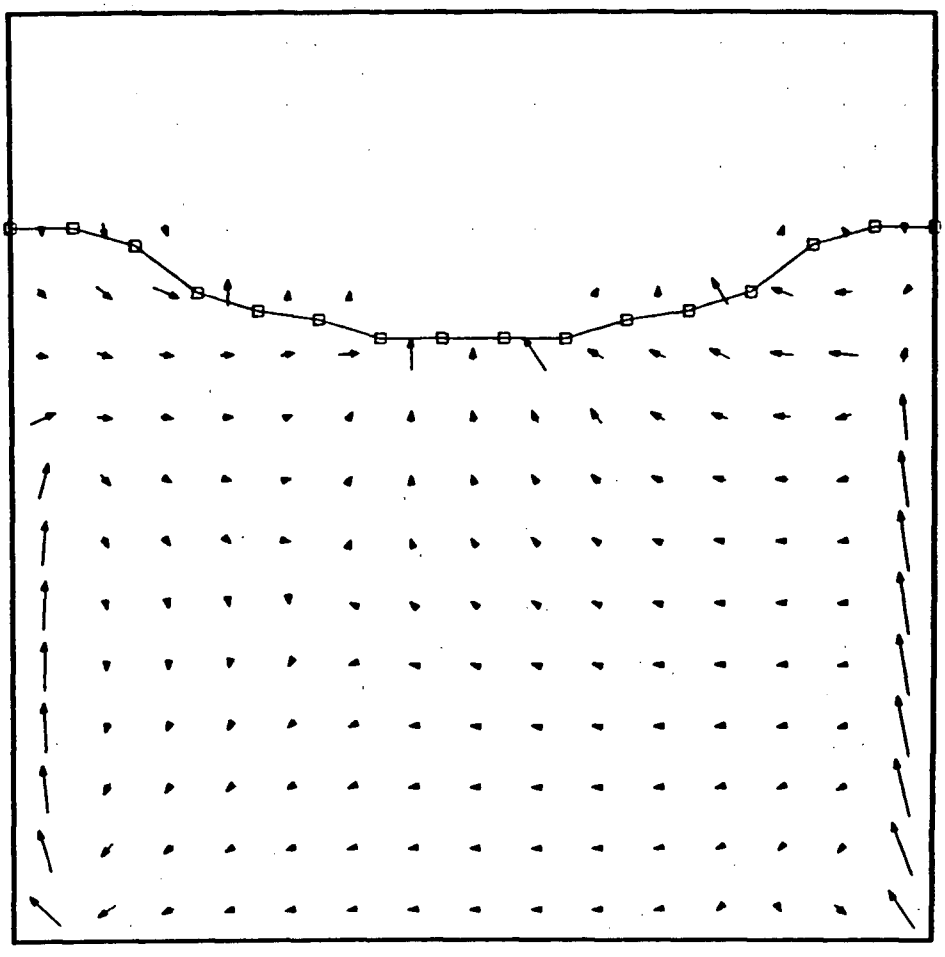

MAXIMUM VELOCITY (M/S) = 0.001

Figure 6.3. Prediction of Flow Regime in a Zinc Slag Fuming Furnace Made by Collapsing Surface Condition.

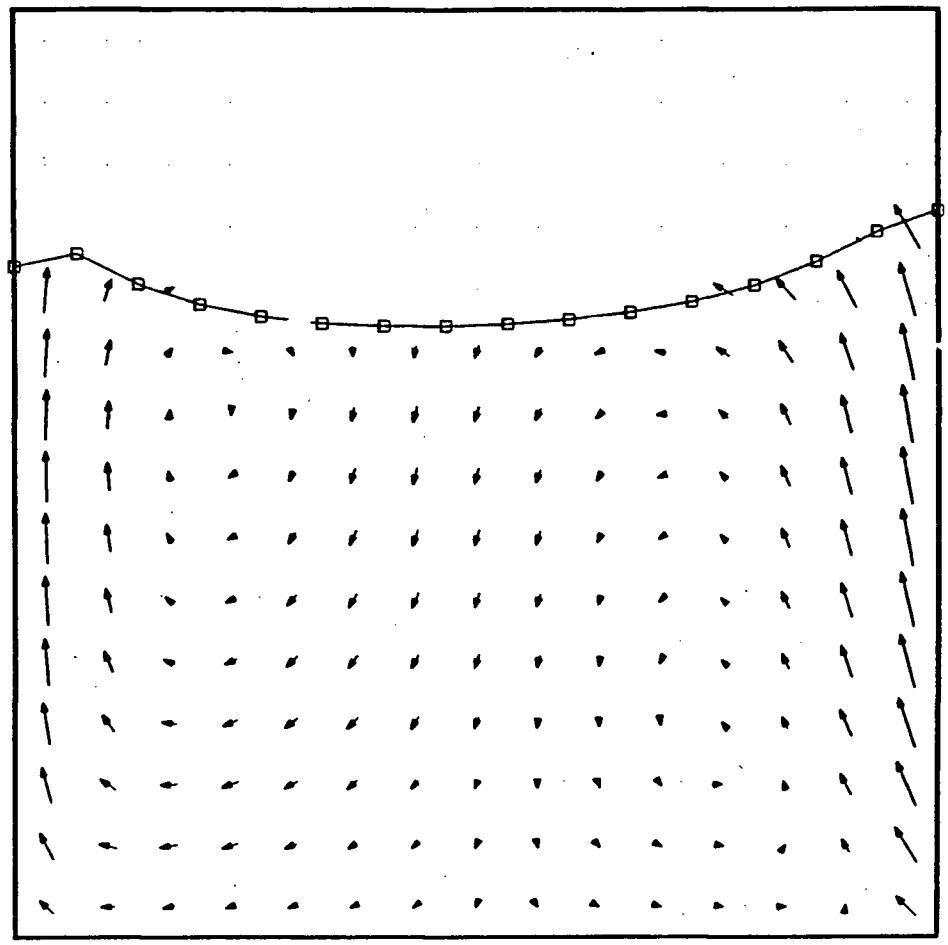

MAXIMUM VELOCITY (M/S) = 0.625

Figure 6.4. Prediction of Flow Regime in a Zinc Slag Fuming Furnace Made by Constant Velocity Condition.

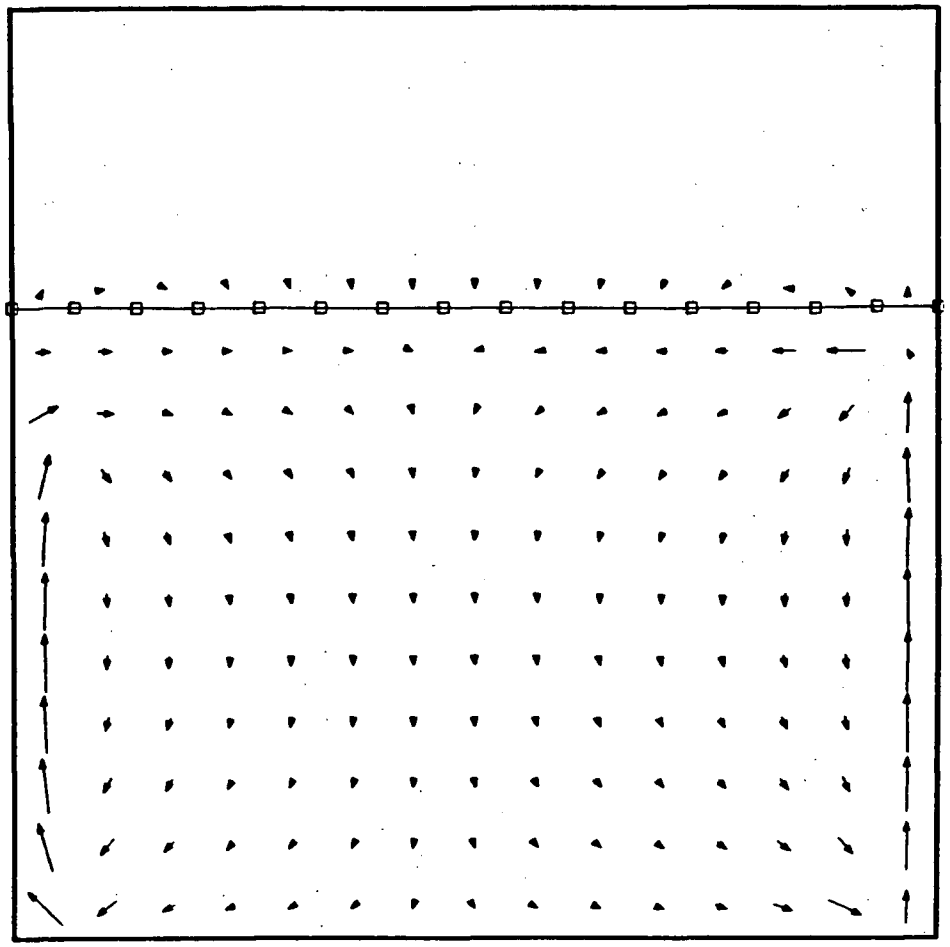

MAXIMUM VELOCITY (M/S) = 0.062

Figure 6.5. Prediction of Flow Regime in a Zinc Slag Fuming Furnace Made by Variable Density Condition.